

THE UNIVERSITY OF TOKYO
Graduate School of Science
Department of Astronomy

Master Thesis

**Multi-emission-line study on H α emitters
at $z \sim 2.3$ from broad-band excesses**

和訳：広帯域フィルタの超過に基づく $z \sim 2.3$ H α 輝線銀
河の多輝線解析

Nuo Chen

Supervisor Prof. Kentaro Motohara

January 2022

Abstract

In this thesis, we present the selection and physical properties of H α emission line galaxies (H α emitters, HAEs) at $2.05 < z < 2.5$, aiming at studying a population of star-forming galaxies at the epoch of Cosmic Noon.

We introduce a new selection method for finding emitters, in which the HAEs are selected from the excess in the observed K_s broad-band flux relative to the best-fit stellar continuum model flux by SED fitting. The photometric data in this thesis is mainly based on the multi-band catalog from the ZFOURGE survey, which contains a very-deep K_s data and five unique and deep medium-bandwidth data (J_1, J_2, J_3, H_s, H_l). Besides, we add two unique medium-bandwidth data K_1 and K_2 , taken by a near-IR camera SWIMS to the ZFOURGE-COSMOS catalog. Then, we applied SED fitting with emission line templates performed by CIGALE. A total number of 1780 HAEs at $z_{med} = 2.25$ are selected with flux excesses of $> 2\sigma$. In virtue of the J and H-band medium-bandwidth data, fluxes of the [OII] or [OIII] emission lines could be simultaneously measured. Finally, 733 HAEs also have the detection of [OIII] with flux excesses of $> 2\sigma$. The line fluxes derived by our method are compared with the newly published MOSDEF Emission-Line Catalogs, and we find a very good agreement with our results that more than 90% H α , [OIII] and [OII] line fluxes have spectroscopic fluxes within a factor of 3. We further run SED fitting simulations by adding random flux errors on model flux from several model emission line templates iteratively. The output line fluxes have differences within 10% comparing to the model flux, indicating a good stability of the SED fitting. Both the observations and simulations prove that the H α , [OIII] and [OII] line fluxes derived by our method are robust and show no significant systematic errors.

We research on the physical properties of these HAEs based on their multiple emission line fluxes and SED-derived parameters. The star formation rate (SFR) versus stellar mass (M_*) relation (i.e., star formation main sequence) shows that our sample has a good correlation with a slope of 0.70 ± 0.03 at $M_* > 10^{9.2} M_\odot$, which is the mass completeness. Meanwhile, we find a large number of low-mass HAEs distributed above the SFMS by $\Delta MS \sim 0.9$ dex, suggesting bursty star formation activities in these systems. Thus, our HAEs are separated into two populations, the main sequence HAEs and the low-mass starburst HAEs. We further explore the oxygen abundance of these HAEs based on the empirical calibration of the O32 index. For the main sequence HAEs, the mass-metallicity relation (MZR) have a power law slope of $O/H \propto M_*^{0.25}$ similar to local galaxies, with an evolving rate of $d\log(O/H)/dz \sim -0.14$ dex. On the other hand, as the O32-metallicity relation is scattered at low-metallicity range, we have reservations about the existence of MZR in low-mass regime. The photoionization models, based on the combination of the O32 and R_{23} indices, are also applied to evaluate the ionization parameters of HAEs. The models reveal that our low-mass starburst HAEs have ionization parameters ~ 0.5 dex lower than those of LAEs at similar redshift. It is also found that our low-mass starburst HAEs have a higher specific star formation rate than LAEs. We speculate that our low-mass starburst HAEs are not an analogous population of LAEs and may have a very low Ly α photon escape fractions.

Contents

1	INTRODUCTION	5
1.1	Cosmic Noon and Star-forming galaxies in this era	5
1.1.1	Star formation rate and its indicators	5
1.1.2	Star formation main sequence at $z \sim 2$	6
1.2	Nebular emission lines and Emission line diagnostics	7
1.2.1	Hydrogen Recombination Lines	7
1.2.2	Forbidden lines	7
1.2.3	Emission line diagnostics	8
1.3	Detection of emission lines	9
1.3.1	Spectroscopy	9
1.3.2	Narrow-band imaging	10
1.3.3	Broad/Medium band imaging and SED fitting with emission line templates	10
1.4	Objectives and Structure of this thesis	11
2	OBSERVATIONS AND DATA	13
2.1	The ZFOURGE survey	13
2.2	SWIMS medium K-band imaging	14
2.2.1	Data Reduction	15
2.2.2	Photometric Calibration and Image depths	16
2.2.3	PSF Matching and Medium-band Fluxes	17
2.3	The MOSDEF survey	17
3	SED FITTING, $H\alpha$ EMITTERS SELECTION AND MULTIPLE EMISSION LINES	19
3.1	Sample Selection	19
3.2	SED fitting with emission line templates	21
3.2.1	Stellar population models and Star formation history	21
3.2.2	Nebular emission lines	22
3.2.3	Dust attenuation model	24
3.2.4	Other parameters	26
3.3	Extracting line fluxes from the best-fit model	27
3.4	$H\alpha$ emitters selection and $H\alpha$ fraction	30
3.5	Reliability of Line Fluxes from SED fitting	32
3.5.1	SED fitting simulation on mock galaxies	32
3.5.2	Flux comparisons with spectroscopic data	36
3.6	The ZFOURGE HAEs catalog	39
4	PHYSICAL PROPERTIES OF $H\alpha$ EMITTERS	41
4.1	$H\alpha$ luminosity function	41
4.2	Star formation rate and Star formation main sequence	44
4.3	Strong emission line ratios	48
4.4	The MZR and FMR at $z \sim 2.3$ with empirical calibration	50
4.5	Photoionization Modeling and ISM ionization states	52

5	DISCUSSION AND IMPLICATIONS	58
5.1	Main Sequence HAEs	58
5.1.1	Star formation rate function	58
5.1.2	Metallicity, MZR and FMR	59
5.2	Low-mass Starburst HAEs	59
5.2.1	Limitation of the O32 calibration	60
5.2.2	Inflow of metal-polluted gas ?	62
5.2.3	Similarity and Difference with LAEs	63
5.3	Futher observations	64
6	SUMMARY AND CONCLUSIONS	66
Appendices		69
A	SWIMS imaging pipeline: SWSRED	69
B	PSF matching on SWIMS reduced image	70
C	Comparison of different SED fitting code	72
D	SED fitting simulation of individual model	75
E	Reddening comparison of various dust attenuation recipes	76

List of Figures

1	Five Fourstar medium-band filters	13
2	SWIMS Medium K-band filters	14
3	Main emission lines drop in Fourstar+SWIMS MB filters	15
4	SWIMS K_2 image in ZFOURGE-COSMOS field	16
5	z_{phot} from ZFOURGE vs. z_{spec} from MOSDEF	18
6	An EAZY sample w/o or with SWIMS K_1/K_2 data	20
7	Improvement of the accuracy of z_{phot} with additional SWIMS data	20
8	Cigale Emission line templates	23
9	Exclude model emission lines from the best-fit model	28
10	The stellar continuum from the best-fit model and observed fluxes	29
11	The $H\alpha$ fraction of the ZFOURGE sample	31
12	The flow chart of the SED fitting simulation on mock galaxies	33
13	The simulation and SED fitting result from one galaxy SED	33
14	Relative changes of the input $H\alpha$ flux ($\Delta F_{H\alpha}$)	35
15	$\Delta F_{H\alpha}$ and its physical dependence	35
16	$\Delta\sigma_{H\alpha}$ and its physical dependence	35
17	Spatial distribution of cross-matched MOSDEF objects	36
18	$H\alpha$ Flux comparison between SED and MOSDEF	38
19	OIII, OII Flux comparison between SED and MOSDEF	38
20	The best-fit $H\alpha$ luminosity function of our sample	42
21	The cosmic star formation rate density (CSFRD) at $z \sim 2.3$	44
22	The star formation main sequence of HAEs at $z \sim 2.3$	45
23	SFR($H\alpha$) vs. SFR(UV) of the HAEs	48
24	Reddening-corrected emission-line ratios vs. M_* for HAEs at $z \sim 2.3$	50
25	The Mass-Metallicity Relation at $z \sim 2.3$ from HAEs	53

26	The Fundamental Metallicity Relation at $z \sim 2.3$ from HAEs	53
27	Relation between OIII/OII and R_{23} -index for HAEs at $z \sim 2.3$	55
28	Average ionization parameter and metallicity for HAEs	55
29	The evolution of Mass-Metallicity Relation	60
30	The “O32 vs. $12 + \log(\text{O}/\text{H})$ ” calibration	62
31	The O32 index have no environment dependence	63
32	The UV-based star formation main sequence of HAEs	64
A.1	The flow chart of SWSRED	69
B.1	The final-median PSF of SWIMS K_1/K_2 image	71
B.2	SWIMS K_2 image before and after convolution	71
C.1	The comparison of the observed $\text{H}\alpha$ luminosity from CIGALE and FAST++	73
C.2	The best-fit SED fitting model from CIGALE, FAST++, FAST, PROSPECTOR	74
D.1	The simulation and output result from a low-mass galaxy SED	75
D.2	The simulation and output result from a high-mass galaxy SED	75
E.1	Observed $\text{H}\alpha$ Flux comparison between SED and MOSDEF	77
E.2	Observed OIII Flux comparison between SED and MOSDEF	77
E.3	Observed OII Flux comparison between SED and MOSDEF	78
E.4	The star formation main sequence of HAEs at $z \sim 2.3$ with the Calzetti curve	78
E.5	The star formation main sequence of HAEs at $z \sim 2.3$ with the SMC curve	79
E.6	Difference between SED-derived and Balmer decrement derived color excesses	81

List of Tables

1	SWIMS Medium-band Observations and Photometry	17
2	CIGALE modules and input parameters used for the SED fitting	26
3	Explanation of the HAEs catalog header	39
4	The best-fit parameters of $\text{H}\alpha$ luminosity functions at $z \sim 2.3$	43
5	The best-fit parameters of SFMS at $z \sim 2.3$	47
6	The summary of galaxy numbers and properties for the subsamples	49
7	Properties and Emission-line Ratios from stacks in each mass bin	51
8	The ionization parameter, $\log(q_{\text{ion}})$, and metallicity, $12 + \log(\text{O}/\text{H})$, distribution	56

1 INTRODUCTION

Galaxy formation and evolution through the cosmic time is one of the biggest topics in astronomy in the past decade. In this chapter, we first review several important facts on star-forming galaxies (SFGs) at $z \sim 2$ revealed by recent observations (§1.1). Then we will go through the astrophysics of interstellar medium (ISM) and the interpretation of their emission-line spectra (§1.2). After that, we will introduce the observational methods for strong emission line galaxies and list advantages and disadvantages of these methods (§1.3). Finally, we present the structure of this thesis and cosmological parameters we use in the last section (§1.4).

1.1 Cosmic Noon and Star-forming galaxies in this era

The early Universe sets the stage for how galaxies evolve to the present stage. Star-forming galaxies at high redshift trace the prime formation epoch of massive disk and elliptical galaxies in the local universe. [Madau & Dickinson \(2014\)](#) concluded an avalanche of observational data and led to a fairly robust outline of the evolution of the star formation activity of galaxies from $z \sim 8$ to $z \sim 0$. The redshift $z \sim 2$, when the universe was roughly 3 billion years old, marks a critical stage of galaxy evolution, during which the overall star-formation activity was at its peak level and more than 50% of the present-day stellar mass formed. As a result, this era is frequently referred to as “Cosmic Noon”. Cosmic Noon is an ideal time to examine mechanisms of star formation. Studying galaxy properties of SFGs in this era offer unique laboratories to understand the galaxy formation and evolution better.

1.1.1 Star formation rate and its indicators

Star formation rates (SFRs) in galaxies are the most important parameters that define galaxies and their evolution across cosmic times. Quantifying SFRs in galaxies requires precise diagnostics methods, in other word, indicators. Mainly there are three kinds of SFR indicators ([Calzetti 2013](#)).

A. Ultraviolet continuum (UV continuum) ($\sim 1300 - 3000\text{\AA}$) probes the direct stellar light emerging from the brightest and youngest stellar populations. After adopting a suitable initial mass function (IMF; e.g., [Salpeter 1955](#); [Chabrier 2003](#)) and flux calibration (e.g., [Kennicutt 1998](#)), UV continuum could be converted to a SFR(UV).

B. On the other hand, especially in dusty system, a significant fraction of luminosity from star is absorbed by interstellar dust and re-emitted in Mid/Far-Infrared wavelengths ($\sim 5 - 1000\mu\text{m}$). As the absorption cross section of the dust is strongly peaked at UV, the bolometric IR luminosity could be another good indicators for star formation activity, symbolized as SFR(IR) ([Kennicutt 1998](#)).

C. In addition to measuring direct or indirect stellar emission, the ionizing photon emitted from massive stars can be traced by the the hydrogen recombination lines (e.g., $H\alpha$), which provide a direct probe of the young massive stellar population as SFR($H\alpha$). Furthermore, some forbidden metal lines (e.g., [OII]) could be used as a quantitative SFR tracer ([Kennicutt 1998](#); [Calzetti et al. 2004](#); [Kennicutt & Evans 2012](#)), calibrated empirically through SFR($H\alpha$).

It should be noticed that these SFR indicators have different timescales. SFR(UV) represents the dominant UV emitting stellar population whose lifetimes are around 100 Myr. SFR(UV) will remain constant over timescales ~ 100 Myr, on behalf of an approximated continuous star formation. In contrast, SFR(H α) is significantly contributed by only stars with masses $> 10M_{\odot}$ whose lifetimes are less than 10 Myr and represents a nearly instantaneous star formation activity.

1.1.2 Star formation main sequence at $z \sim 2$

In the past decade, star-forming galaxies (SFGs) at Cosmic Noon and their SFRs have been detailedly studied. Using SFR indicators, such as UV continuum or H α luminosity, it is found that the vast majority of SFGs hold a correlation between their stellar masses (M_*) and SFR, called the “star formation main sequence” (SFMS) at least up to $z \sim 3$. Moreover, the normalization of SFMS evolves with redshift that higher redshifts objects hold larger star formation rates than local ones with the same stellar mass (Whitaker et al. 2014; Speagle et al. 2014). However, these studies only reach a stellar mass limit of $> 10^9 M_{\odot}$ at $z \sim 2$, due to an observational incompleteness at the low-mass end.

While, with the help of ultra-deep images in the past few years, some recent studies track the lower-mass part of the SFMS at $z \sim 2$. Hayashi et al. (2016), using the NB2315 filter on MORICS, detected ~ 100 H α emitters (HAEs) with stellar masses down to $10^8 M_{\odot}$. Furthermore, Terao (2020) identified ~ 2000 HAEs through the flux excess of K_s -band, by applying SED fitting with the emission line templates to the very deep multi-band dataset of ZFOURGE survey. Although their completeness is limited, both these studies discovered a large population of low mass ($M_* < 10^9 M_{\odot}$) galaxies with specific star formation rate (sSFR = SFR / M_*) higher than at SFMS by an order of magnitude. On the other hand, Ly α emitting galaxies (LAEs) at $z \sim 2$ also lie slightly above the main-sequence line at the low mass end based on their UV measured SFR (Hagen et al. 2016). These offsets mean that these galaxies are undergoing starbursts rather than normal star-forming activity. Also, it may also imply a larger scatter around the SFMS at lower stellar masses than more massive ones, especially for H α -derived SFR, which is seen in cosmological hydrodynamical simulation (Sparre et al. 2017).

However, it is still physically unclear why such kind of low-mass galaxies hold an unexpected high sSFR. Analogous low-mass starburst objects in the local universe, such as blue compact dwarfs (BCDs), usually hold lower metallicities and higher ionization parameters than galaxies with same stellar mass (e.g., Izotov et al. 2006; Janowiecki et al. 2017). The lower metallicity could be explained by recent inflow of pristine (metal-poor) gas in response to the deposition of fresh fuel and the galaxy will experience increasing SFR. The larger ionization parameter means an increasing number of ionizing photons produced, and corresponds to a more intense star formation activity. In addition, when comparing SFR(H α) and SFR(UV), the BCDs shows a larger H α /UV ratio, suggesting a shorter timescale of star formation, i.e, the star formation activity in BCDs is more bursty. Although it is still unclear about the physical condition at high redshift, we can trace such galaxy properties of low-mass population at high redshift through the emission lines produced in their

HII regions, which is introduced in section 1.2.3.

1.2 Nebular emission lines and Emission line diagnostics

Stars form from gas, and the gas is constantly flowing in and out of galaxies between the intergalactic medium (IGM) and the interstellar medium (ISM). Since stars convert lighter elements into heavier elements, we would expect that the gas flowing into a galaxy from IGM is dominated by light elements. On the other hand, the ISM could become a record-keeper of the change in elements of a given galaxy.

ISM consists of the gas in ionic, atomic, and molecular form, as well as dust and cosmic rays (Ferrière 2001). However, observational constraints for high redshift galaxies means that main information of ISM at high redshift comes from HII regions, which consist of high density ionized atomic hydrogen. Orion Nebula is one of the most famous HII region around us and star formation activities of O- and early B-type stars are usually taking place in such HII regions (Osterbrock 1989). The rest-frame UV-optical-near-infrared spectrum of galaxies is characterized by a number of important emission lines from the HII regions in them and these spectral lines are powerful probes of physical and chemical conditions in galaxies. Here, we list some strong emission lines as follow.

1.2.1 Hydrogen Recombination Lines

In HII regions, neutral atoms are ionized by UV photons from hot “exciting” stars and become ions, which is called ionization process. Meanwhile, electrons in the gas clouds will combine with the ions and subsequently emit energy in the form of photons, producing “recombination lines”. Recombination is the opposite of ionization, and these two processes are in equilibrium in HII regions.

Wavelengths of the recombination lines depend on the changes of energy levels. For hydrogen, the primary component of the gas, these ranges from the radio (caused by transitions between the outer energy levels), via the infrared (e.g., Paschen series), to the optical produced by transitions down to 2 (Balmer series). Recombination to the ground level produces a UV photon which itself causes further ionization. Among these observed hydrogen recombination lines, the most prominent one is $H\alpha$ (6563 Å), and some other strong recombination lines are $H\beta$ (4861 Å), $P\alpha$ (1.875 μm), and $P\beta$ (1.282 μm).

1.2.2 Forbidden lines

Forbidden lines from low-lying energy levels of metal ions, such as O^+ , O^{++} , N^+ , are other prominent emissions from HII regions. Forbidden lines violate the quantum-mechanical rules that specify the most probable transitions (electric dipole) by which an atom could return to its ground states. However, these “rule-breaking” transitions could occur via less-probable slower pathways (Sparke & Gallagher 2007). The intensity of a forbidden line depends strongly on the quantity of ions, so it often gives us detailed information on the density and temperature of the HII region, which will be introduced in section 1.2.3.

Famous optical and infrared forbidden lines are [OIII] (5007\AA , $^1D_2 \rightarrow ^3P_2$; 4959\AA , $^1D_2 \rightarrow ^3P_1$), [OII] (3729\AA , $^2D_{5/2} \rightarrow ^4S_{3/2}$; 3726\AA , $^2D_{3/2} \rightarrow ^4S_{3/2}$), and [NII] (6583\AA , $^1D_2 \rightarrow ^3P_2$; 6548\AA , $^1D_2 \rightarrow ^3P_1$).

1.2.3 Emission line diagnostics

For galaxy formation studies, it is essential to understand physical conditions of the ISM in galaxies. The emission lines from the ISM contain a wealth of information on the physical parameter of the target galaxy including the rate of star formation, chemical abundance, and ionization parameter (Kewley et al. 2019).

The gas-phase metallicity is usually expressed as an oxygen abundance relative to hydrogen, and is defined in units of $12+\log(\text{O}/\text{H})$. In a closed-box model of galaxy evolution, metallicity increase over time through each generation of star formation. However, the closed-box model could not reflect the reality in galaxies because pristine gas inflow from IGM and high metallicity gas outflow are happening. Theoretically, as time progresses, the mean metallicity of galaxies increases with age as galaxies undergo chemical enrichment, meanwhile the stellar mass of a galaxy is continuously built in through accretion processes. This leads to observations of a global correlation between the stellar masses (M_*) and gas-phase oxygen abundances [$12+\log(\text{O}/\text{H})$] of star-forming galaxies in the local and high- z universe, known as the mass–metallicity relation (MZR; e.g., Lequeux et al. 1979; Tremonti et al. 2004; Erb et al. 2006). Moreover, further research found that the scatter in MZR could be minimized when extending the relation using the star formation rate (SFR) dimension, resulting in a " M_* -SFR- Z " relation called the "Fundamental Metallicity Relation" (FMR; e.g., Mannucci et al. 2010; Sanders et al. 2018). The Fundamental Metallicity Relation has been interpreted that the accretion of pristine gas from the IGM increases the SFR while diluting the metallicity of the ISM.

The gas-phase oxygen abundances can be determined from a wide variety of emission-lines. The "direct" measurement of the gas-phase oxygen abundance is Auroral lines, mainly by [OIII] λ 4363. However, the Auroral lines are very weak and barely observed. So, empirical calibrations are derived by fitting the observed relationship between Auroral metallicities and strong emission-line ratios. There are several commonly used metallicity-sensitive line emission-ratios to estimate oxygen abundances: $([\text{OIII}]\lambda\lambda 4959, 5007 + [\text{OII}]\lambda\lambda 3726, 29)/\text{H}\beta$ (hereafter R_{23}); $([\text{OIII}]\lambda 5007/\text{H}\beta)/([\text{NII}]\lambda 6584/\text{H}\alpha)$ (hereafter O3N2) and $[\text{NII}]\lambda 6584/\text{H}\alpha$ (hereafter N2).

The amount of ionization photons is another interesting physical property of galaxy. The ionization parameter is defined as $U = n_{\gamma,i}/n_H$ – the ratio of ionizing photon density $n_{\gamma,i}$ to hydrogen density n_H , which works as a tool to measure the abundance of ionization photons produced from massive stars and controls the ionization state in the galaxy (Yeh & Matzner 2012). Starburst environments in the local universe, such as M82, have a maximum of ionization parameter around $\log U \sim 2.3$ (Förster Schreiber et al. 2001; Smith et al. 2006). On the other hand, the ionization parameter of galaxies evolves with redshift, that high- z galaxies usually hold larger $\log U$ than their local counterparts independent of stellar mass (e.g., Kewley et al. 2015; Kaasinen et al. 2017, 2018).

The global ionization parameter in galaxies is usually anti-correlated with the gas-phase metallicity, such that low metallicity galaxies may have large ionization parameters (Dopita & Evans 1986). It is proposed that the stellar wind would have a larger metal opacity at high metallicity, and absorb a larger fraction of the ionizing photons, leaving less to ionize the surrounding HII region. The ionization parameter could be measured directly using the emission-line ratio of $[\text{OIII}]\lambda 5007/[\text{OII}]\lambda\lambda 3726, 29$ (hereafter O32) and $([\text{SII}]\lambda 9069 + [\text{SII}]\lambda 9531)/[\text{SII}]\lambda\lambda 6717, 31$ (hereafter S32).

1.3 Detection of emission lines

Since the emission lines from HII regions contain a wealth of information on galaxy properties, scientists are trying to extract these emission lines from a bulk of observation data. Traditionally, spectroscopy or narrow-band imaging are usually applied for finding emitters. On the other hand, these traditional observations usually consume a large amount of time and suffer from selection bias.

1.3.1 Spectroscopy

Multi-object spectroscopy is the most popular method to get the full spectra of galaxies and obtain emission lines from the stellar continuum. The most important merit of spectroscopy is that very accurate emission line strengths could be obtained through observation. In order to obtain rest-frame optical spectroscopy covering all of the strong emission lines from rest-frame 3700 to 6800Å for $z \sim 2$ galaxies, multi-object medium resolution J, H, K-band spectrographs with very strong resolving powers are utilized, including Keck/MOSFIRE (McLean et al. 2012) and Gemini/Flamingos2 (Eikenberry et al. 2012). These powerful, high-throughput and sensitive instruments provide a large number of valuable spectroscopic data in the past few years.

When carrying out a multi-object spectroscopic observation, a mask (or several masks) with long slits needs to be prepared well in advance. The mask with slits allows for the dispersed spectrum of each source at the detector array, without overlaps with the spectra of other sources. However, because of limited widths of the slits (usually $< 1''$), the long slits will miss lights from outskirts of the galaxies outside the slit apertures. Such slit loss may contribute to 20% if the seeing is close to the slit width.

Besides slit loss, it is hard to construct large samples by the spectroscopy within a limited observation time because spectroscopic observations are really time consuming. For each mask, only ~ 30 objects can be observed simultaneously. Moreover, the exposure time for each filter consumes a few hours especially for high- z galaxies which are fainter than local ones. One of the largest high- z spectroscopic surveys so far, MOSDEF (Kriek et al. 2015), took 24 nights to obtain rest-frame optical spectra of ~ 600 galaxies.

1.3.2 Narrow-band imaging

Photometric observations with narrow-band (hereafter NB) filters, which have $\lambda/\Delta\lambda \sim 100$ (the ratio of central wavelength to bandwidth), also enable us to derive the emission line fluxes. Such NB filters are designed to have bandpasses corresponding to specific emission lines at specific redshifts, so NB imaging are perfect for imaging a cluster of galaxies, among which galaxies have very similar redshifts. For example, [Shimakawa et al. \(2018a,b\)](#) observe two separate proto-clusters at different redshift by two different narrow-band filters on Subaru/MOIRCS ([Suzuki et al. 2008](#)).

With the help of NB filters, galaxies with strong emission lines could be easily identified. The emission line strengths could be achieved through color excesses in NB to the broad-band ($\lambda/\Delta\lambda \sim 5$, hereafter BB) filter which have a similar central wavelength. Usually, emission lines with equivalent width larger than 50\AA in the observed-frame K_s -band have color excess around 0.2 magnitude in NB, so the derived emission line strengths are enough accurate.

However, because of their narrow redshift windows, NB imaging surveys have a very limited searching volume. It is also hard to construct large samples based on NB data within a limiting observation time. For example, [Sobral et al. \(2013\)](#) made a total sample of ~ 800 H α emitters at $z \sim 2.23$ from more than 100 hours exposure-time data in the COSMOS and UKIDSS-UDS fields.

1.3.3 Broad/Medium band imaging and SED fitting with emission line templates

Either spectroscopy (section 1.3.1) or NB imaging (section 1.3.2) has difficulty in constructing large sample of high- z galaxies. In contrast, BB or medium-band (hereafter MB) imaging could be a more efficient choice.

In the past, BB/MB imaging is not a good choice for measuring emission lines. Due to the wider bandwidths of BB/MB filters than NB filters, color excess caused by the emission lines is relatively small, leading to the problem that precise information on the emission lines are almost lost.

However, with new techniques utilizing on SED fitting code, extracting the emission line fluxes from broad-band flux become feasible. Here, estimate of the nebular emission line fluxes based on a stellar population synthesis model are added to the SED templates, called emission line templates. In virtue of these emission line templates, observed fluxes boosted by the emission lines would be taken into account and the stellar continuum lower than the observed fluxes can be estimated. Based on the flux excess between the observed fluxes and the stellar continuum, emission line strengths could be derived by this method. Moreover, the SED fitting with the emission line templates could not only derive the emission line strengths, but also improve the accuracy of some derived important galaxy properties such as stellar masses, dust attenuation and ages. Recent studies (e.g., [Onodera et al. 2020](#); [Terao 2020](#)) have confirmed the feasibility of this method and the derived emission line strengths from the broad-band K_s filter show a good consistency with spectroscopic data or narrow band data.

However, the SED fitting with the emission line templates on broad-band imaging

also has several flaws. Since the broad-band filters have a large bandwidth, several emission lines may drop into the same filter simultaneously. One example is $H\alpha$ (6563Å) and [NII] doublets ($\lambda\lambda 6548, 84$). The wavelengths of the three emission lines are so close that even a low-resolution spectroscopy cannot separate them. This blending will contaminate the measurement of the $H\alpha$ flux. As a result, in the K_s -band, contamination from other emission lines (even [SII] doublets may drop in the filter) must be taken into account as a ratio of $H\alpha$ to total strengths of all emission lines. Such line ratio could be estimated from relative line strengths table in the local universe (e.g., Inoue 2011), but introduces a large uncertainty as properties of galaxies has a large diversity according to their properties such as stellar mass, SFR and metallicity (e.g., Faisst et al. 2018; Reddy et al. 2018; Topping et al. 2021).

To some extent, only with the photometric data from broad-band filter may not be enough to derive accurate information and sometimes extreme emission lines even cause the overestimates of the continuum levels (Terao 2020). Actually, this issue could be handled by adding two or more extra photometric filters during the observations. MB filters, which has spectral resolution of $\lambda/\Delta\lambda \sim 15$, can solve part of this problem. If we add two MB filters, whose wavelength coverages are within the bandwidth of a specific BB filter, one of the fluxes from MB will be boosted by the emission line, while another flux will indicate the level of stellar continuum. As a result, adding extra MB data has an advantage of delivering more information and accurate SED due to the larger number of independent bands. This will not extend observation time too much since the bandwidths of the MB filters are still much wider than those of the NB filters.

1.4 Objectives and Structure of this thesis

The objective of this thesis is to investigate the galaxy properties of star-forming galaxies at Cosmic Noon, especially the low-mass ones which are still physically unclear so far. As mentioned above, the strong emission lines from the HII regions contain a lot of information of the host galaxies. We hope to construct a large number of star-forming galaxies with multiple emission line fluxes and understand their properties statistically.

In this thesis, we present a systematic search of $H\alpha$ emitters (HAEs) at $2.05 < z < 2.5$ based on the photometric catalog from the FourStar galaxy evolution survey (ZFOURGE) and two additional medium K-band photometric data K_1 and K_2 from a near-infrared camera SWIMS (Konishi et al. 2012; Motohara et al. 2014). By applying SED fitting with emission line templates (1.3.3), we construct a large sample of HAEs, which is important to understand physical properties of these galaxies. Moreover, our method can extract not only $H\alpha$ emission line strengths but also [OIII] and [OII] emission line strengths from flux excesses in the J and H medium-band data, included in the ZFOURGE catalog. This will help us to understand much more detailed physical properties such as metallicity and ionization parameter of the HAEs, especially the low mass ones (1.1.2).

The outline of this paper is as follows. We introduce the ZFOURGE survey and the SWIMS medium K-band image, as well as the reduction of SWIMS image in Section 2. Sample selection, the SED fitting with the emission line templates and

the basic measurements of line fluxes including $H\alpha$, $[OIII]$, $[OII]$ are presented in Section 3, and we derive physical parameters of the selected HAEs in Section 4. In Section 5, we compare the low mass HAEs with other analogous objects and discuss their relation with galaxy formation and evolution. Finally we summarize our result in Section 6 and present proposals for future observations to further investigate the properties of HAEs at $z \sim 2.3$.

Throughout this thesis, we adopt the AB magnitude system (Oke & Gunn 1983), assume a Chabrier(2003) initial mass function (IMF) and a Λ CDM cosmology with $H_0 = 70 \text{ km s}^{-1} \text{ Mpc}^{-1}$, $\Omega_m = 0.3$, and $\Omega_\Lambda = 0.7$.

2 OBSERVATIONS AND DATA

2.1 The ZFOURGE survey

Our study is mainly based on the photometric catalog from the FourStar galaxy evolution survey (ZFOURGE, [Straatman et al. 2016](#)). ZFOURGE is a 45-night photometric observation survey with the FourStar near infrared camera ([Persson et al. 2013](#)) on 6.5-meter Magellan telescope. The observation targets at three legacy fields: CDFS ([Giacconi et al. 2002](#)), COSMOS ([Scoville et al. 2007](#)) and UDS ([Lawrence et al. 2007](#)) with a total coverage of ~ 450 arcmin² (128, 135, 189 arcmin² in CDFS, COSMOS, UDS, respectively).

The unique characteristic of ZFOURGE is that it has five near-infrared MB filters: J_1 , J_2 , J_3 , H_s and H_l , covering a similar wavelength range as the BB filters J and H as shown in Figure 1. Moreover, ZFOURGE has a ultra-deep K_s detection map which is a combination of the FourStar K_s images and some other K_s images, such as UltraVISTA ([McCracken et al. 2012](#)) (see Section 2.3 of [Straatman et al. \(2016\)](#), for details). In addition to the above 6 photometric data, ZFOURGE catalog also includes multiwavelength public data covering from $0.3 - 8 \mu\text{m}$. In all, the CDFS, COSMOS, and UDS fields have 40, 37, and 26 photometric data with the 80% completeness of 26.0, 25.5, and 25.8 magnitudes in the combined K_s images, respectively.

Such a large number of photometric data makes it possible to accurately derive the photometric redshift (hereafter z_{phot}) of galaxies. [Nanayakkara et al. \(2016\)](#) measure the spectroscopic redshift (hereafter z_{spec}) of ~ 200 galaxies at $1.5 < z < 2.5$ in ZFOURGE-COSMOS and UDS field, and confirm that the primary z_{phot} for SFGs from ZFOURGE catalog has a very good accuracy that $\Delta z / (1 + z_{\text{spec}}) < 2\%$, where $\Delta z = |z_{\text{spec}} - z_{\text{phot}}|$.

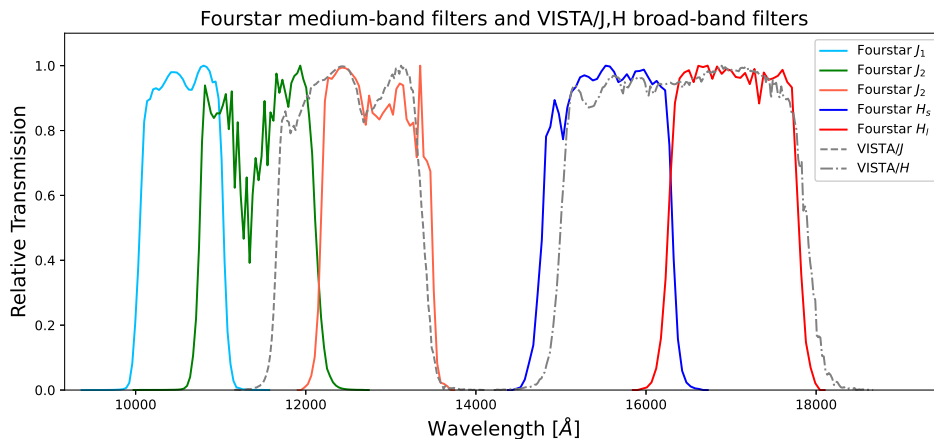


Figure 1. Normalized transmission curves of five Fourstar medium-band filters, J_1 , J_2 , J_3 , H_s , H_l in addition to VISTA/J,H broad-band filters. Atmospheric transmittance is included. The photometric data of the above bands are all included in the ZFOURGE catalog.

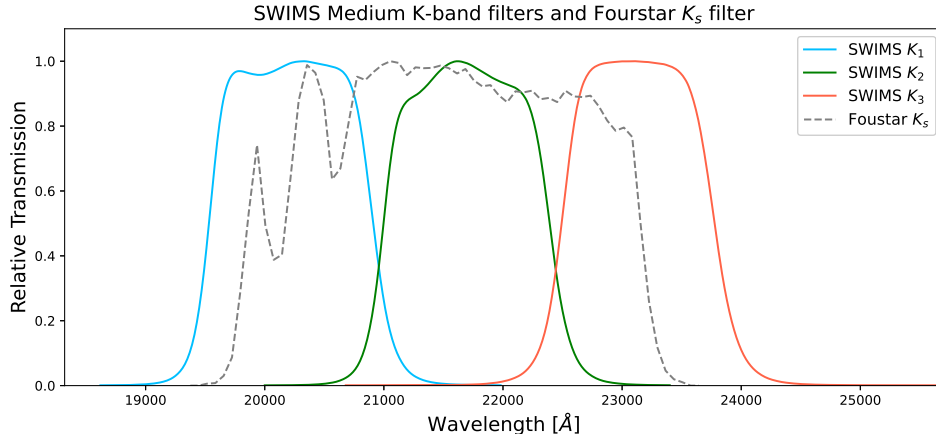


Figure 2. Normalized transmission curves of three SWIMS medium-band filters, K_1 , K_2 , K_3 in addition to Fourstar K_s broad-band filter. The atmospheric transmittance is included only in the K_s filter curve.

2.2 SWIMS medium K-band imaging

FourStar near infrared camera does not have medium-band filters in the K_s -band ($2.0 - 2.4 \mu\text{m}$), where $\text{H}\alpha$ emission line, the most direct SFR indicator, at $z > 2$ falls in.

Luckily, a new NIR camera SWIMS (Simultaneous-color Wide-field Infrared Multi-object Spectrograph, Konishi et al. 2012) is under commissioning at Subaru telescope, which will be installed on the University of Tokyo Atacama Observatory (TAO) 6.5m telescope (Yoshii et al. 2010) in the future. This instrument is capable of simultaneous two-color imaging with a field-of-view (FOV) of 9.6 arcmin in diameter (at TAO) from 0.9 to $2.5 \mu\text{m}$ in a single exposure. One of the unique characteristics of SWIMS is its medium K-band filters (K_1 , K_2 and K_3 -band), which will be a great replenishment for ZFOURGE data. Figure 2 shows the normalized transmission curves of the K_1 , K_2 , K_3 filter and the Fourstar K_s . The SWIMS medium K-band transmission curves are highlighted in RGB colors, while that of the FourStar K_s filter is shown in grey dashed line. As explained in the last paragraph of section §1.3.3, these MB filters could improve the situation because $\text{H}\alpha$ emission lines at $2.0 < z < 2.6$ will separately drop in one of the MB filters, while the other two filters can sample stellar continua. On the other hand, combined with the ZFOURGE medium J and H band data, some other strong emission lines of HAEs at $2.0 < z < 2.6$, including $[\text{OIII}]$, $\text{H}\beta$, $[\text{OII}]$, would fall into the ZFOURGE MB filters (H_s/H_l for $[\text{OIII}], \text{H}\beta$; J_2/J_3 for $[\text{OII}]$) as shown in Figure 3, which provides us with a chance to extract multiple emission lines for these HAEs.

SWIMS currently works as a PI-type instrument at Subaru telescope and has already completed several commissioning observations and open-use observations at S21A and S21B. During the second commissioning observation, a part of (one FOV) the ZFOURGE-COSMOS Field has been observed, and the observation time (seeing) is ~ 2 hours ($1''.0$) and ~ 1.5 hours ($0''.6$) for the K_1 and K_2 filters, respectively.

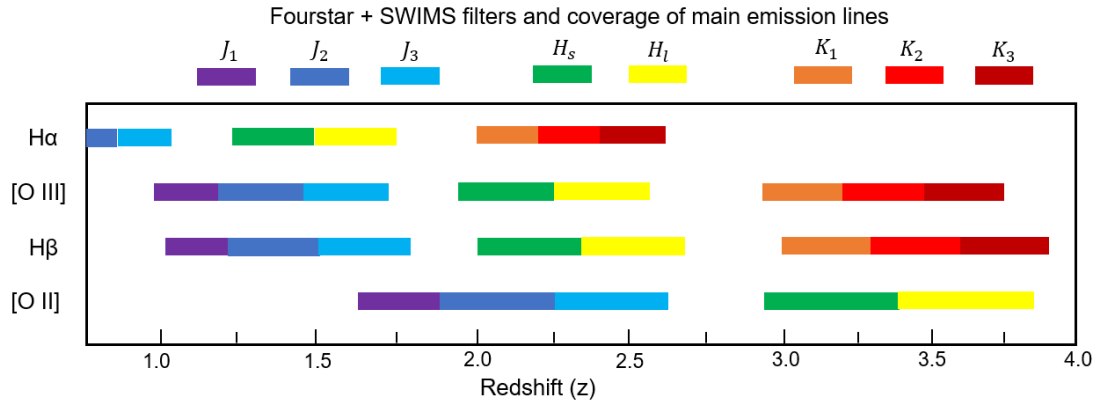


Figure 3. Combinations of several strong emission lines and the MB filters at each redshift. At $z > 1$, H α , H β , [OII] and [OIII] emission lines are observed in the NIR regime. Especially, at $z \sim 2.3$, H α falls into the K medium-band filters. Simultaneously, H β /[OIII] could be observed in the H medium-band filters and [OII] in the J medium-band filters.

2.2.1 Data Reduction

The SWIMS data are reduced by a custom Python-3 pipeline, named “SWSRED” (Konishi et al.), whose stability and performance have already reached at good state. Since SWSRED is written in Python, many options and parameters could be changed easily for different situations and scientific purposes. The detailed description for the pipeline is in Appendix A.

The pipeline processes the data by set, which consists of 18 frames on 9 dithering positions (number of frames and dithering positions depend on the observation) for each of the two SWIMS detectors (when moved to TAO, there will be four detectors). We obtain the bad-pixel map from dark current frames. Dome flat frames are used for flat fielding, which is obtained from dome-on and dome-off frames.

A sky background frame is computed by averaging up to 8 flat-fielded images taken before and after a frame except in the same dithering position. The sky background frames are then subtracted from individual flat-fielded frames to obtain the sky-subtracted frames.

After that, SourceExtractor (SE; Bertin & Arnouts 1996) is applied on the sky-subtracted frames to identify bright sources, then SCAMP (Bertin 2010a) is used on the same frame to obtain astrometric solutions by cross-matching the sources with astrometric reference catalog, Pan-STARRS1 (Chambers et al. 2016).

After registering the astrometry to all the frames in the set, we run SWARP (Bertin 2010b) to stack them together into a single stacked frame. Next, SourceExtractor is applied again on this stacked frame to identify all the objects in the frame, and a master object mask frame and individual object mask frames are created successively.

At last, we iterate the processes from making sky background frames by using the individual object mask frames to stack frames, and repeat the following steps to obtain the final reduced frame. We display the final reduced SWIMS K_2 image and ZFOURGE K_s image in Figure 4.

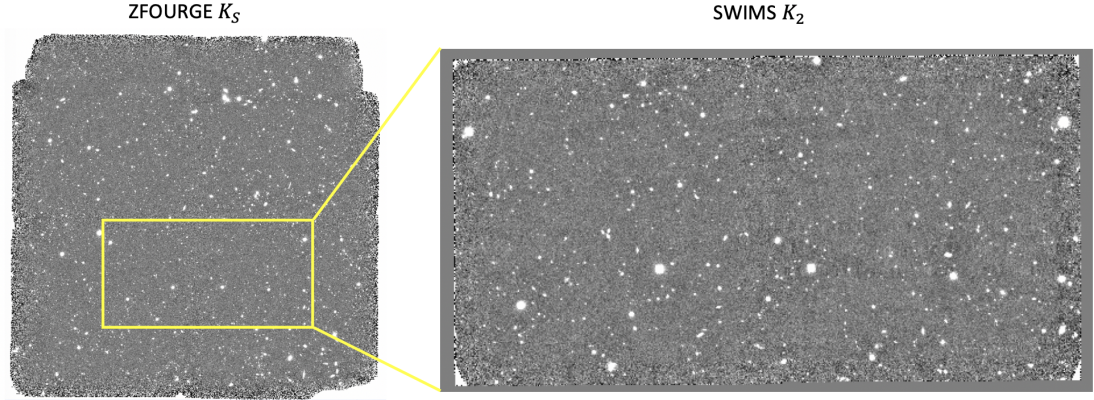


Figure 4. Deep K_s -band detection image in ZFOURGE-COSMOS field from [Straatman et al. \(2016\)](#) and the final-reduced 1.5-hour exposure SWIMS K_2 image in the same field. Because the FOV of SWIMS at Subaru telescope is $6'.6 \times 3'.3$, only 1/6 of ZFOURGE-COSMOS field was covered in the second commissioning observation.

2.2.2 Photometric Calibration and Image depths

SWSRED automatically produces photometric calibration of the final reduced frame by cross-matching to 2MASS catalog ([Skrutskie et al. 2006](#)). However, because the FOV lacks bright stars, 2MASS calibration unfortunately suffer from large uncertainties (up to 0.3 magnitude). As a result, we use photometric data of the ZFOURGE catalog for photometric calibration in this work.

Since K_1 and K_2 filters have unique central wavelengths, we apply a linear interpolation between ZFOURGE H and K_s magnitude in relation to wavelengths and define the magnitude of K_1/K_2 as the interpolated value at the central wavelength of K_1/K_2 , which could be expressed as (using K_1 as an example),

$$m_{K_1} = \frac{m_{K_s} - m_H}{\lambda_{c,K_s} - \lambda_{c,H}} \cdot (\lambda_{c,K_1} - \lambda_{c,K_s}) + m_{K_s}. \quad (1)$$

In order to calculate image depths (limiting magnitudes), we directly measure the fluxes of circular apertures with $0''.6$ diameter (same as ZFOURGE) placed at 5000 random positions on the final reduced images. Due to the dithering pattern, the final reduced images have less exposure at the edges. We therefore put random apertures only on regions larger than 80% of the maximum exposure.

The negative side of the resulting aperture flux distribution, representing the noise distribution, is fit with a Gaussian distribution, from which we derived the standard deviation (σ). σ is then multiplied by 5 and added to the zeropoint, which is derived from the photometric calibration as described above, to obtain an estimate of the 5σ depth. The resulting depth in AB magnitude can thus be summarized as

$$\text{depth}(5\sigma) = m_{zp} - 2.5 \cdot \log_{10}(5 \cdot \sigma_{aper}). \quad (2)$$

A basic summary of the SWIMS medium K-band images in ZFOURGE-COSMOS field is shown in [Table 1](#).

Table 1. SWIMS Medium-band Observations and Photometry

Filter	λ_c (μm)	$\Delta\lambda$ (μm)	Seeing ($''$)	Zeropoint	Total Integration time (min)	5σ depth
K_1	2.023	0.138	0.98	26.13	118	23.7
K_2	2.170	0.140	0.51	26.36	90	23.8

2.2.3 PSF Matching and Medium-band Fluxes

In order to merge our SWIMS sources into ZFOURGE catalog, we follow the PSF matching method of ZFOURGE (see Section 3.1 of [Straatman et al. \(2016\)](#), for details). A detailed procedure of PSF matching on SWIMS images are summarized in Appendix B. In short, we first scale the original images to 25 AB mag and reproject images to match the ZFOURGE pixel sizes. Then, we obtain the average PSF for K_1/K_2 by selecting unsaturated stars with high S/N. After that, we generated a reference PSF having a Moffat profile ([Moffat 1969](#)) with FWHM = $0''.9$ and $\beta = 2.5$. A convolving kernel is derived for each image individually by matching to the Moffat model PSF. Finally, the original images are convolved with this kernel.

Aperture fluxes of K_1/K_2 images are calculated by SourceExtractor in double image mode in virtue of the ZFOURGE ultra-deep K_s detection map. Circular apertures of $1''.2$ diameter, which are sufficiently large to capture most light (PSFs of the convolved images are $\sim 0''.9$), are applied on the detection map, while measurements of aperture fluxes are carried out on MB images. All these aperture fluxes are then corrected to total by multiplying `Ks_ratio` (the aperture correction coefficient) from the ZFOURGE catalog.

Finally, we successfully merge the SWIMS K_1/K_2 photometry into the ZFOURGE-COSMOS catalog. Among the 1541 objects at $2.0 < z < 2.6$ in ZFOURGE-COSMOS field (details of sample selection are in section 3.1), 207 objects ($\sim 13\%$) have both K_1 and K_2 detection and medium K-band fluxes are merged into the catalog. Unfortunately, the total integration times of K_1/K_2 images are not long enough when compared with the ZFOURGE images whose total integration times are ~ 10 hours. The flux errors of $K_1(K_2)$ are $\sim 4(3)$ times larger than that from the ultra-deep K_s detection map. This means that even there are obvious color excesses in our MB images, many objects cannot be classified as HAEs since they have relatively large flux errors (see the selection method in section 3.4). As a result, we still use the K_s detection maps in three fields to select HAEs in our study profited from its ultra-deep imaging and small flux errors.

2.3 The MOSDEF survey

The ZFOURGE catalog we use in our thesis is from the 2017 Data Release. While in the past 4 years, similar fields were also observed by some other surveys. These new data would be a good replenishment and comparison (see section 3.5.2) with our result.

The MOSDEF survey is a 4-year spectroscopic observation utilized the Multi-Object Spectrometer For Infra-Red Exploration (MOSFIRE; [McLean et al. 2012](#))

on the 10m Keck I telescope (Kriek et al. 2015). This survey observed ~ 1500 galaxies at $1.37 < z < 3.80$ in three fields: AEGIS, COSMOS, and GOODS-N, targeted strong nebular emission lines and stellar continuum of these galaxies. The MOSDEF 2D and 1D Spectra and ID+redshift catalog was published on January 2021 and the MOSDEF Emission-Line Catalog was published in May 2021. The detected emission lines from MOSDEF catalog include [OII], [NeIII], H β , [OIII], H α , [NII] and [SII].

Among the catalog, we identified ~ 150 galaxies cross-matched at $z \sim 2.3$ (the middle redshift range of MOSDEF) in ZFOURGE-COSMOS field. We first compare the spectroscopic redshifts from MOSDEF and the photometric redshifts from ZFOURGE, as shown in Figure 5. In the ZFOURGE catalog, spectroscopic redshifts of a part of cross-matched galaxies are already included, where Δz are 0. Most of the other galaxies with only photometric redshifts have $\Delta z / (1 + z) < 0.05$ and only a small percentage are outliers, with $\Delta z / (1 + z) > 0.15$.

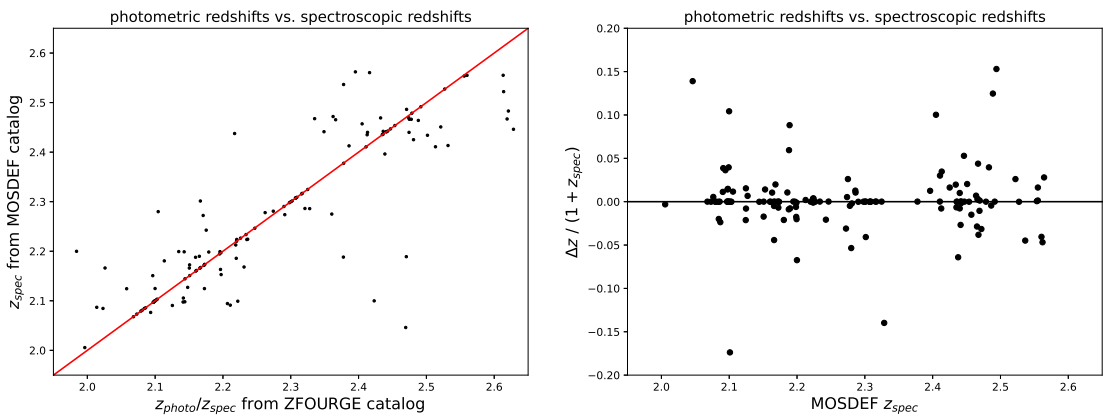


Figure 5. The comparison between the photometric redshift (or spectroscopic redshift) from the ZFOURGE catalog and the spectroscopic redshift from the MOSDEF catalog.

Although deviations on redshifts will not greatly influence the statistic result since MOSDEF cross-matching galaxies take up less than 5% of the parent sample of our study (see section 3.1), we still update z_{spec} in the ZFOURGE-COSMOS catalog with z_{MOSFIRE} from the MOSDEF catalog (though the MOSDEF catalog includes galaxies in UDS field, it did not cover the ZFOURGE-UDS field).

3 SED FITTING, H α EMITTERS SELECTION AND MULTIPLE EMISSION LINES

3.1 Sample Selection

We use the ZFOURGE catalog (Straatman et al. 2016) in three fields (CDFs, COSMOS, UDS) for the sample selection. The goal of our photometric selection is to construct a parent sample of galaxies whose H α emission lines drop in the ZFOURGE K_s filter. Based on the transmission curve of the K_s filter in Figure 2, H α emission lines from galaxies at $2.0 < z < 2.6$ are shifted into the K_s filter. However, the transmission are relatively low at the boundary of the redshift range, we finally define that samples at $2.05 < z < 2.5$ are fully complete (see details in section 3.4). While, when creating our parent sample, we still choose galaxies at $2.0 < z < 2.6$ based on their existing spectroscopic redshifts (z_{spec} in catalog) or photometric redshifts.

The ZFOURGE catalog also contains photometric redshifts, which were derived with a photometric redshift code, Easy and Accurate z_{phot} from Yale (EAZY; Brammer et al. 2008). EAZY fits linear combinations of sets of input galaxy spectral templates to the photometric data, then calculates the photometric redshifts and rest-frame colors. The output parameter z_{peak} from EAZY is chosen as the indicator of the z_{phot} , which is calculated by integrating over the redshift probability distribution function, $p(z)$. One of the unique characteristics of the ZFOURGE survey is that, with the additional medium J/H-band photometric data, the accuracy of photometric redshifts is greatly improved. The high accuracy of photometric redshifts is necessary to minimize scatters and errors in further SED fitting. Based on the scatter in the difference between photometric and spectroscopic redshifts, Straatman et al. (2016) quantified the errors in the photometric redshifts, σ_z , using $1.48 \times$ the median absolute deviation of $|z_{\text{phot}} - z_{\text{spec}}| / (1 + z_{\text{spec}})$. At $z > 1.5$, we have $\sigma_z \approx 0.03$ (see in Figure 7) in the SWIMS-ZFOURGE-COSMOS field (the FOV observed in the commissioning run of Subaru/SWIMS), representing a very good accuracy of z_{phot} at the high redshift.

Moreover, as mentioned in section 2.2, we also merge our SWIMS K_1/K_2 fluxes into the ZFOURGE catalog. For those objects which have additional medium K-band data, we rerun the EAZY code and update z_{phot} (z_{peak}) with the new outputs. The additional SWIMS MB data, to some extent, help us constrain the photometric redshift even better. Figure 6 gives an example before and after the rerun of EAZY. As this object does not show strong color excess in medium J/H band, it shows a bimodal distribution in $p(z)$ when EAZY was run without the SWIMS K_1/K_2 data. However, after SWIMS data being included, we find that the K_1 filter show strong color excess, likely to be boosted by H α emission line, while the K_2 filter may indicate the level of stellar continuum (as mentioned in the last paragraph of section 1.3.3). After the rerun, EAZY no longer gives a bimodal distribution but a very constrained distribution of $p(z)$. Statistically, by comparing the high- z objects which already have z_{spec} in the ZFOURGE catalog, we again obtain the σ_z as ZFOURGE was done. In Figure 7), we find that, after including our SWIMS MB data, σ_z drop from 0.03 to 0.02 in the SWIMS-ZFOURGE-COSMOS field. Statistically, the overall

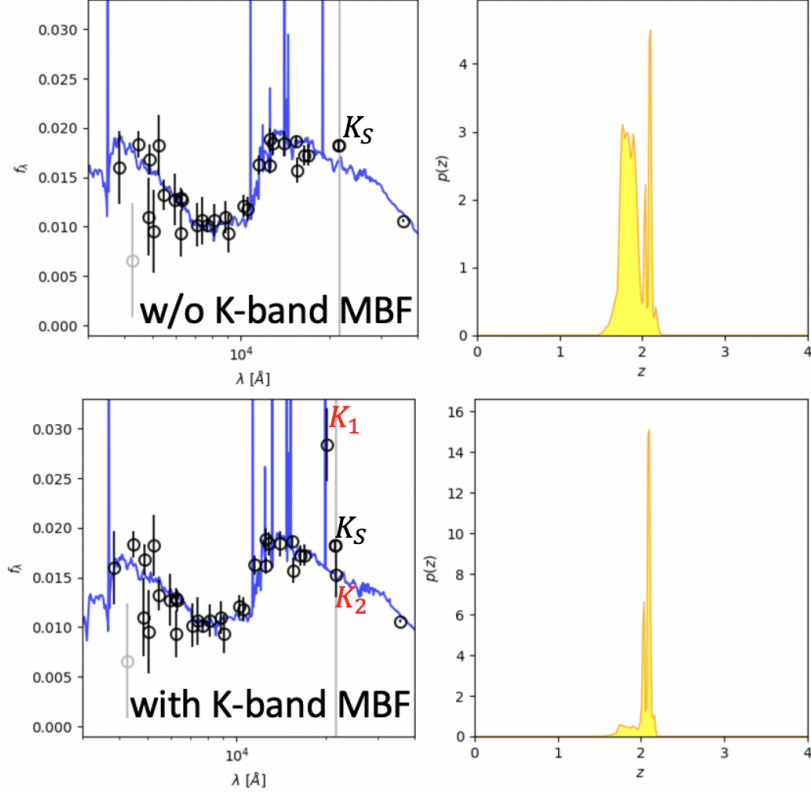


Figure 6. An example galaxy fitted by EAZY templates to obtain z_{phot} . Open circles represent flux of the galaxy in every filter. In the upper panel we show the EAZY result without the SWIMS K_1/K_2 filters. Blue line represents the best-fit template spectrum. In the bottom panel we show the result after including the SWIMS K_1/K_2 bands. In both cases, we exhibit the redshift probability distribution functions $p(z)$ in the right panels. A much better constraint is obtained after including the SWIMS K_1/K_2 data.

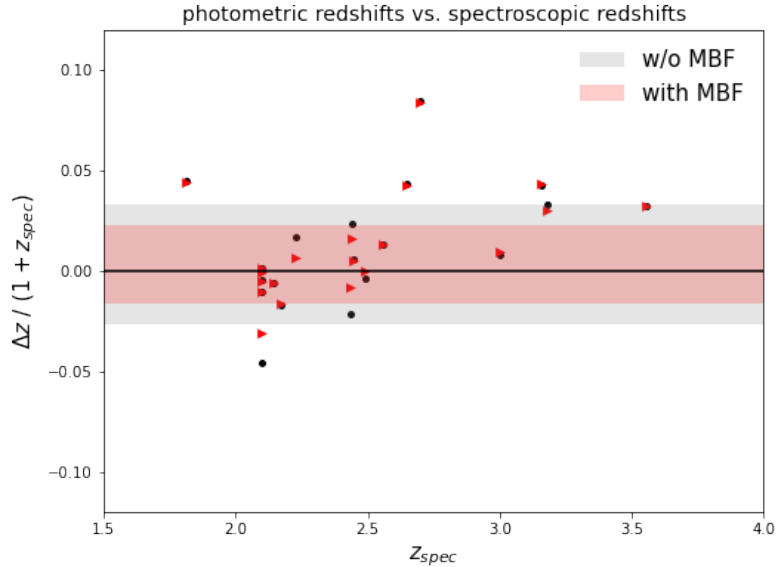


Figure 7. Errors of photometric redshifts in the SWIMS-ZFOURGE-COSMOS field. Black dots represent the results without the SWIMS K_1/K_2 data, while red triangles with the data. Shaded regions indicate the σ_z scatter. $\sigma_z \approx 0.03$ without the SWIMS K_1/K_2 data, while $\sigma_z \approx 0.02$ with the data.

correspondence is ever better after adding SWIMS K_1/K_2 data, as indicated by the smaller scatter in the difference between photometric and spectroscopic redshifts.

After updating the photometric redshifts in the ZFOURGE-COSMOS catalog (for the ZFOURGE/UDS and ZFOURGE/CDFS catalog, we keep the original z_{phot}), we choose galaxies at $2.0 < z < 2.6$ as the parent sample. Spectroscopic redshifts are prior to photometric redshifts in the selection since spectroscopic redshifts derived from redshifted emission-line features are much more reliable than photometric redshifts derived from the best-fit spectral energy distribution. Also, there is a catalog flag `use` in ZFOURGE catalog. This flag eliminates objects such as stars, objects near stars, low S/N objects, and objects with low exposure time, which is very useful to eliminate contaminants. A standard selection of galaxies should be obtained by selecting sources as `use=1`, so we follow this criterion. ZFOURGE catalog also have a list of X-ray-selected, IR-selected, and radio-selected AGN hosts as identified in Cowley et al. (2016). We keep these AGNs in our fitting, but exclude them when deriving statistical galaxy properties. Finally, these cuts (including AGN) produce 4761 galaxies at $2.0 < z < 2.6$ (1676, 1541, and 1544 in CDFS, COSMOS, and UDS respectively).

3.2 SED fitting with emission line templates

After selecting our parent sample, we carry out an SED fitting to obtain primary galaxy properties. The SED fitting is performed by the 2020.0 version of Code for Investigating GALaxy Emission (CIGALE; Burgarella et al. 2005; Noll et al. 2009; Boquien et al. 2019). We have also tried SED fitting with two other codes, FAST++ (Kriek et al. 2009) and PROSPECTOR (Johnson et al. 2021) which are summarized in Appendix C. Here, we exhibit the results from CIGALE.

CIGALE is written in Python. The code creates models based on an energy balance principle in which dust partially absorbs emission in the UV-to-near-IR domain and re-emits self-consistently in the mid- and far-IR. The models are built in a modular way, taking into account flexible parameters of SFH, stellar populations, ionized gas, dust attenuation and more. Such parameters are input and computed on grids, that can reach several hundred million elements in one fitting. The models are then compared with the observations and physical parameters of galaxies such as SFR, stellar mass, and dust luminosity are estimated using a Bayesian statistical analysis approach. Finally, a global indicator of the quality of the fit is given by the reduced χ^2 . In the following subsections, we demonstrate the parameter setting in our fitting.

3.2.1 Stellar population models and Star formation history

CIGALE supports two kinds of simple stellar population models (SSP), one is BC03 (Bruzual & Charlot 2003) and the other is M2005 (Maraston 2005). In this work, we used composite stellar population models generated from BC03 with a Chabrier IMF (Chabrier 2003) as SED templates. Moreover, the metallicity Z of stellar population are allowed to be 0.004, 0.008 and 0.02, in which the first two values are sub-solar metallicity and the last one is close to solar metallicity.

Then, we adopt a delayed- τ models to represent the star formation history (SFH) with the functional form presented in Equation (3). The delayed- τ model depends on the time of the star-formation onset, t_0 , and the e-folding time of the main stellar population model, τ_{main} . This form allows us to have a smooth SFH where the SFR increases from the onset of star-formation until its peak at τ_{main} . After that point, the SFR gradually declines:

$$\text{SFR}_{\text{main}}(t) \propto \frac{t}{\tau_{\text{main}}^2} \times \exp(-t/\tau_{\text{main}}) \quad \text{for } 0 \leq t \leq t_0. \quad (3)$$

The delayed- τ model is considered to be a more representative SFH for SFGs than a constant or an exponentially declining SFH. Cohn et al. (2018) analyze the SFH of several extreme emission-line galaxies (EELGs) at $z > 2.5$ by fitting with non-parametric SFH. These systems show evidence of a starburst in the most recent 50 Myr, with rising SFH in the last 1 Gyr. While our HAEs are also likely to experience starburst recently, it is sensible to choose delayed- τ models as SFH.

When setting grids in our fitting, the stellar population age t_0 ranges in $\log(t_0/\text{yr}) = 7\text{--}10$ with steps of 0.1 dex. The upper limit of t_0 is assumed not to exceed the age of the universe at $z \sim 2$. The e-folding time τ_{main} also ranges in $\log(\tau_{main}/\text{yr}) = 7\text{--}10$ with steps of 0.1 dex. While CIGALE module also allows for an extra exponential burst representing the latest episode of star formation with parameters τ_{burst} and f_{burst} , we do not add this ingredient to our fitting by setting $f_{burst} = 0$.

3.2.2 Nebular emission lines

CIGALE models the galaxy's emission of the ionized gas in HII regions from the nebular templates based on Inoue (2011) via CLOUDY 13.0 (Ferland et al. 1998, 2013). The nebular templates give the relative intensities of 124 lines in HII regions covering from HeII (303.8 Å) to [NII] (205.4 μm), which are parameterized according to a user-defined ionization parameter U (available from -4 to -1), and metallicity (the same as the stellar one) Z, accompanied with a fixed electron density $n_e = 100 \text{ cm}^{-3}$. The ionizing parameter in the local universe have a maximum value around $\log U \sim 2.3$ (see section 1.2.3). Also, Yeh & Matzner (2012) stated that radiation pressure confinement sets the upper limit $\log U \sim -1$ seen in individual regions. Considering that the cosmic star formation is much more intense at high redshift, we set an ionization parameter of $\log U = -2$ during our fitting.

Besides, as mentioned in section 1.2, nebular emission lines are triggered by Lyman continuum (LyC) photons. As a result, some other factors, such as LyC escape fraction (f_{esc} , the leakage of the ionizing radiation into IGM) are also needed to be taken into account when modelling the emission lines. From $z = 11$ to $z = 6$, when the universe was in cosmic reionization era, the IGM becomes ionized and heated by the escaped LyC photons. It is estimated that if the universe is totally reionized by galaxies, a large $f_{esc} \sim 20\%$ at $z > 7$ is needed (Ouchi et al. 2009). In contrast, after the universe is fully reionized, based on direct LyC imagings at lower redshift ($2 < z < 4$, e.g., Vanzella et al. 2010; Grazian et al. 2016; Matthee et al. 2017), an upper limit of the escape fraction is $f_{esc} < 6\%$. Therefore, LyC photons are assumed to be entirely absorbed by neutral hydrogen, i.e., $f_{esc} = 0$. Also, we assume that there is no LyC absorption by dust.

Last but not least, CIGALE could set a user-defined `lines_width` (velocity width) of emission lines, which creates a Gaussian shape on emission lines to take gas motion into account. The default setting of `lines_width` is 200 km/s. However, we find that a large `lines_width` will lead to the blend of emission lines which has close rest-frame wavelengths (e.g., Figure 8). Such blending of emission lines will lead to troubles when we extract the continuum level by removing emission lines in section 3.3. In fact, setting different velocity widths may have some influence on narrow-band filters ($\lambda/\Delta\lambda \sim 100$ corresponds to ~ 3000 km/s), that emission lines may be cut off by the filter occasionally. However, since our fitting are basically using BB/MB filters whose bandpasses are broad enough, the above issue would not cause large uncertainties. After overall consideration, we set FWHM of emission line as 1 km/s, though this assumption is not realistic. We have compared the fitting results with `lines_width` = 200 km/s and 1 km/s, that the effect of setting different velocity widths is negligible when deriving galaxy properties of our galaxies.

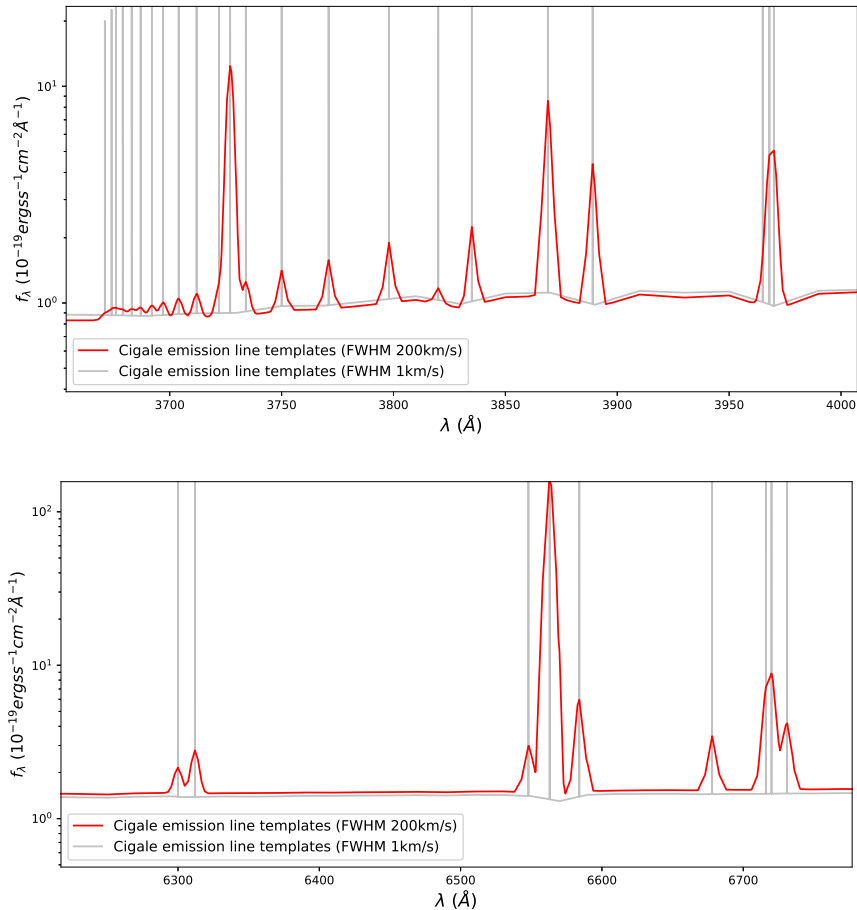


Figure 8. The Cigale Emission line templates with different `lines_width`. The total flux integration of each emission line is same regardless of `lines_width`. The red solid line is the templates with `lines_width`=200 km/s, while the grey solid line is with 1 km/s. Both panels indicate the blend of emission lines when `lines_width`=200 km/s. The upper panel shows many emission lines around the rest-frame 3800 Å, including [OII], [NeIII], HeI and Balmer series from H ϵ to H $_{24}$. The bottom panel shows emission lines around the rest-frame 6500 Å, from left to right are [OI], [SIII], [NII] λ 6548, H α , [NII] λ 6583, HeI, and [SII] λ 6716, 31.

3.2.3 Dust attenuation model

Galaxies contain dust, which absorbs short-wavelength radiation easily and re-radiates in the mid-IR and far-IR. Commonly, we use a dust attenuation curve, $k(\lambda)$, to describe how a galaxy's integrated luminosity is absorbed by the dust at different wavelengths: from far-ultraviolet (FUV), where the attenuation is severe, to NIR, where it becomes almost negligible. Observations in the Milky Way and local nearby galaxies have yielded detailed information on the shape of the dust attenuation curves: the Milky Way curve (Cardelli et al. 1989), the LMC/SMC curve (Gordon et al. 2003), and the Calzetti curve (i.e., the Starburst curve; Calzetti et al. 1994, 2000). At higher redshift, Reddy et al. (2015) have used MOSDEF spectroscopic data to derive the dust attenuation curves at $z \sim 2$, finding it to be very similar in shape to that of the SMC curve at $\lambda > 2500 \text{ \AA}$ and the Calzetti curve at shorter wavelength.

The strength of dust extinction is indicated through the colour excess $E(B - V)$, defined as $E(B - V) = (B - V)_{observed} - (B - V)_{intrinsic}$. For two galaxy with the same dust attenuation curve, the higher $E(B - V)$ means the stronger dust extinction. The colour excess of stellar continuum, $E(B - V)_{star}$ are usually traced by UV spectral slope β . Physically, the colour excess is a measure of the thickness of the dust layer, while the extinction curve provides a measure of the overall cross-section of dust to light as a function of wavelength. Dust extinction and reddening are expressed by the following equations. R_V is defined as the ratio of relative absorption at V-band ($\simeq 0.55 \mu\text{m}$). Dust attenuation curve $k(\lambda)$, as in Equation (5), is commonly fitted with the polynomial with a single parameter λ . The sum of every term except R_V in the polynomial equals to zero when $\lambda \simeq 0.55 \mu\text{m}$. Dust extinction at other wavelength (A_λ , unit: magnitude) can be calculated by extrapolating $k(\lambda)$ to certain wavelength as in Equation 6. Finally, Equation 7 can help to derive the intrinsic flux densities (f_{int}) from observed flux densities (f_{obs}) and dust extinction at certain wavelength.

$$R_V = \frac{A_V}{E(B - V)}, \quad (4)$$

$$k(\lambda) = a_0 + \frac{a_1}{\lambda} + \frac{a_2}{\lambda^2} + \frac{a_3}{\lambda^3} + R_V, \quad (5)$$

$$A_\lambda = k(\lambda) \times E(B - V), \quad (6)$$

$$f_{int}(\lambda) = f_{obs}(\lambda) \times 10^{0.4 \times A_\lambda}. \quad (7)$$

Stellar continuum and nebular emission usually suffer different dust extinction because HII regions may have a different distribution of dust (or dust with different properties) compared to the ambient ISM containing non-ionizing stellar populations (Calzetti et al. 1994; Charlot & Fall 2000). An approach to solve this issue is to assume that each component is subject to a different dust attenuation curve and different $E(B - V)$. Usually, for starburst galaxies, the Milky Way curve (Cardelli et al. 1989) is commonly adopted for the nebular line emission, and the Calzetti curve (Calzetti et al. 2000) for the stellar continuum. In addition, the nebular reddening, $E(B - V)_{neb}$, can be directly measured from the ratio of $H\alpha$ and $H\beta$ emission lines,

i.e, the Balmer decrement, as follows:

$$E(B - V)_{neb} = \frac{2.5}{k'(H\beta) - k'(H\alpha)} \times \log_{10} \left[\frac{(H\alpha/H\beta)_{obs}}{(H\alpha/H\beta)_{int}} \right]. \quad (8)$$

In this equation, $k'(H\alpha)$ and $k'(H\beta)$ are from the assumed nebular attenuation curve; $(H\alpha/H\beta)_{obs}$ is the observed line ratio of H α and H β , while $(H\alpha/H\beta)_{int}$ represents the intrinsic ratio of H α and H β . Assuming a Case-B recombination, $T_e = 10,000K$, and $n_e = 100 \text{ cm}^{-3}$, we usually accept $(H\alpha/H\beta)_{int} = 2.86$ (Osterbrock 1989).

It is found that the color excess of the stellar continuum $E(B - V)_{star}$, and the color excess in the ionized gas $E(B - V)_{neb}$, are different, and usually $E(B - V)_{star}$ is smaller than $E(B - V)_{neb}$. We parametrize the difference of color excesses by a factor f such that:

$$E(B - V)_{neb} = \frac{E(B - V)_{star}}{f}, \quad (f < 1). \quad (9)$$

Various studies have been done on f -factor. Calzetti et al. (1994, 2000) conclude that $f = 0.44 \pm 0.03$ for starburst galaxies in the local universe. Price et al. (2014) indicate that $f = 0.55 \pm 0.16$ for MS star-forming galaxies at $z \sim 1.5$. Kashino et al. (2013) give that $f = 0.83 \pm 0.10$ for sBzK-selected galaxies at $z \sim 1.6$. Reddy et al. (2020) use a sample of > 500 star-forming galaxies from MOSDEF and find that $f = 0.48 \pm 0.02$ at $z \simeq 1.4 - 2.6$. While f -factor still suffers from large uncertainty, it seems to have a trend that f is smaller at a lower redshift and tends to be larger at higher redshift. Saito et al. (2020) introduce a simple redshift evolution in this f -factor, that $f = 0.44 + 0.2z$ by modeling SED and emission lines of $\sim 500,000$ galaxies from the COSMOS2015 photometric catalog (Laigle et al. 2016).

The V2020.0 CIGALE has several choices for modelling dust attenuation curves ($k(\lambda)$) in galaxies. An empirical approach is just to implement the Calzetti curve, named as `dustatt_calzletti`, while a modified powerlaw slope δ could be added to this model (Noll et al. 2009); $\delta < 0$ represents steeper slope than the Calzetti law and leads to smaller R_V . For example, $\delta = -0.45$ gives a $R_V \sim 2.76$ which is similar to the SMC curve and $\delta = 0$ exactly reproduces the basic Calzetti curve. The `dustatt_calzletti` model assumes that stellar continuum and nebular emission share the same extinction curve and $E(B - V)_{star} = E(B - V)_{neb}$. In contrast, in a more complicated model `dustatt_modified_starburst`, Calzetti extinction curve is applied only to the stellar continuum while the emission lines being dimmed with a optional extinction curve selected from the MW, SMC, or LMC curve with a user-defined f -factor from 0 to 1.

In the following, we represent the result from the `dustatt_calzletti` model with $\delta = 0$. The color excess $E(B - V)$ ranges from 0 to 1.0 with steps of 0.02 in the fitting. Although it may not be realistic that the model emission lines follow the Calzetti curve, the derived observed fluxes of emission lines (see the method in section 3.3) shows a good consistency with the spectroscopy data (see details in section 3.5.2). More importantly, this enables us to apply a redshift-dependent f -factor as Saito et al. (2020). We also run the CIGALE `dust_modified_starburst` model with various combination of δ and f -factor. It is found that the stellar

continuum level and observed flux of emission lines do not change much. A detailed discussion of dust attenuation recipe will be presented in Appendix E. Additionally, no UV bump (Stecher 1965) is considered in our dust attenuation model.

3.2.4 Other parameters

We fit the SEDs of our sample using a set of parameters summarized in Table 2 as presented as Boquien et al. (2019).

Table 2. CIGALE modules and input parameters used for the SED fitting

Model	Parameter	Value
sfhdelayed	tau_main (10^6 year)	10, 12.5, 16, 20, 25, 32, 40, 50, 63, 80, 100, 125, 160, 200, 250, 320, 400, 500, 630, 800, 1000, 1250, 1600, 2000, 2500, 3200, 4000, 5000, 6300, 8000, 10000
	age_main (10^6 year)	10, 12.5, 16, 20, 25, 32, 40, 50, 63, 80, 100, 125, 160, 200, 250, 320, 400, 500, 630, 800, 1000, 1250, 1600, 2000, 2500, 3200, 4000, 5000, 6300, 8000, 10000
	tau_burst (10^6 year)	50
	age_burst (10^6 year)	10
	f_burst	0.0
bc03	imf	1 (Chabrier)
	metallicity	0.004, 0.008, 0.02
nebular	log U	-2.0
	f_esc	0.0
	f_dust	0.0
	lines_width ($km s^{-1}$)	1.0
dustatt_calzleti	E_BVs_young	0.0, 0.02, 0.04, 0.06, 0.08, 0.1, 0.12, 0.14, 0.16, 0.18, 0.2, 0.22, 0.24, 0.26, 0.28, 0.3, 0.32, 0.34, 0.36, 0.38, 0.4, 0.42, 0.44, 0.46, 0.48, 0.50, 0.52, 0.54, 0.56, 0.58, 0.6, 0.62, 0.64, 0.66, 0.68, 0.7, 0.72, 0.74, 0.76, 0.78, 0.8, 0.82, 0.84, 0.86, 0.88, 0.9, 0.92, 0.94, 0.96, 0.98, 1.0
	E_BVs_old_factor	1.0
	uv_bump_amplitude	0.0
	powelaw_slope	0.0
	filters	B_B90, V_B90, FUV
	dale2014	alpha
	fracAGN	0.0
redshifting	redshift	

Notes. The grid of models (fluxes and physical properties) is estimated over all the possible combinations of parameters, leading to a total of 8969013 models.

Here, we list some secondary parameter setting in our SED fitting.

The statistical analysis, including the best-fit values and the standard deviations, are computed based on the probability distribution functions (PDFs) implemented as the pdf_analysis module in the fitting.

Dust emission model is implemented as the dust templates of Dale et al. (2014) with $\alpha = 2.0$ and $\text{fracAGN} = 0$. As the longest wavelength in our photometric data is $8\ \mu\text{m}$ (IRAC4), dust emission makes almost no effect in our fitting.

3.3 Extracting line fluxes from the best-fit model

The SED fitting described above allows us to derive not only the stellar continuum levels but also the emission line fluxes of galaxies. However, Terao (2020) found that the line fluxes in the emission line templates strongly depend on model assumptions, while the stellar continuum estimated by the SED fitting are more robust against the model assumptions. This means that the model stellar continuums are more dependable than the model emission lines.

In order to obtain more reliable emission line fluxes from the best-fit model and then to select emitters, we need to define a ‘‘flux excess’’ (F_{excess} , in units of $10^{-19}\ \text{erg s}^{-1}\ \text{cm}^{-2}$) as a difference between the total observed flux and the flux of stellar continuum from SED in a broad/medium-band filter (bandwidth $\Delta\lambda$) as follows:

$$F_{\text{excess}}\ (\text{erg s}^{-1}\ \text{cm}^{-2}) = f_{\text{obs}} \times \Delta\lambda - \int_{\lambda_1}^{\lambda_2} f_{\text{cont}}\ d\lambda. \quad (10)$$

where F_{excess} represents the total flux of all emission lines in a certain filter and theoretically to be zero if no emission line falls into the filter, $\Delta\lambda = \lambda_2 - \lambda_1$ the bandwidth of the filter, f_{obs} the observed flux density of the filter that the target emission line is located, and f_{cont} the stellar continuum obtained from the best-fit SED of each galaxy.

In the CIGALE fitting, each galaxy is provided with a `best_model.fits` file, which represents the best-fit SED. This file includes grids of wavelength and flux densities (F_ν) at each grid. Model emission lines are already included in F_ν in this file, so emission lines should be excluded elaborately from the best-fit model to obtain the stellar continuum, otherwise it would be overestimated. For each emission line in the model, several extra grids with flux densities are added to the stellar continuum independent of the input `lines_width`, i.e, larger `lines_width` only results in broader grids on the wavelength. This characteristic leads to a very convenient algorithm to exclude each emission line. In this algorithm, we first locate the position of the center grid of the emission line at wavelength $(1+z)\lambda$, then we interpolate the flux densities of stellar continuum on the surrounding grids instead of the original flux densities (emission lines + stellar continuum). As mentioned in section 3.2.2, we change the `lines_width` to 1 km/s in the fitting. The reason for this adjustment is that not only emission lines at close wavelengths would be blended up but also the wavelength grids of emission lines and stellar continuum would be blended together. Both issues would make it difficult for subtracting emission lines to estimate correct stellar continuum level. Figure 9 gives an example of extracting the model $\text{H}\alpha$ (and $[\text{NII}]$ doublets) emission line(s). In the left panel, when `lines_width` was set to 1 km/s, $\text{H}\alpha$ emission lines is added to the continuum with an extra 9 grids ($\text{H}\alpha$ and $[\text{NII}]$ are separated). The continuum level can be precisely defined because the grids with the emission line cover a very narrow wavelength range. We interpolate the flux densities of these grids with those of the stellar continuum and obtain the red solid line which

clearly indicates the model stellar continuum. In contrast, when `lines_width` was set to 200 km/s as in the right panel, H α , [NII] doublets and stellar continuum are blended together in wide wavelength range. When we apply our algorithm to remove emission lines on this model, a residual is left as red solid line which will lead to an overestimate of stellar continuum and an underestimate of flux excess simultaneously. Therefore, we adopt the parameter setting of `lines_width` = 1 km/s in our fitting because we can obtain a correct stellar continuum as shown in Figure 10.

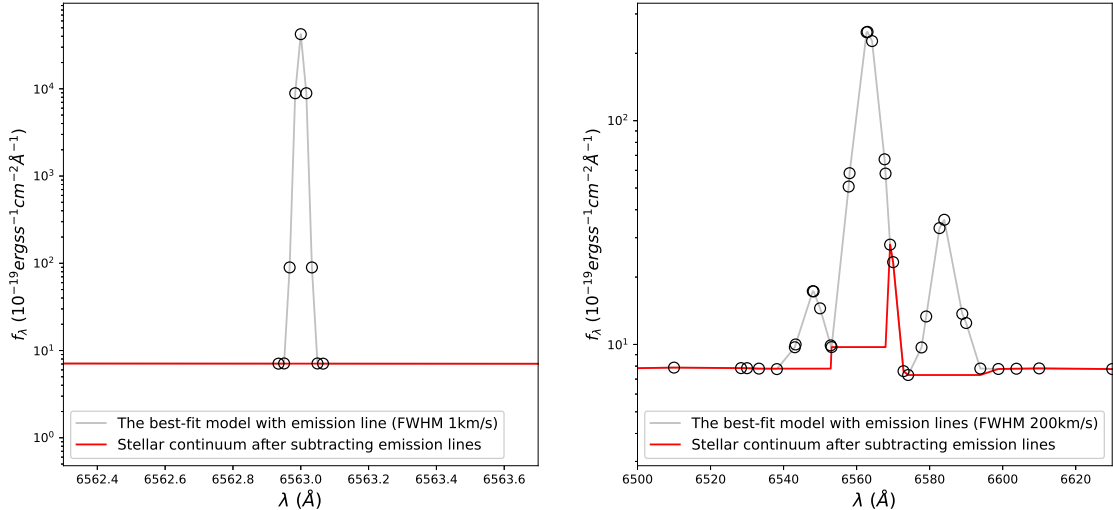


Figure 9. Example of a case of excluding emission line(s) from the best-fit model. In both panels, grey solid line indicates the best-fit model. Grids of wavelengths and corresponding flux densities are shown with open circles. Red solid line is the derived stellar continuum level by our algorithm. Left: The best-fit model with `lines_width` = 1 km/s. Right: The best-fit model with `lines_width` = 200 km/s.

In this thesis, we have extracted the H α emission line from the flux excess in the K_s filter, the [OIII] emission line from the flux excess in the H_s or H_l filter and the [OII] emission line from the flux excess in the J_2 or J_3 filter of galaxies at $z \sim 2.3$ (see also in Figure 3).

However, as mentioned in section 1.3.3, several emission lines may drop into the same broad/medium-band filter simultaneously because of the large bandwidth. Isolating close emission lines is not realizable with only the BB/MB data, so we need to put either of the following assumptions to separate them. One assumption is to define a ratio of the target emission line to the total strengths of all the emission lines in the same filter (r_{EL}), defined as:

$$F_{EL} (erg s^{-1} cm^{-2}) = r_{EL} \times F_{excess}. \quad (11)$$

Here, F_{EL} is the derived observed emission line fluxes and F_{excess} is the flux excesses from Equation (10).

In the K_s filter, the main contaminants are [NII] $\lambda\lambda 6548, 84$ and [SI] $\lambda\lambda 6717, 31$. The common solution is to assume a constant contamination fraction based on

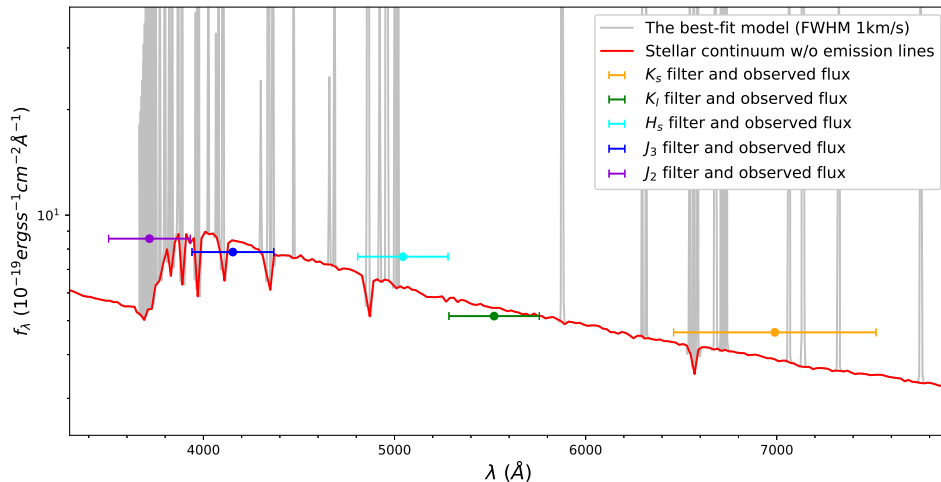


Figure 10. The best-fit model of a galaxy at $z \simeq 2.1$ with `lines_width = 1 km/s`. Grey solid line indicates the result from the best-fit model (before subtracting emission lines), while red solid line shows the stellar continuum after excluding emission lines. We also display the observed fluxes and bandwidth of the J_2 , J_3 , H_s , H_l , and K_s filter. $H\alpha$ line causes a boost in the observed flux of the K_s filter, $[\text{OIII}]$ line in the H_s filter and $[\text{OII}]$ in the J_2 filter. On the other hand, the fluxes of the J_3 and H_l filters are close to the stellar continuum.

average values in the local universe, but it is likely insufficient for describing galaxies at high redshift (Topping et al. 2021). Therefore, we refer to the MOSDEF Emission-Line Catalog (Kriek et al. 2015) to estimate a typical emission-line ratios at $2.0 < z < 2.6$. First, we remove galaxies with non-detection of $[\text{NII}]$, $[\text{SII}]$ and $[\text{Nii}]\lambda 6584 / H\alpha > 0.5$. The last criterion is introduced because such strong $[\text{NII}]$ emission is not likely to be emitted by star formation and to exclude possible AGN hosts (BPT diagram; Kauffmann et al. 2003). This selection yields a sample of 453 objects. From this sample, we obtain the line ratios, $H\alpha / (H\alpha + [\text{NII}] + [\text{SII}])$ and take their average to obtain 0.67 ± 0.10 . Finally, we keep one significant digits and define $r_{H\alpha} = 0.7$.

In J_2/J_3 filter, $[\text{NeIII}]\lambda\lambda 3870, 3969$ and Balmer lines such as $H\epsilon \lambda 3970$ contaminate $[\text{OII}]$. We estimate r_{OII} in the same manner. Although the MOSDEF catalog contains only $[\text{OII}]$ and $[\text{NeIII}]$ and no weaker Balmer lines shorter than $H\delta \lambda 4103$, we assume $[\text{NeIII}]$ as the main contaminant and remove galaxies with non-detection of $[\text{NII}]$, $[\text{OII}]$, $[\text{NeIII}]$ and $[\text{Nii}]\lambda 6584 / H\alpha > 0.5$. This criterion leads to a sample of 270 objects and the average line ratio, $[\text{OII}] / ([\text{OII}] + [\text{NeIII}])$, from this sample is 0.71 ± 0.14 . Likewise, we define $r_{\text{OII}} = 0.7$.

After comparing with the spectroscopic observed flux from the MOSDEF catalog (in section 3.5.2), we find the ratios of $r_{H\alpha} = 0.7$ and $r_{\text{OII}} = 0.7$ leads to no bias in the derived emission line fluxes by our method.

For $[\text{OIII}]$ emission lines in the H_s/H_l filter, we assume that the total flux excesses are only contaminated by $H\beta$. Because the ZFOURGE K_s -band data are very deep and the flux errors are relatively small, the derived $H\alpha$ fluxes are relatively credible. So, we assume a Case-B recombination with $T_e = 10,000\text{K}$ and $n_e = 100\text{cm}^{-3}$, and

derive the intrinsic H β fluxes from the intrinsic H α fluxes as,

$$F_{\text{H}\beta, \text{int}} = \frac{F_{\text{H}\alpha, \text{int}}}{2.86}. \quad (12)$$

Here, $F_{\text{H}\alpha, \text{int}}$ are corrected for dust extinction by $A_{\text{H}\alpha}$ (see section 3.6 for the derivation of $A_{\text{H}\alpha}$). After deriving $F_{\text{H}\beta, \text{int}}$ by Equation (12), we apply the dust extinction of H β ($A_{\text{H}\beta}$) through the same attenuation curve as $A_{\text{H}\alpha}$ and obtain the observed H β fluxes, $F_{\text{H}\beta, \text{obs}}$. Finally $F_{\text{H}\beta, \text{obs}}$ is subtracted from the total flux excesses to get the [OIII] emission line fluxes.

In conclusion, if flux excesses in the three filters are available, we can obtain the observed emission line fluxes of H α , [OIII], and [OII] as follows,

$$F_{\text{H}\alpha, \text{obs}} = (1 - 0.3) \times F_{\text{excess}, K_s},$$

$$F_{[\text{OIII}], \text{obs}} = F_{\text{excess}, H_s/H_l} - F_{\text{H}\beta} = F_{\text{excess}, H_s/H_l} - \frac{F_{\text{H}\alpha, \text{obs}} \cdot 10^{A_{\text{H}\alpha}}}{2.86 \cdot 10^{A_{\text{H}\beta}}}, \quad (13)$$

$$F_{[\text{OII}], \text{obs}} = (1 - 0.3) \times F_{\text{excess}, J_2/J_3}.$$

Thanks to the deep data from the ZFOURGE catalog, it is possible to carry on multi-emission-line analysis on galaxies.

3.4 H α emitters selection and H α fraction

We select candidates of H α emitters by requiring the flux excesses in the K_s -band to be twice larger than its photometric errors ($> 2\sigma$), that is,

$$F_{\text{excess}, K_s} > 2 \times \Delta f_{K_s} \times \Delta \lambda. \quad (14)$$

Also, in section 3.1, we select our parent sample from a redshift range of $2.0 < z < 2.6$. But at the boundary of this redshift range, we may not acquire a completed sample of H α emitters because of the uncertainties in the photometric redshift and the real shape of the filter. Figure 11 indicates the H α fraction (the number of HAEs to the number of all galaxies) of ZFOURGE field from $z = 2.0$ to $z = 2.6$ with steps of 0.025. The peak of the H α fraction in each redshift bin in our survey are ~ 0.5 . In order to obtain a clear sample of emitters and exclude contamination outside the filter, we cut off the redshift bin whose H α fraction are lower than half of the peak value (0.25). Finally, we adopt the redshift range at $2.05 < z < 2.5$ for further scientific discussion.

These two selection criteria yield a sample of 1815 H α emitters (649, 574, 592 in CDFS, COSMOS, UDS respectively) at $z_{\text{med}} = 2.25$.

Furthermore, we derive the [OII] and [OIII] emission line fluxes of these HAEs from the flux excesses in the medium J/H-band. We follow the flux excess criterion of 2σ when extracting line fluxes of these two lines. A detailed information of HAEs with [OII] and [OIII] emission lines will be listed in section 3.6.

The bottom three panels of Figure 11 indicate the H α fraction of ZFOURGE-CDFS, COSMOS, and UDS field. In the COSMOS field, we find that the total

number of HAEs at $z \simeq 2.1$ is much larger than other redshift bin, which confirm the existence of the COSMOS cluster at $z = 2.095$, first discovered by Spitler et al. (2012). This suggests that we can compare a large number of HAEs in clustered or field environments from our sample and may be able to answer an open question whether the star formation activities in dense environments are enhanced or suppressed relative to the field at high redshift (e.g., Elbaz et al. 2007; Koyama et al. 2013; Zeimann et al. 2013; Tran et al. 2017).

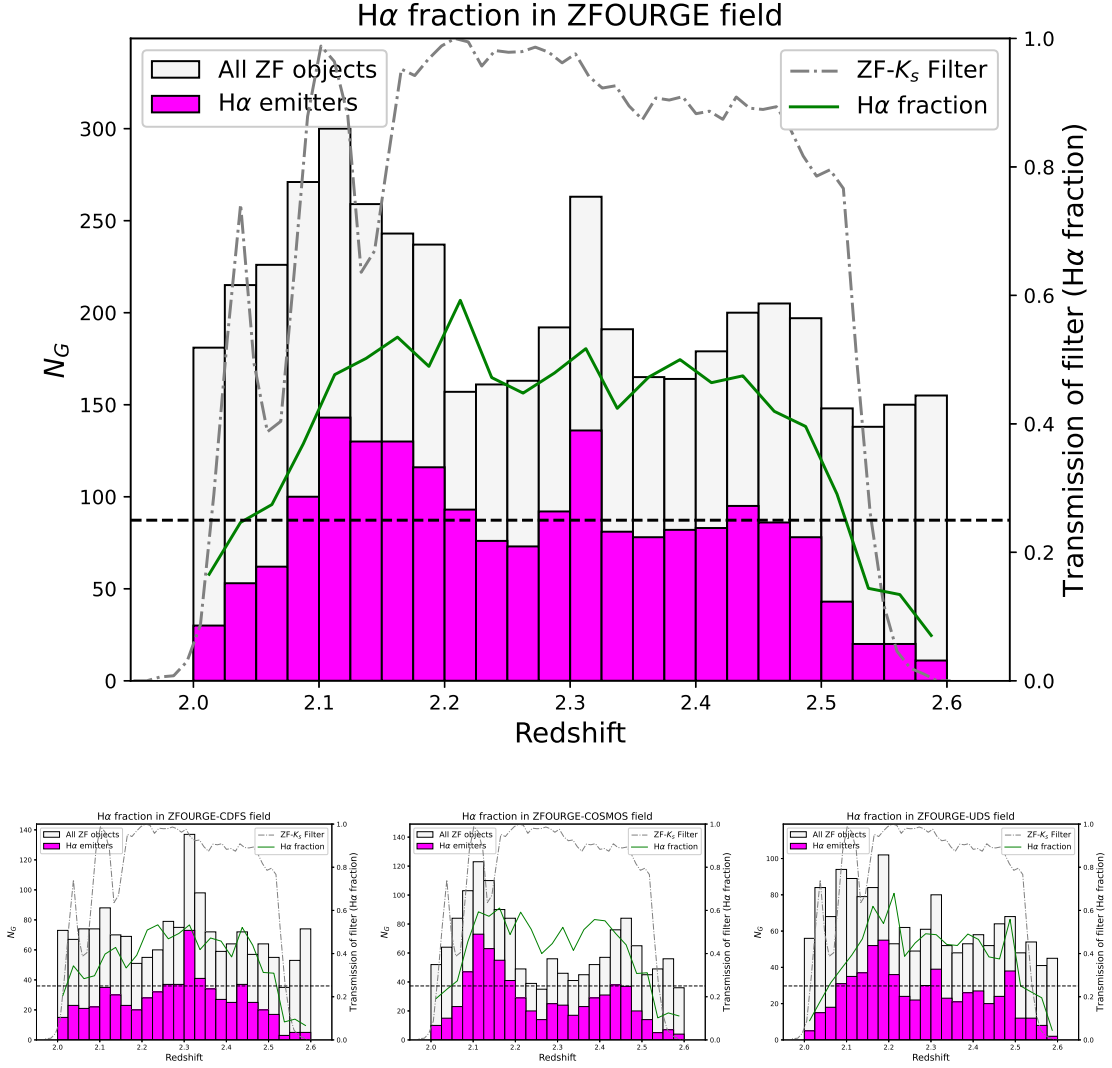


Figure 11. Top: Redshift distributions of all the 4761 galaxies at $2.0 < z < 2.6$ from the parent sample. Galaxies are separated into histograms in redshift bins with steps of 0.025. Magenta and grey histograms indicate the total number of HAEs and all galaxies in each bin, respectively. Green solid line represents the H α fraction in each bin, while black dashed line is the cutoff H α fraction set as 0.25. The transmission curve of the Fourstar K_s filter are shown as grey dashed-dotted line with wavelength transferred to the redshift of H α emission lines. Bottom: Same as top panel, separated by each ZFOURGE field: CDFS, COSMOS, and UDS field from left to right.

3.5 Reliability of Line Fluxes from SED fitting

In this section, we try to confirm the reliability of emission line fluxes derived by the flux excesses utilizing CIGALE fitting in two ways. First is a monte-carlo simulation in which we generate a large number of mock galaxy SEDs with known H α fluxes and perform SED fitting on them. Then a comparison was made between the input and output. The second is to compare the observed H α , [OIII] and [OII] fluxes derived by our method with those obtained from the spectroscopic MOSDEF Emission-Line Catalog.

3.5.1 SED fitting simulation on mock galaxies

In this test, a simulation was performed on mock galaxy SEDs generated by the CIGALE model. We compare the input H α fluxes with the output H α fluxes to verify whether the input and output match. An overview of the method is given in Figure 12.

In the first step, we select 248 galaxy SEDs from the best-fit results of the ZFOURGE-COSMOS catalog. These selected galaxy SEDs have a model K_s flux excesses twice larger than the observed errors ($> 2\sigma$). During this step, the input H α fluxes ($F_{\text{H}\alpha,\text{in}}$) are defined as the model H α emission line strengths (as the left panel of Figure 9). We subtract the model stellar continuum from the total flux densities to get the value of the input H α fluxes.

In the second step, we add a random error on the flux of each filter for each galaxy SED. The random error follows a Gaussian distribution with the standard deviation equals to the observed flux error. This process is repeated 1000 times for each selected galaxy SED. For each galaxy SED, the Gaussian distribution of the randomized K_s fluxes is recovered to H α fluxes, obtaining a so-called ‘‘input fluctuation’’ ($\sigma_{\text{H}\alpha,\text{in}}$), expressed as $\sigma_{\text{H}\alpha,\text{in}} = r_{\text{H}\alpha} \times \sigma_{K_s} \times \Delta\lambda_{K_s}$, where σ_{K_s} is the standard deviation of the 1000 K_s fluxes with random errors added, i.e, the observed flux error, $\Delta\lambda_{K_s}$ the bandwidth of K_s filter, and $r_{\text{H}\alpha}$ equals to 0.7 from section 3.3. We repeat this for all 248 galaxy SEDs and get 248 input fluctuations corresponding to each input H α flux during this step.

In the third step, we run the CIGALE fitting on these 1000 mock galaxies with the same parameter setting as Table 2 and obtain the best-fit models for each mock galaxies. Then, we derive the mock H α flux of each galaxy by the same method as mentioned in section 3.3. After that, the output H α flux ($F_{\text{H}\alpha,\text{out}}$) is taken as the median of the 1000 mock H α fluxes from the SED fitting, and the output H α flux uncertainty ($\sigma_{\text{H}\alpha,\text{out}}$) is defined as the standard deviation of the 1000 mock H α fluxes. We repeated the third step to the rest of the 247 galaxy SEDs, and finally obtain 248 output H α fluxes and corresponding output H α flux uncertainties.

Figure 12 indicates a flow chart of this simulation. The three consecutive steps above follow the black solid arrows, while the calculations of $F_{\text{H}\alpha,\text{in}}$, $\sigma_{\text{H}\alpha,\text{in}}$ are following the orange dashed arrows during respective steps. After obtaining the input ($F_{\text{H}\alpha,\text{in}}$, $\sigma_{\text{H}\alpha,\text{in}}$) and output ($F_{\text{H}\alpha,\text{out}}$, $\sigma_{\text{H}\alpha,\text{out}}$) of each galaxy SED, we try to compare them individually and statistically, respectively.

We show the SED fitting result of 1000 mock galaxies from an individual observed galaxy SED in Figure 13. The input and output of the simulation are placed

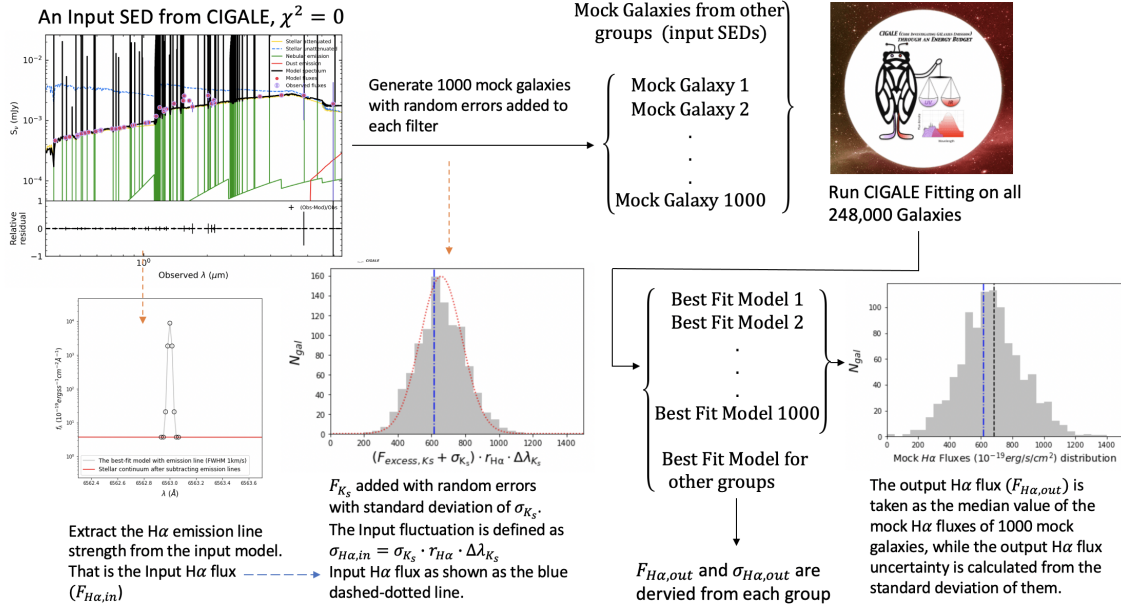


Figure 12. The flow chart of the SED fitting simulation on mock galaxies. It can be split into 3 consecutive steps mentioned in the main text. The parallel computations during the step are pointed with orange dashed lines.

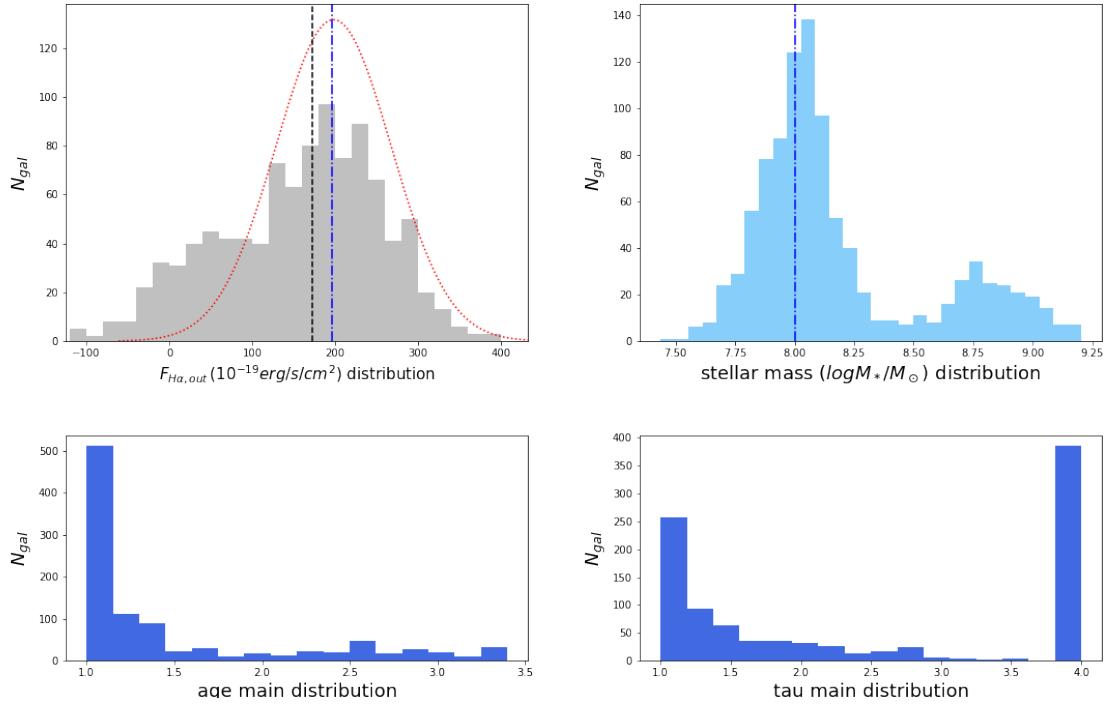


Figure 13. The simulation and SED fitting result of 1000 mock galaxies from one model fitted to an observed galaxy SED (ID: 20415). Top-left: Blue dashed line indicates $F_{H\alpha,in}$ from the observed galaxy SED and red dotted line is the Gaussian distribution of the randomized K_s fluxes, being recovered to H α fluxes. The mock H α fluxes of the 1000 mock galaxies are distributed as the grey histograms, while black dotted line represent $F_{H\alpha,out}$. Top-right: Distribution of the output stellar mass of these 1000 mock galaxies derived from the CIGALE fitting. The stellar mass of the observed galaxy SED is indicated as blue dashed line. Bottom: Distribution of age_main and tau_main of these 1000 mock galaxies derived from the CIGALE fitting.

on the top-left panel, while the distribution of the derived stellar mass of each mock galaxies are presented on the top-right panel. The stellar population age (age_main) and e-folding time (tau_main) of the mock galaxies from the simulated galaxy SEDs are placed on the bottom panels. It is interesting that the H α fluxes and the stellar masses from the simulated galaxy SEDs show a bimodal distribution. The reason for this bimodal distribution is possibly that the simulated galaxy SEDs appear to favour two different galaxy types. This may reflect an underlying degeneracy between these galaxy types when the data is noisy. When inspecting the e-folding time distribution, more than half of the mock galaxies degenerate to a template with tau_main = 10000 Myr and the other half degenerate to a template with tau_main = 10 Myr. The difference in the SFH leads to a bimodal distribution of the H α fluxes and stellar masses. Such phenomenon results in larger output H α flux uncertainties and changes in output H α fluxes. While, such phenomenon is uncommon and do not lead to a large statistical bias. In Appendix D, we also listed some general examples of individual observed galaxy SEDs.

Statistically, we obtain 248 sets of input/output that contain $F_{\text{H}\alpha,\text{in}}$, $\sigma_{\text{H}\alpha,\text{in}}$, $F_{\text{H}\alpha,\text{out}}$, $\sigma_{\text{H}\alpha,\text{out}}$. First, we make a comparison between the input and output H α flux and flux residual (i.e., $\Delta F_{\text{H}\alpha} = (F_{\text{H}\alpha,\text{out}} - F_{\text{H}\alpha,\text{in}})/F_{\text{H}\alpha,\text{in}}$) from each observed galaxy SED in Figure 14. The residuals shows that 90% of our sample (224/248) have a change of H α flux less than 10% and the maximum relative change are within 30%. This result implies that our method can reproduce the input H α to within 10%. Figure 15 shows $\Delta F_{\text{H}\alpha}$ plotted as a function of stellar mass and signal-to-noise (S/N) in the flux excess of K_s (i.e., $\text{S/N} = F_{\text{excess},K_s}/(\Delta f_{K_s} \cdot \Delta\lambda)$). Here, we find no dependence on the stellar mass, while there is a clear dependence on the S/N that objects with larger S/N can reproduce the H α flux much better than others. The outliers ($|\Delta F_{\text{H}\alpha}| > 0.2$) usually have a S/N smaller than 5.

Secondly, we also focus on the difference between the input fluctuation and output flux uncertainty (i.e., $\Delta\sigma_{\text{H}\alpha} = \sigma_{\text{H}\alpha,\text{out}} - \sigma_{\text{H}\alpha,\text{in}}$). $\Delta\sigma_{\text{H}\alpha}$, to some extent, indicates the stability of the SED fitting. In the top-left panel of Figure 13, the red dotted line represents the recovered H α fluxes from the Gaussian noise added on K_s filter, and symbolizes the input fluctuation. While, from the grey histogram, we find that degeneracy to other galaxy types during the SED fitting would broaden the distribution and increase the output flux uncertainties. In comparison, Figure D.1 in Appendix D presents a sample that such degeneracy is barely happening during fitting. A similar distribution of red dotted line and grey histogram is found there.

Figure 16 gives a similar plot that $\Delta\sigma_{\text{H}\alpha}$ as a function of stellar mass and S/N in the flux excess of K_s . Here, we find an obvious correlation between $\Delta\sigma_{\text{H}\alpha}$ and the stellar mass, that high-mass galaxies have much larger $\Delta\sigma_{\text{H}\alpha}$. A possible explanation is that galaxies with higher stellar mass possesses a much complicated star-formation history, since they are older than the low-mass galaxies. This leads to a higher possibility of degeneracy to other templates instead of the template for the best-fit model. On the other hand, the correlations between the changes of flux deviations and S/N in K_s filter are not clear for our sample.

In conclusion, we show that the CIGALE fitting is capable of deriving the correct H α flux from the flux excesses in K_s filter since the relative change is smaller than 10% for most of the input models.

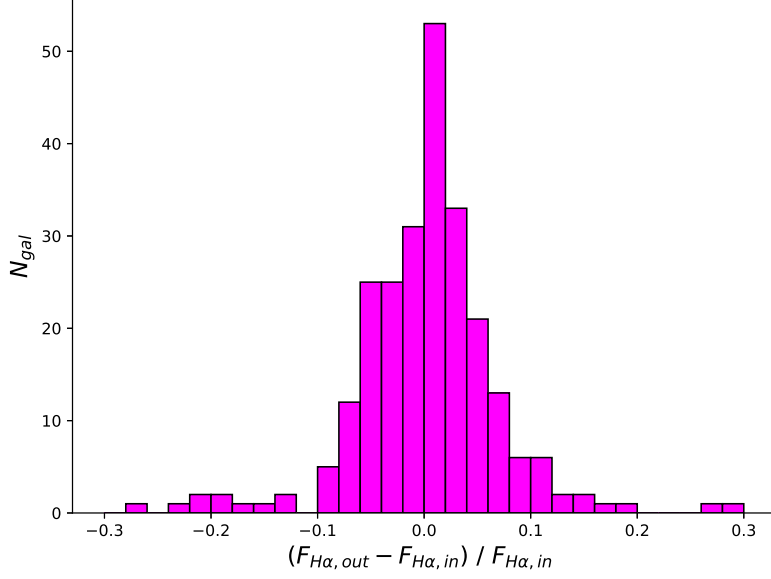


Figure 14. The 248 sets of the relative change of the H α flux, $\Delta F_{\text{H}\alpha}$ are separated into the histogram with steps of 0.02 from -0.3 (30%) to 0.3 (30%). Most of the fitting results are focuses within the region of -0.1 to 0.1, which means that the changes of H α flux are less than 10%.

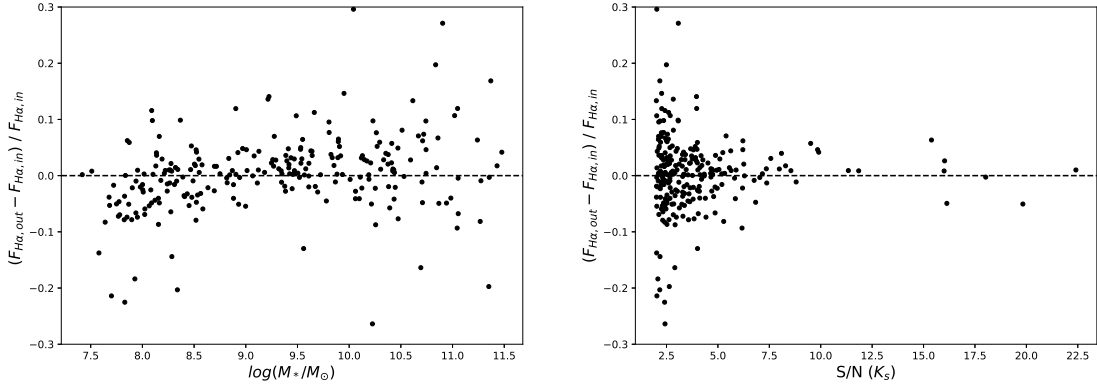


Figure 15. $\Delta F_{\text{H}\alpha}$ and its physical dependence on the stellar mass (left) and signal to noise (right). Right: Since the input model have a criterion of $S/N > 2$, the minimum value of the x -axis is 2.

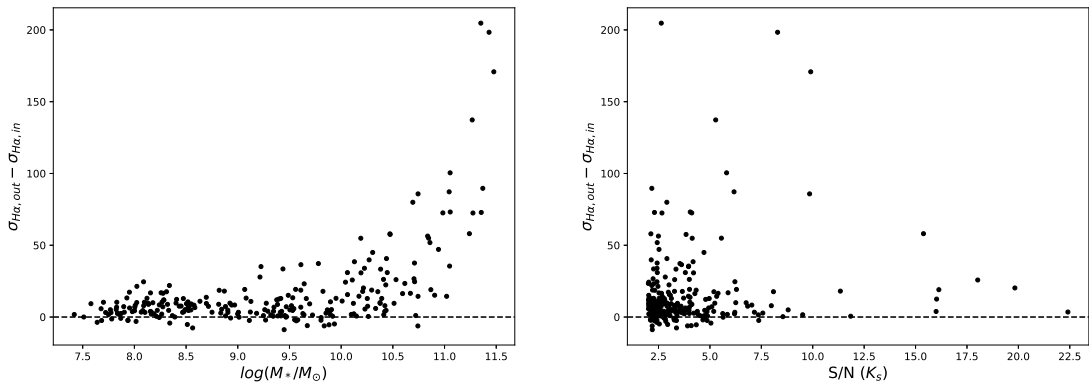


Figure 16. $\Delta \sigma_{\text{H}\alpha}$ and its physical dependence on the stellar mass (left) and signal to noise (right). Right: Since the input model have a criterion of $S/N > 2$, the minimum value of the x -axis is 2.

3.5.2 Flux comparisons with spectroscopic data

Here, we compare the observed $H\alpha$, $[OIII]$ and $[OII]$ fluxes derived by our method (F_{phot}) with the observed flux from the MOSDEF Emission-Line Catalog (F_{spec} , Kriek et al. 2015). A total of 122 galaxies at $2.05 < z < 2.5$ in ZFOURGE-COSMOS field have been observed in the MOSDEF survey by cross-matching within $< 0''.5$. Among them, 90 objects are classified as $H\alpha$ emitters by our method that the flux excesses in the K_s are 2σ larger than photometric errors. Figure 17 shows the spatial distribution of these 122 galaxies and 90 HAEs with a special marker. Moreover, we separate these galaxies into histograms according to their spectroscopic $H\alpha$ flux in the left panel. It is found that all galaxies with spectroscopic $H\alpha$ fluxes larger than $10^{-16} \text{ erg s}^{-1} \text{ cm}^{-2}$ are classified as HAEs by our method, while the non-detected galaxies have relatively low spectroscopic $H\alpha$ fluxes. This finding, in another aspect, proves the robustness of our method to identify and reproduce most of the galaxy with strong emission lines.

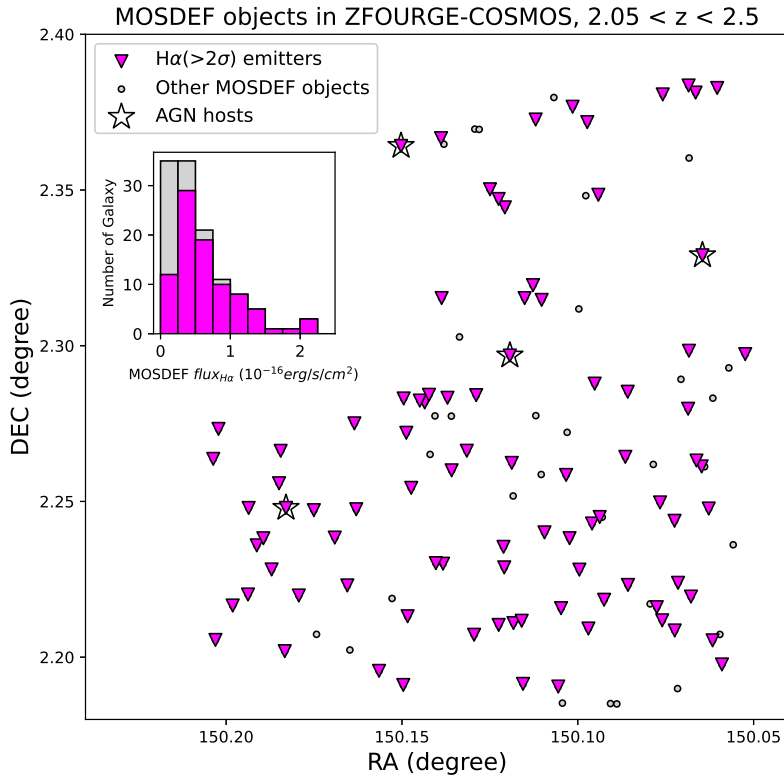


Figure 17. Spatial distribution of cross-matched MOSDEF objects in the ZFOURGE-COSMOS field. Galaxies being classified as $H\alpha$ emitters are marked as magenta triangles, while other objects are marked as grey circles. Galaxies are separated into histograms on the left corner according to their observed $H\alpha$ fluxes from the MOSDEF catalog with steps of $0.25 \times (10^{-16} \text{ erg s}^{-1} \text{ cm}^{-2})$. Among the 90 HAEs, 4 of them have an AGN host, marked as stars.

In the next step, we try to compare the observed emission line fluxes of these 86 HAEs (4 AGN have been excluded as in Figure 17). Figure 18 shows a comparison of the $H\alpha$ fluxes between our method and the MOSDEF catalog. We find that 66/86

(77%) of the H α emitters have consistent values within a factor of 2, and 80/86 (93%) within a factor of 3. Moreover, the median scatter around the one-to-one relation is $F_{phot}/F_{spec} = 1.052$, which implies that the flux from SED is 5% larger than the flux from MOSDEF. The former finding indicates that the H α fluxes derived from the flux excesses between the observed flux and the flux of stellar continuum from SED are robust. The latter finding indicates that the supposed $r_{H\alpha} = 0.7$ (see section 3.3) is dependable and cause almost no bias (only 5%) on the comparison.

The color gradient of individual galaxies corresponds to their stellar masses are added in the figure. These 86 HAEs have a median stellar mass of $\log(M_*/M_\odot)_{med} = 9.8$. From the one-to-one relation, there are 6 outliers which have 3 times larger SED-derived H α fluxes than those from spectroscopy. It is found that these outliers possess larger stellar masses ($\log(M_*/M_\odot)_{med} = 10.6$) than others. A possible explanation is that the assumed ionization parameter of $\log U = -2$ seems too large for galaxies with large stellar mass, leads to an overestimate of emission line strengths in the SED fitting. Another explanation is that galaxies with larger stellar mass are more sensitive to various templates from SED as was shown in the left panel of Figure 16 since they are older and usually have more complicated SFH.

When comparing [OIII] and [OII] emission line fluxes of the 86 HAEs, we need to make a further selection that the [OIII] ([OII]) flux should be detected in both methods: they must have a $> 2\sigma$ flux excess from our method as well as a positive value in the MOSDEF catalog. The additional selection criterion leads to 56 (54) counterparts in [OIII] ([OII]). The one-to-one relation of the [OIII] ([OII]) fluxes between our method and the MOSDEF catalog are exhibited on the left (right) panel of Figure 19.

For the HAEs with [OIII] detection, we find that 38/42 (90%) of the [OIII] fluxes have consistent values within a factor of 2, and 40/42 (95%) within a factor of 3. The median scatter around the one-to-one relation of [OIII] is $F_{phot}/F_{spec} = 0.940$, which implies that the flux from SED is 6% smaller than the flux from MOSDEF. It could be concluded that the [OIII] fluxes derived from the flux excesses with the exclusion of the contamination from H β are robust.

Meanwhile, there are 28/40 (70%) of the [OII] fluxes have consistent values within a factor of 2, and 36/40 (90%) within a factor of 3. The median scatter of [OII] is $F_{phot}/F_{spec} = 0.951$, which implies that the flux from SED is 5% smaller than the flux from MOSDEF. Because [OII] emission lines are often weaker than [OIII] emission lines in SFGs, the flux errors of [OII] from the MOSDEF catalog are larger than those of [OIII]. This may result in a more scattered one-to-one relation in the right panel. However, we can still conclude that the SED-derived [OII] fluxes are dependable and the assumption of $r_{OII} = 0.7$ results in little bias on the comparison.

Similarly, when we are checking the outliers which have 3 times larger SED-derived [OIII] or [OII] fluxes than those from spectroscopy survey, it is also found that these outliers are much more massive than others. The possible explanations are already stated above.

Finally, we conclude that there is no significant systematic error when deriving the H α , [OIII], [OII] fluxes by our method and the SED-derived fluxes have very good agreement with those from spectroscopic survey. It suggests the emission line fluxes estimated by the flux excesses are robust.

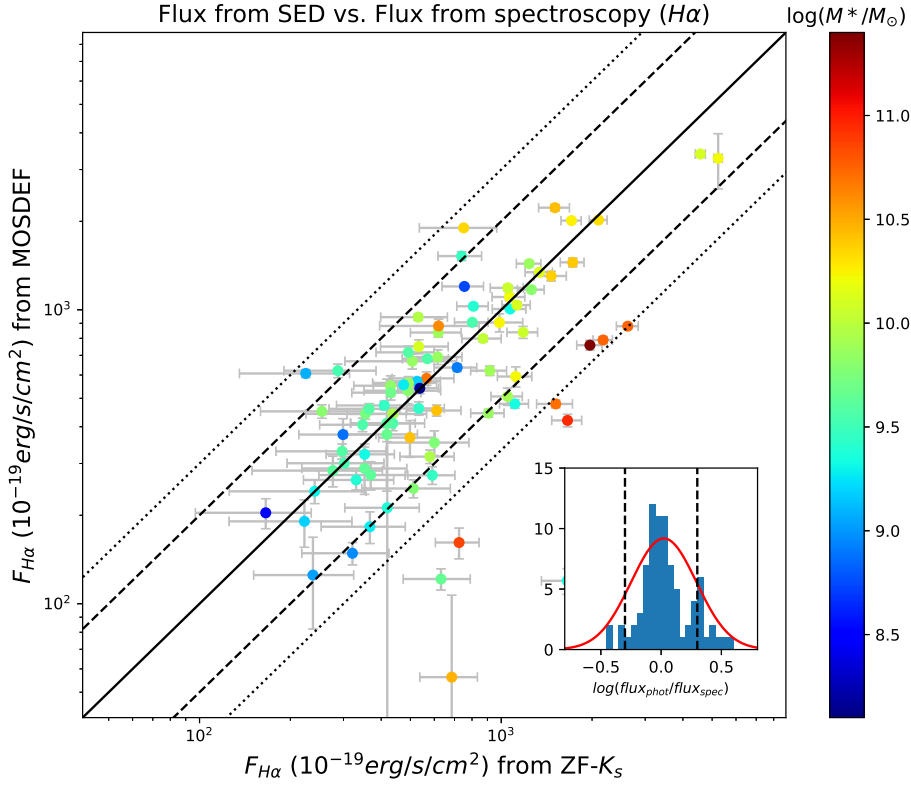


Figure 18. Comparison between the observed $H\alpha$ fluxes derived from SED fitting and those from the MOSDEF Emission-Line Catalog (Kriek et al. 2015). Black dashed (dotted) line indicates a consistency with a factor of 2 (3), respectively. The errorbars on the y -axis implies the flux errors from the MOSDEF catalog, while the errorbars on the x -axis is those from our method. Galaxies are separated into histograms on the lower right corner according to their scatters around the one-to-one relation. Here, the flux ratios (F_{phot}/F_{spec}) are scaled to log-space with steps of 0.05 and black dashed lines (a factor of 2) are added. The color gradient of dots shows the stellar mass of individual galaxy.

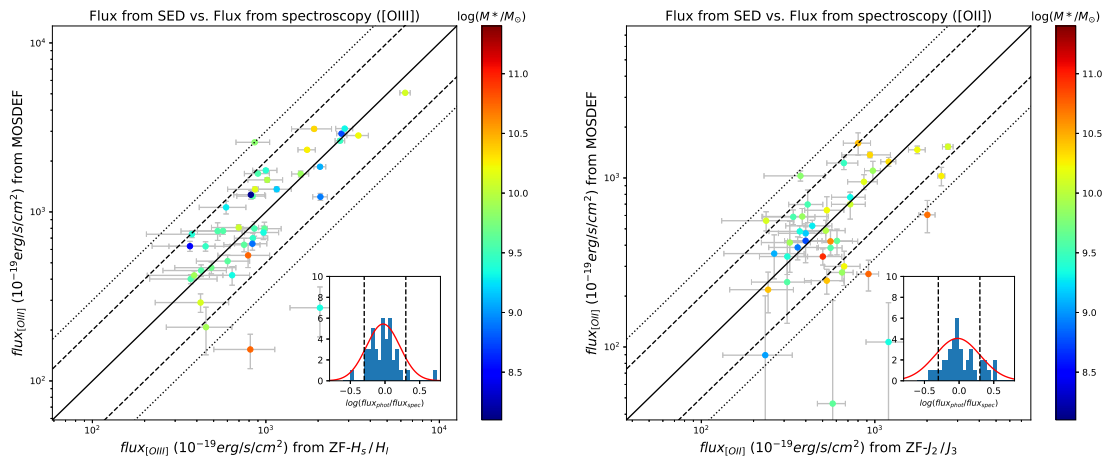


Figure 19. Left: Comparison between the observed $[OIII]$ fluxes derived from SED fitting and those from the MOSDEF Emission-Line Catalog (Kriek et al. 2015). Right: Same but for the observed $[OII]$ fluxes. Outlines as in Figure 18.

3.6 The ZFOURGE HAEs catalog

We provide an H α emitters catalog for the three ZFOURGE field. The total number of HAEs is 1815 with redshift at $2.05 < z < 2.5$ (see section 3.4). The catalog contains the coordinates, observed emission line fluxes, flux uncertainties and SED derived properties such as stellar mass, dust attenuation. Individual sources are indicated by their ID, which is identical to the ZFOURGE catalog. A description of the columns is given in Table 3.

Table 3. Explanation of the HAEs catalog header

Column	Header	Explanation
1	id	ZFOURGE ID number
2	Field	Field name (CDFs, COSMOS, UDS)
3	ra, dec	right ascension, declination (J2000) same as ZFOURGE
4	redshift	z_{phot} from EAZY; if z_{spec} exists, set as z_{spec}
5	f_Ha_obs	H α emission line flux ($10^{-19} \text{ erg s}^{-1} \text{ cm}^{-2}$)
6	f_Ha_obs_err	1σ dispersion in emission line flux of H α
7	LHa_obs	Observed H α emission line luminosity (erg s^{-1})
8	LHa_obs_err	1σ dispersion in observed H α emission line luminosity
9	A_Ha	Dust extinction of H α emission line (mag)
10-14		Same as columns 9-14 for [OIII] emission line
14-19		Same as columns 9-14 for [OII] emission line
20	A_V	Dust extinction of stellar continuum at $\simeq 0.55 \mu\text{m}$ (mag)
21	age	Stellar population age (Myr)
22	tau	The e-folding time of the main stellar population (Myr)
23	sfr_Ha	Star formation rate from the intrinsic H α luminosity
24	agn	Sources that match Cowley et al. (2016) AGN catalog are set to 1

Here, the observed luminosity of H α emission line is calculated from the SED-derived H α flux (f_Ha_obs in the catalog) as follows, same for other emission lines,

$$L_{\text{H}\alpha, \text{obs}} (\text{erg s}^{-1}) = F_{\text{H}\alpha, \text{obs}} \times 4\pi D_L^2, \quad (15)$$

where D_L is the luminosity distance corresponding to the redshift of each galaxy.

The SED fitting gives the color excess of the stellar continuum, $E(B-V)_{star}$, of each galaxy. The A_V in the catalog is obtained from the Calzetti curve ($R_V = 4.05$; Calzetti et al. 2000) as Equation (4). On the other hand, accounting for the fact that the amount of dust attenuation for the emission lines are different from that for the stellar continuum (see section 3.2.3), we adopt the Galactic extinction curve ($R_V = 3.1$; Cardelli et al. 1989) for the emission lines, but parametrize the amplitude of color excess by a factor of $f = 0.44 + 0.2z$ (Saito et al. 2020) as Equation (9). Follow these rule, we obtain the dust extinction of H α , [OIII] and [OII], respectively and have the median dust extinction of H α at $A_{\text{H}\alpha, \text{med}} = 0.43$ mag.

Using the A_Ha, we can derive the intrinsic H α luminosity (H α luminosity corrected for the dust attenuation) as,

$$L_{\text{H}\alpha, \text{int}} (\text{erg s}^{-1}) = L_{\text{H}\alpha, \text{obs}} \times 10^{A_{\text{H}\alpha}}. \quad (16)$$

Finally, the star formation rate can be converted from the intrinsic $H\alpha$ luminosity using the calibration of [Kennicutt \(1998\)](#) with a correction to the [Chabrier \(2003\)](#) IMF. Since low-mass stars do not contribute significantly to the $H\alpha$ luminosity, only the mass-to-light ratio is changed when the [Chabrier \(2003\)](#) IMF is adopted instead of the [Salpeter \(1955\)](#) IMF. This leads to a decrease in SFR by a factor of 1.7 ([Pozzetti et al. 2007](#)) because of there are fewer low-mass stars created. The expression are as follows,

$$\text{SFR}(H\alpha) (M_{\odot} \text{ yr}^{-1}) = \frac{7.9 \times 10^{-42}}{1.7} \times L_{H\alpha, int} (erg s^{-1}). \quad (17)$$

In addition, the age and tau in the catalog are both obtained from the SED fitting. The agn are matched the catalog of X-ray-selected, IR-selected, and radio-selected AGN hosts from [Cowley et al. \(2016\)](#). Among the 1815 HAEs in our catalog, 35 of them contain AGN hosts. After excluding them, we finally have a sample of 1780 $H\alpha$ emitters at $z_{med} = 2.25$ with stellar masses spanning the range $\log(M_*/M_{\odot}) = 7.3 - 11.5$ and SFRs ranging from 1.0 to 440 $M_{\odot} \text{ yr}^{-1}$. The median stellar mass and $\text{SFR}(H\alpha)$ of the sample is $\log(M_*/M_{\odot})_{med} = 9.3$ and 8.6 $M_{\odot} \text{ yr}^{-1}$, respectively.

4 PHYSICAL PROPERTIES OF H α EMITTERS

In this section, we try to figure out various physical properties of the 1780 HAEs included in our catalog, especially focus on the low-mass HAEs which haven't clearly studied before.

4.1 H α luminosity function

In order to derive the luminosity function of the HAEs, we first calculate the volume and number density of our survey. Considering the redshift range $2.05 < z < 2.5$ and the total coverage of ZFOURGE survey (see section 2.1), we obtain that our H α survey probes a (comoving) volume of $\Delta V = 6.8 \times 10^5 \text{ Mpc}^3$. Then number density in each luminosity bin is calculated as follows,

$$\phi^*(\log(L_c)) = \frac{1}{\Delta(\log L)} \sum_{|\log \frac{L_i}{L_c}| < \frac{\Delta(\log L)}{2}} \frac{1}{\Delta V}, \quad (18)$$

where $\log(L_c)$ is the central luminosity in each bin, $\Delta(\log L)$ is the step of each bin and $\log(L_i)$ is the H α luminosity of each galaxy in \log_{10} space. In this work, we set the bin width $\Delta(\log L) = 0.25$ and $\log(L_c)$ start from 42.0 to 44.0. Terao (2020) calculated the H α completeness of the ZFOURGE survey that more than 95% completeness is obtained for galaxies with $L_{\text{H}\alpha} > 10^{42.25} \text{ erg s}^{-1}$, where the H α luminosity is corrected for attenuation by dust. We adopt this estimation of H α completeness and exclude the lowest luminosity bin when fitting the luminosity function.

Based on these prerequisites, we can determine the best-fit H α luminosity function of our HAEs at $z_{\text{med}} = 2.25$. The luminosity function are fitted with Schechter functions (Schechter 1976), defined by three parameters, α , ϕ^* and L^* . In the \log_{10} space, the Schechter function is given by,

$$\phi(L) dL = \ln 10 \phi^* \left(\frac{L}{L^*} \right)^\alpha e^{-(L/L^*)} \left(\frac{L}{L^*} \right) d\log L, \quad (19)$$

where ϕ^* is the normalization density, L^* is a characteristic galaxy luminosity where the power law form of the function cuts off, and α is the power law slope at low luminosity. The Schechter functions are fitted to each bin of $\log(L_c)$ except the first one, and the best fits for the H α luminosity function are presented in Figure 20 and Table 4.

In Figure 20, we provide two best-fit curve (solid line) with different colors. One is the result if AGNs is included and the other excluded. It is found that AGNs leads to obvious contamination in our work, which contribute to $\sim 14\%$ of the total H α luminosity and cause an excess at the bright end of the luminosity function.

After excluding AGNs, we also add two former studies for comparison. Sobral et al. (2013) derive the H α luminosity function from star-forming galaxies in the High-redshift(Z) Emission Line Survey (HiZELS, A narrow-band imaging survey; Geach et al. 2008; Sobral et al. 2009). The other study, Terao (2020), makes use of the ZFOURGE data and calculate the flux excess in the K_s filter using the same

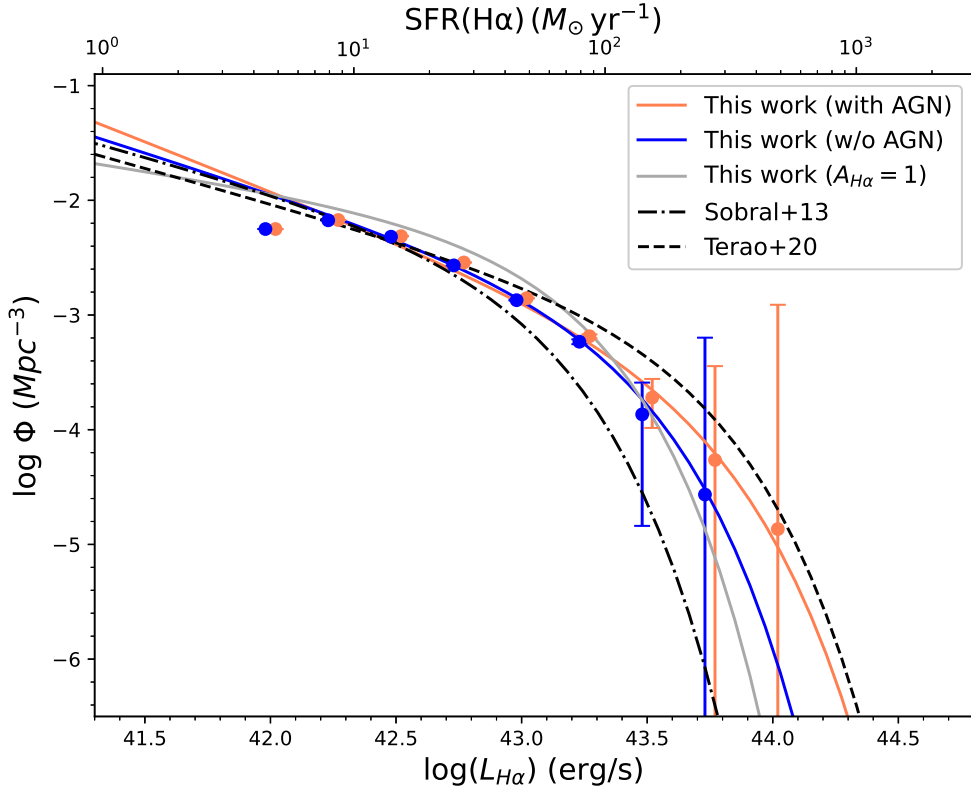


Figure 20. The $H\alpha$ luminosity function of our sample. The orange dots and curve illustrates the best-fit luminosity function when including the AGNs, while the blue dots and curve gives the result of 1780 HAEs when removing the AGNs. The best-fit curve from Sobral et al. (2013) and Terao (2020) are also included for comparison, which are shown by the black dashed-dotted curve and the black dashed curve, respectively. On the other hand, the best-fit luminosity function when assuming a same $A_{H\alpha} = 1$ mag for all our HAEs are presented as the grey curve. The parameters of the Schechter function for each best-fit curve with are summarized in Table 4.

method as ours, but by a different SED fitting code, FAST (Kriek et al. 2009). It is interesting that the bright end of the $H\alpha$ luminosity function from our work (the blue solid line) falls in between the former two works. One explanation is that, though we use the same method of deriving $H\alpha$ fluxes as Terao (2020), FAST often produce a lower stellar continuum than CIGALE and may lead to an overestimate of $H\alpha$ fluxes. This will result in an excess at the bright end. A comparison between CIGALE and FAST are given in Appendix C.

Another factor which causes the difference at the bright end of the luminosity function may be the treatment of the dust attenuation, as discussed in Terao (2020). Sobral et al. (2013) have assumed $A_{H\alpha} = 1$ mag for all the galaxies and this assumption may lead to an underestimate of the intrinsic $H\alpha$ luminosity of the brightest HAEs, which usually have $A_{H\alpha} > 1$ mag from our SED-derived dust correction. The grey solid line in Figure 20 indicates the best-fit Schechter function if we employ the same assumption of $A_{H\alpha} = 1$ mag as Sobral et al. (2013) to our sample. It is found that the excess is reduced at bright end, while an overestimate of number density is appeared in the intermediate region. On the other hand, Terao (2020) corrected

dust extinction by using a relation between A_V derived from the infrared excess (IRX) and the SED fitting. Then, A_V is converted to $A_{H\alpha}$ by using the Calzetti curve again. The difference between the dust correction methods in Terao (2020) and our work may also lead to the discrepancy of the $H\alpha$ luminosity function.

Table 4. The best-fit parameters of $H\alpha$ luminosity functions at $z \sim 2.3$

	$\log L_{H\alpha}^*$ (erg s^{-1})	$\log \phi_{H\alpha}^*$ (Mpc^{-3})	α	$\log \rho L_{H\alpha}$ ($\text{erg s}^{-1} \text{Mpc}^{-3}$)
This work (with AGN)	43.52	-3.58	-1.85	–
This work (w/o AGN)	$43.22^{+0.03}_{-0.03}$	$-3.13^{+0.06}_{-0.08}$	$-1.69^{+0.06}_{-0.06}$	$40.54^{+0.11}_{-0.18}$
This work ($A_{H\alpha} = 1$)	42.99	-2.59	-1.33	–
Sobral et al. (2013)	42.87	-2.78	-1.59	40.43
Terao (2020)	43.50	-3.30	-1.61	40.55

Notes. The cosmic $H\alpha$ luminosity density, $\log \rho L_{H\alpha}$, is integrated from $L_{H\alpha} = 0$ to $10^{45} \text{ erg s}^{-1}$. We do not display the cosmic star formation rate density here, since various IMF lead to different calibration.

Finally, we integrate our $H\alpha$ luminosity function from the faint end to the bright end with a range of $L_{H\alpha} = 0 - 10^{45} \text{ erg s}^{-1}$, and obtain the cosmic $H\alpha$ luminosity density at $z_{med} = 2.25$ to be $\log \rho L_{H\alpha} (\text{erg s}^{-1} \text{Mpc}^{-3}) = 40.54^{+0.11}_{-0.18}$. Assuming a Salpeter IMF (Salpeter 1955) as used in Madau & Dickinson (2014), the cosmic $H\alpha$ luminosity density is translated to the cosmic star formation density (CSFRD) of $\log \psi (\text{M}_{\odot} \text{yr}^{-1} \text{Mpc}^{-3}) = -0.56^{+0.11}_{-0.18}$ as in Figure 21. This results agrees well with the literature based on $H\alpha$ observations (e.g, Sobral et al. 2013; Terao 2020). It is clear that we obtain an almost identical result as Terao (2020) because both studies select the same sky field and method of selecting HAEs, though SED-fitting codes and treatments of dust correction are different. However, the result is larger than most compiled UV & IR data (e.g, Cucciati et al. 2012; Gruppioni et al. 2013), and the best-fit CSFRD curve by a factor of 2 (~ 0.3 dex) from Madau & Dickinson (2014).

Both the bright end (constrained by L^*) and the faint end (constrained by α) of the luminosity function contribute a lot in the cosmic $H\alpha$ luminosity density. For example, Sobral et al. (2013) made a truncation at $L_{H\alpha, \text{int}} \simeq 10^{41.6} \text{ erg s}^{-1}$ (the observed luminosity limit of HiZELS survey), and the faint end contribute to about 1/3 of the total $H\alpha$ luminosity. Because of the observation limit, the faint end of the $H\alpha$ luminosity function at $z > 2$ is still unclear, and is usually obtained from the extrapolation of the best-fit Schechter function of those brighter objects. The uncertainty on the faint end of the $H\alpha$ luminosity function may leads to a discrepancy of the CSFRD.

On the other hand, the coverage and total volume of the ZFOURGE survey is much smaller than other wide-field-surveys, such as HiZELS, HSC-SSP. This may result in a large uncertainty on the normalization density ϕ^* in the luminosity function. Hayes et al. (2010) fitted the $H\alpha$ luminosity function in GOODS-S field and obtain a set of Schechter parameters with similar L^* and α , but smaller ϕ^* than our

work. It is reasonable to deduce that the difference in CSFRD is caused by the bias of survey volume that the ZFOURGE field may possess a larger number of brighter H α emitters and leads to an excess in the CSFRD.

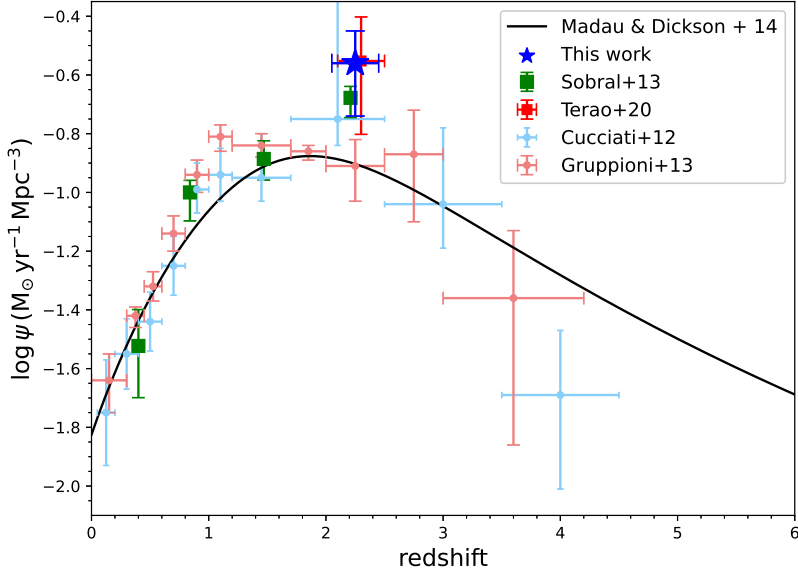


Figure 21. The cosmic star formation rate density (CSFRD) after excluding AGN are marked as blue star. The H α -derived CSFRD from Sobral et al. (2013) and Terao (2020) are shown as green squares and red square for comparison, respectively. Black solid line is the evolution of the CSFRD from Madau & Dickinson (2014). The light blue and coral circles represent a part of UV & IR results from literature (e.g, Cucciati et al. 2012; Gruppioni et al. 2013), summarized in Madau & Dickinson (2014).

4.2 Star formation rate and Star formation main sequence

The correlation between stellar mass (M_*) and SFR of galaxies has been studied intensively since Brinchmann et al. (2004). It is found that star formation galaxies, including HAEs, usually hold a correlation between M_* and SFR, called the “star formation main sequence” (SFMS) at least up to $z \sim 3$. In Figure 22, we show this correlation between SFR(H α) and stellar mass for the 1780 HAEs in our catalog. The larger circles represent the median SFR(H α) in seven mass bins (the first bin is $\log(M_*/M_\odot) < 8.0$, the last bin is $\log(M_*/M_\odot) > 10.5$ and the rest are divided by 0.5 dex widths).

From Straatman et al. (2016), the ZFOURGE survey have an 80% mass completeness of $\log(M_*/M_\odot) \sim 9$ at $z \sim 2$ and $\log(M_*/M_\odot) \sim 9.5$ at $z \sim 4$. Since the median redshift of our HAEs is $z_{med} = 2.25$, and we want to have a slightly higher completeness to avoid missing too much emitters with relatively low equivalent widths, we take the completeness limit of the stellar mass as $\log(M_*/M_\odot) = 9.2$. On the other hand, Whitaker et al. (2014) suggests that galaxies with $\log(M_*/M_\odot) < 10.2$ evolve in a different SFMS whose slope is consistently steeper than the high-mass slopes because the SMBH feedback may be contributing to the quenching of

star formation in these massive systems (The negative feedback; e.g., [Fabian 2012](#); [Kormendy & Ho 2013](#)). Therefore, to avoid any biases, we limited the fitting of SFMS to those with stellar mass $9.2 < \log(M_*/M_\odot) < 10.2$. Although the stellar mass range is limited, we still have 753 galaxies with $9.2 < \log(M_*/M_\odot) < 10.2$ applied to the fitting. Finally, the linear regression fitting gives us a relation presented in [Table 5](#) and blue solid line in [Figure 22](#).

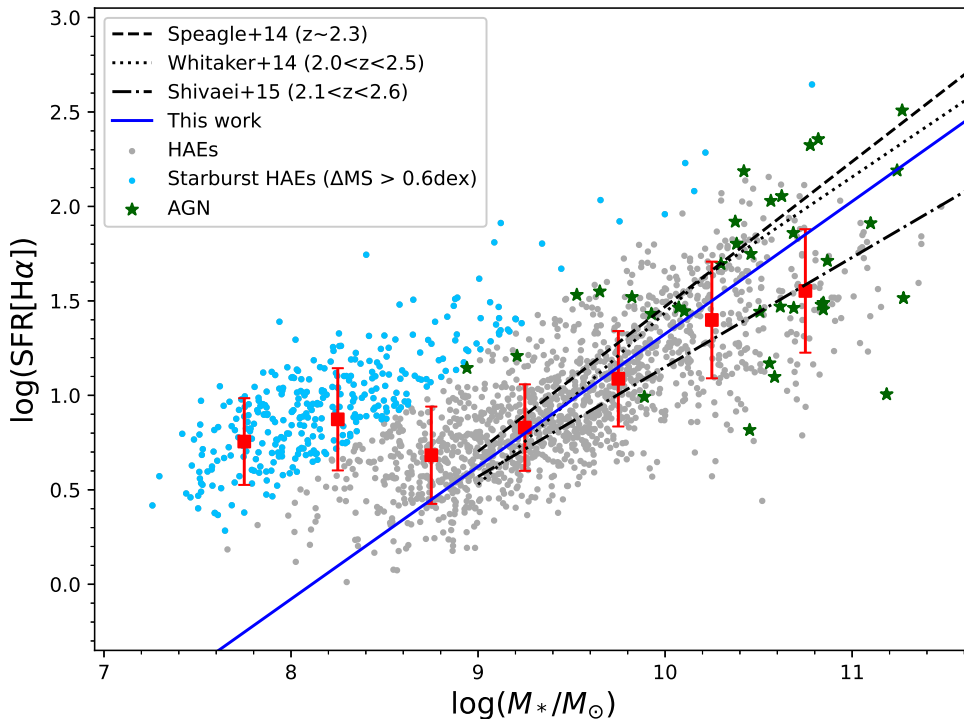


Figure 22. The star formation main sequence of HAEs at $z_{med} = 2.25$ in the ZFOURGE field. Grey dots show the HAEs in our catalog $\Delta MS < 0.6$ dex, while cyan points are starburst HAEs with $\Delta MS > 0.6$ dex. Red squares are stacks in seven mass bins, while the error bars on them represent the standard deviation in each mass bin. Blue solid line is the best linear fit to the galaxies with $9.2 < \log(M_*/M_\odot) < 10.2$. The best-fit SFMS from [Whitaker et al. \(2014\)](#), [Speagle et al. \(2014\)](#) and [Shivaei et al. \(2015\)](#) are also shown with dotted, dashed, and dot-dashed lines, respectively. AGNs are marked as green stars for comparison, though they are excluded from the fitting of SFMS.

In [Figure 22](#), we plot additional three SFMS lines from literature as references. [Speagle et al. \(2014\)](#) determined the redshift-evolution SFMS using a compilation of 25 studies, [Whitaker et al. \(2014\)](#) combined the ultraviolet (UV) and infrared (IR) data to derive the SFMS at $2.05 < z < 2.5$, and [Shivaei et al. \(2015\)](#) obtained the SFMS from HAEs in the MOSDEF survey. It is found that the slope of our study is shallower than those of [Speagle et al. \(2014\)](#) and [Whitaker et al. \(2014\)](#) but steeper than [Shivaei et al. \(2015\)](#). Several factors may influence the slope of the SFMS including sample bias and dust correction. Firstly, the MOSDEF survey may have a sample selection bias that lacks dusty star-forming galaxies, which may result in the steeper slope. In contrast, the other surveys including our study, possess much

larger samples and do not suffer from selection bias. Secondly, dust correction in Speagle et al. (2014), Shivaiei et al. (2015) and our study are different from one another. Whitaker et al. (2014) estimated the total SFR as the sum of UV and IR based SFRs, while Shivaiei et al. (2015) corrected H α emission line using the nebular color excess computed from the Balmer decrement. On the other hand, our study transfer the SED-derived $E(B - V)_{star}$ to $E(B - V)_{neb}$ by a factor of f , and adopt the Galactic extinction curve for emission line correction. In Appendix E, we present the SFMS of various dust attenuation recipes used in SED fitting. It is found that, dust correction leads to a remarkable difference on the slope of SFMS. Also, Shivaiei et al. (2015) found a slope of SFMS close to unity if correcting the H α emission line with the SED-derived $E(B - V)_{star} \times 2.27$ with the assumption of the Calzetti curve. Although the dust correction leads to a shallower slope in our study, the discrepancies between our study and Whitaker et al. (2014) is not large. Therefore, it can still be concluded that our study have a good agreement with former studies and there is no obvious systematic errors on the SFMS obtained from SFR(H α) of the HAEs with $9.2 < \log(M_*/M_\odot) < 10.2$.

In this work, we also derive the SFR(UV) of galaxies from the attenuation corrected rest-frame FUV (1500Å) luminosities (L_{1500}). We adopt the Calzetti curve ($R_V = 4.05$; Calzetti et al. 2000) and the SED-derived color excess, $E(B - V)_{star}$, for the dust correction at 1500Å. L_{1500} is expressed as follow,

$$L_{1500} (erg s^{-1}) = \nu f_{\nu,1500} \cdot \frac{4\pi D_L^2}{(1+z)} \cdot 10^{0.4 A_{1500}}. \quad (20)$$

where $f_{\nu,1500}$ is the flux density of the closest grids to rest-frame 1500Å from the CIGALE best-fit model for each galaxy and D_L is the luminosity distance corresponding to the redshift of each galaxy. The luminosities were then converted to SFRs using the calibration by Theios et al. (2019),

$$\text{SFR(UV)} (M_\odot \text{ yr}^{-1}) = 3.46 \times 10^{-44} \times L_{1500} (erg s^{-1}). \quad (21)$$

We also obtain the SFMS using SFR(UV) of our HAEs with stellar mass $9.2 < \log(M_*/M_\odot) < 10.2$. The relation is also presented in Table 5. We obtain nearly the same slope as (but slightly steeper than) that of SFR(H α), which supports the reliability of both methods. A further comparison between SFR(H α) and SFR(UV) is shown in Figure 23, which was also done in Terao (2020).

The SFMS from Table 5 only reach a mass limit of $\log(M_*/M_\odot) \sim 9$ at $z \sim 2$, due to the observational limit. However, in virtue of the ultra-deep K_s image from ZFOURGE, we are able to take a glance at the low-mass end ($\log(M_*/M_\odot) < 9$) of the SFMS in our study. At the low-mass end, Terao (2020) found a large number of galaxies significantly up-scatter above the prediction from the extrapolation of the SFMS, which is also seen in our analysis. Similar population of HAEs are also mentioned in literature (e.g., Hayashi et al. 2016). Although we cannot discuss the exact locations of the SFMS at $\log(M_*/M_\odot) < 9$ due to the incompleteness of sample, these galaxies substantially have much higher specific star formation rates ($s\text{SFR} = \text{SFR}/M_*$) than the intermediate/high-mass galaxies. It is really interesting to investigate the physical properties of these low-mass HAEs in our

Table 5. The best-fit parameters of SFMS at $z \sim 2.3$

	SFR indicator	slope	intercept
This work (with AGN)	$H\alpha_{\text{cor}}$	0.69 ± 0.03	-5.66 ± 0.27
This work (w/o AGN)	$H\alpha_{\text{cor}}$	0.70 ± 0.03	-5.69 ± 0.27
This work (w/o AGN)	UV_{cor}	0.72 ± 0.04	-5.84 ± 0.41
Speagle et al. (2014)	–	0.77 ± 0.03	-6.20 ± 0.32
Whitaker et al. (2014)	UV + IR	0.91 ± 0.06	-7.66 ± 0.63
Shivaei et al. (2015)	$H\alpha_{\text{cor}}$	0.58 ± 0.10	-4.65 ± 1.05

Notes. The best-fit parameters of slope and intercept from [Whitaker et al. \(2014\)](#) are taken from the low-mass regimes. The SFMS of [Speagle et al. \(2014\)](#) is resulted from a compilation of 25 studies with various methods.

sample because the high sSFRs may suggest that they are young starburst galaxies just being formed. Considering the star formation enhancements typical of starburst events, we here define starburst galaxies in our sample to be located 0.6 dex above the extrapolated SFMS, i.e, $\Delta\text{MS} > 0.6$ dex, as [Cibinel et al. \(2019\)](#). This selection leads to a subsample of 333 galaxies, and among them 306 galaxies have stellar mass of $\log(M_*/M_\odot) < 9$. These starburst HAEs are marked as cyan dots in Figure 22 and in subsequent figures, to be distinguished from other HAEs. Statistically, the median ΔMS of these samples is 0.91 dex, and $\Delta\text{MS} = 0.92$ dex for the low-mass ($\log(M_*/M_\odot) < 9$) subsample.

The left panel of Figure 23 indicates the relation between $\text{SFR}(H\alpha)$ and $\text{SFR}(UV)$ of the HAEs in our catalog, with the color gradient of their stellar masses. It is found that most of the low-mass galaxies have larger $\text{SFR}(H\alpha)$ than $\text{SFR}(UV)$. Similar result was also found by [Terao \(2020\)](#) that most of the galaxies with $\log(M_*/M_\odot) < 9$ have very high $\text{SFR}(H\alpha)/UV$ ratios, while few massive galaxies show such high ratios.

As mentioned in section 1.1, different SFR indicators have different timescales that are ~ 100 Myr for $\text{SFR}(UV)$ and ~ 10 Myr for $\text{SFR}(H\alpha)$. Thus, if a galaxy experiences a recent starburst, the $\text{SFR}(H\alpha)/\text{SFR}(UV)$ ratio is higher than that in normal SFGs during the burst and the ratio is depressed 10 Myr after the end of the burst, as was also simulated in [Sparre et al. \(2017\)](#); [Flores Velázquez et al. \(2021\)](#). This finding further proves that these low-mass galaxies are undergoing or have undergone instantaneous starburst events within the past 10 Myr. Analogous low-mass starburst objects in the local universe, such as blue compact dwarf (BCD), also usually have larger $\text{SFR}(H\alpha)$ SFRs than UV SFRs ([Janowiecki et al. 2017](#)), which further prove the starburst feature in our low-mass HAEs.

In addition, we plot the relation between the $\text{SFR}(H\alpha)/\text{SFR}(UV)$ ratio and the location on the SFMS, ΔMS , for each galaxy in the right panel of Figure 23. It is interesting that we discover two branches with the increase of the $\text{SFR}(H\alpha)/\text{SFR}(UV)$ ratio. The first branch is the galaxies located on the SFMS, where the less massive one tends to have the higher ratio until $\log(M_*/M_\odot) \simeq 9$ which is the completeness

limit of our survey. The second branch is the low-mass galaxies scattered above the SFMS, where the $\text{SFR}(\text{H}\alpha)/\text{SFR}(\text{UV})$ ratio is correlated to the ΔMS , and ΔMS increases with the higher ratio. Meanwhile, along the second branch, the increase of ΔMS saturates at ~ 1.2 dex. This indicates that these galaxies may reach the maximum of sSFR, lead to the limiting production of ionizing photons.

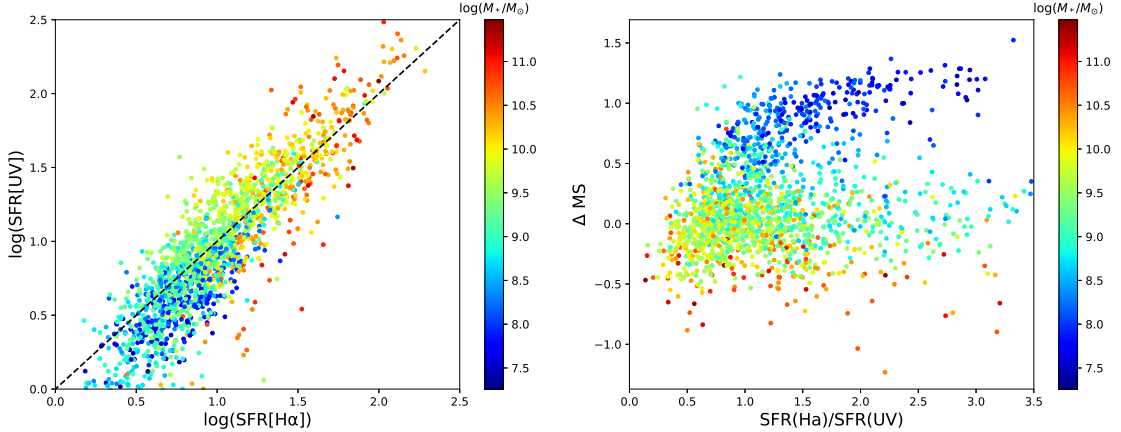


Figure 23. Left: Relation between the $\text{SFR}(\text{H}\alpha)$ and $\text{SFR}(\text{UV})$ of the HAEs in our sample. The color gradient reflects the stellar mass of each galaxy. Right: The ratio of $\text{SFR}(\text{H}\alpha)$ to $\text{SFR}(\text{UV})$ compare with the location on the SFMS, ΔMS , for each galaxy. The color gradient are same as in the left panel.

In conclusion, we find that the low-mass HAEs in our sample are undergoing or have undergone very strong starburst events, result in higher $\text{SFR}(\text{H}\alpha)/\text{SFR}(\text{UV})$ ratios and scattering above the star formation main sequence.

4.3 Strong emission line ratios

In this and subsequent section, we further explore the properties of our HAEs with multiple emission lines. In virtue of the deep ZFOURGE MB data, $[\text{OIII}]$ and $[\text{OII}]$ emission lines are derived from the flux excess in the ZFOURGE H_s/H_l and J_2/J_3 filter. Here, we assume the Case-B recombination and estimate the intrinsic $\text{H}\beta$ fluxes from the intrinsic $\text{H}\alpha$ fluxes.

On the other hand, $[\text{NII}]$ is blended with $\text{H}\alpha$ in K_s flux excess and hard to be extracted because the ratio of $[\text{NII}]/\text{H}\alpha$ is relatively scattered in both local universe and high-redshift universe. Although it is possible to apply a stellar mass correlated $[\text{NII}]/\text{H}\alpha$ ratio, this relation is distinct from that in the local universe (Topping et al. 2021) and needed to further explored. Anyway, we do not further extract $[\text{NII}]$ from the flux excess in this work. This issue is actually the limitation of our method that deriving emission line fluxes from the broad-band flux excess.

As a result, available frequently-used multiple emission-line ratios in our study are,

$$\text{O32} = [\text{OIII}]\lambda 5007 / [\text{OII}]\lambda\lambda 3726, 29, \quad (22)$$

$$\text{R}_{23} = ([\text{OIII}]\lambda\lambda 4959, 5007 + [\text{OII}]\lambda\lambda 3726, 29) / \text{H}\beta. \quad (23)$$

Since the O32 line ratio only consider $[\text{OIII}]\lambda 5007$, we need to extract $[\text{OIII}]\lambda 5007$ from the $[\text{OIII}]$ doublets, $[\text{OIII}]\lambda\lambda 4959, 5007$. We adopt the transition probabilities of $[\text{OIII}]\lambda 5007$ and $[\text{OIII}]\lambda 4959$ from [Osterbrock \(1989\)](#), and take the line ratio of $[\text{OIII}]\lambda 4959 : [\text{OIII}]\lambda 5007 = 1 : 3$.

Among the 1780 HAEs in our catalog, 733 galaxies have detection of $[\text{OIII}]$ emission lines ($> 2\sigma$ in flux excess) and further 388 galaxies have both detection of $[\text{OIII}]$ and $[\text{OII}]$. Usually, $[\text{OII}]$ are weaker than $[\text{OIII}]$ lines by several factors in SFGs at high redshift. In order to avoid selection bias, we include all the galaxies with detection of $[\text{OIII}]$, while set 1σ error for the non-detection of $[\text{OII}]$ for further discussion. Moreover, 210 of these 733 HAEs are starburst galaxies and 185 of them have stellar mass of $\log(M_*/M_\odot) < 9$. An overview of these subsamples are presented in [Table 6](#).

Table 6. The summary of galaxy numbers and properties for the subsamples

Sample (Detected lines)	N_{gal}	$\log(M_*/M_\odot)_{med}$	$\text{SFR}(\text{H}\alpha)_{med}$ ($M_\odot \text{ yr}^{-1}$)
All ZFOURGE HAEs ($2.05 < z < 2.5$)	1780	9.29	8.60
HAEs ($\text{H}\alpha$, $[\text{OIII}]$)	733	9.21	9.75
HAEs ($\text{H}\alpha$, $[\text{OIII}]$, $[\text{OII}]$)	388	9.48	12.98
Starburst HAEs ($\text{H}\alpha$)	333	8.12	8.68
Starburst HAEs ($\text{H}\alpha$, $[\text{OIII}]$)	210	8.27	9.94
Low-Mass Starburst ($\text{H}\alpha$)	306	8.08	8.28
Low-Mass Starburst ($\text{H}\alpha$, $[\text{OIII}]$)	185	8.21	8.97

Notes. Detection of $\text{H}\alpha$, $[\text{OIII}]$ and $[\text{OII}]$ need that the flux excess in K_s has $\text{S/N} > 2$. The starburst HAEs are defined as $\Delta\text{MS} > 0.6$ dex, while the low-mass HAEs are defined as $\log(M_*/M_\odot) < 9.0$.

We first investigate the empirical trends between multiple emission-line ratios and stellar mass. [Figure 24](#) presents O32, R_{23} vs. M_* for the 733 HAEs in our subsample. Considering the number of subsample in each bin, we separate the subsample into six mass bins with steps of 0.5 dex, from the first bin $\log(M_*/M_\odot) < 8.0$ to the last bin $\log(M_*/M_\odot) > 10.0$. The number of galaxies in each mass bin with the stellar mass, SFR and line ratios are given in [Table 7](#). Here, we also show two results from literature for reference. One is the $z \sim 0$ star-forming galaxies from the composite spectra of [Andrews & Martini \(2013\)](#). More than 20 million galaxies at $z \approx 0.087$ from the SDSS ([York et al. 2000](#)) DR7 MPA-JHU ([Abazajian et al. 2009](#)) are selected with the derived stellar masses ([Kauffmann et al. 2003](#)). The spectra of these galaxies were stacked in stellar mass bin with steps of 0.1 dex. We take the stacks with $\log(M_*/M_\odot) > 8.0$ because lack of spectrum leads to large uncertainties below this mass. Another reference is the composite spectra of $z \sim 2.3$ galaxies ([Sanders et al. 2021](#)) from the MOSDEF survey ([Kriek et al. 2015](#)) with stellar masses from the 3D-HST catalog ([Skelton et al. 2014](#); [Momcheva et al. 2016](#)). About 300 galaxies are separated into five mass bins from $\log(M_*/M_\odot) = 9.3$ to 10.6.

The MOSDEF $z \sim 2.3$ sample would be one of the best references since this redshift range is almost same as our study, though it only contains more massive galaxies. We find that, for galaxies with stellar mass $\log(M_*/M_\odot) > 9.0$, both line ratios basically decrease with increasing M_* , though the slope of R_{23} is relatively flatter than that of O32. It is very impressive that the line ratios of the intermediate/high-mass galaxies from our sample is very close to those of the MOSDEF $z \sim 2.3$ sample. In contrast, galaxies with stellar mass $\log(M_*/M_\odot) < 8.5$, most of which are starburst HAEs, maintain a similar O32 and R_{23} . When compared with the emission-line ratios in the local universe, in the intermediate/high-mass regime, both line ratios are significantly higher at $z \sim 2.3$ than at $z \sim 0$. It is also found that the emission-line ratios of the SDSS sample seem to be saturated at high-mass regime. At $z \sim 2$, such saturation at high M_* is observed in the R_{23} ratio while not in the O32 ratio. When moving to the low-mass regime, it is really interesting to find that the O32 ratio at $z \sim 0$ continue to increase with the decrease of stellar mass, which is different from our low-mass sample at $z \sim 2$. Since these low-mass galaxies at high redshift have not detailed studied before, we will further focus on this issue after calibrating the line ratios to galaxy properties.

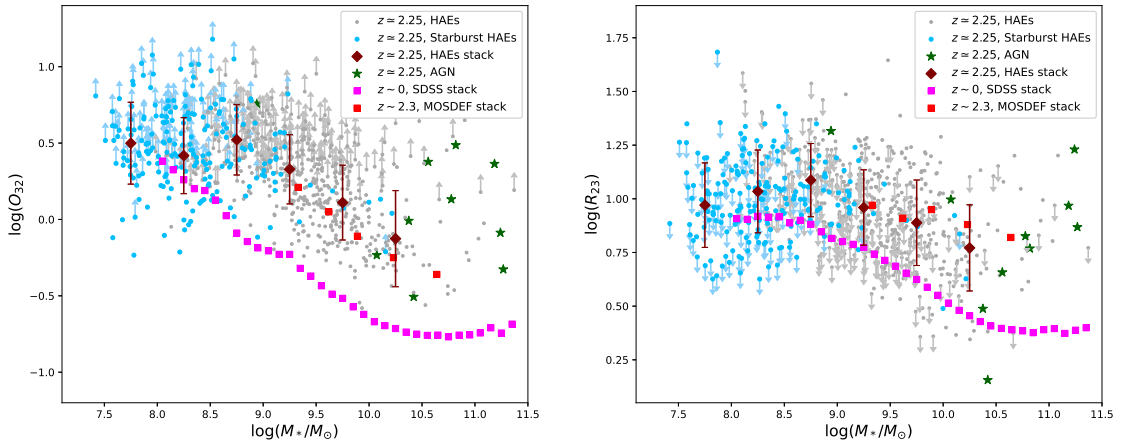


Figure 24. Left: Reddening-corrected emission-line ratios O32 vs. M_* for HAEs at $z \sim 2.3$. The main sequence HAEs are presented as grey dots and the starburst HAEs as cyan triangles as Figure 22. The M_* -stacked result of HAEs are indicated as large maroon squares with error bars which display the standard deviation of the individual galaxies in each mass bin. Magenta squares show the $z \sim 0$ spectra stacks of Andrews & Martini (2013) with steps of 0.1 dex in each mass bin, while red squares the spectra stacks of the MOSDEF $z \sim 2.3$ sample from Sanders et al. (2021) for reference. Also, AGNs are marked as the green stars for comparison. Right: Same as left panel but for R_{23} .

4.4 The MZR and FMR at $z \sim 2.3$ with empirical calibration

We here utilize the emission-line ratios to estimate the oxygen abundance (metallicity) in our analysis by the metallicity calibration of Bian et al. (2018), which is based on local analogs of high-redshift galaxies. Bian et al. (2018) selected a sample of SDSS galaxies lies on the $z \sim 2$ star-forming galaxy sequence in the [NII] BPT

Table 7. Properties and Emission-line Ratios from stacks in each mass bin

Stack	N_{gal}	$\log(M_*/M_\odot)$	$\text{SFR}(\text{H}\alpha)$ ($M_\odot \text{ yr}^{-1}$)	$\log(\text{O32})$	$\log(\text{R}_{23})$	$12 + \log(\text{O}/\text{H})$
Normal	523	9.45	9.70	0.26	0.94	8.32
Starburst	210	8.27	9.94	0.46	1.00	8.20
< 8.0	57	7.79	6.46	0.50	0.97	8.18
8.0-8.5	112	8.27	7.67	0.42	1.03	8.22
8.5-9.0	128	8.79	7.49	0.52	1.09	8.16
9.0-9.5	187	9.27	8.72	0.33	0.96	8.28
9.5-10.0	178	9.70	13.49	0.11	0.89	8.41
> 10	71	10.24	35.27	-0.13	0.77	8.54

Notes. $\log(M_*/M_\odot)$, $\text{SFR}(\text{H}\alpha)$, $\log(\text{O32})$, $\log(\text{R}_{23})$ and $12 + \log(\text{O}/\text{H})$ are taken as the median value in each mass bin. $12 + \log(\text{O}/\text{H})$ are calibrated from O32. $\text{SFR}(\text{H}\alpha)_{med}$ is different from the red square in Figure 22 because $\text{SFR}(\text{H}\alpha)_{med}$ here is calculated from the subsample with detection of $\text{H}\alpha$, [OIII], [OII].

diagram, which might have similar ionized ISM properties as high-redshift galaxies. A significant offset of metallicity calibration is found between these local analogs and normal SDSS galaxies (e.g., Jones et al. 2015), primarily due to the change of ionized ISM conditions. For O32, the Bian et al. (2018) calibration is as follows,

$$12 + \log(\text{O}/\text{H}) = 8.47 - 0.59 \times \text{O32}, \quad (24)$$

note that Bian et al. (2018) used the line ratio of [OIII] $\lambda\lambda$ 4959, 5007 for calibration, so we here decrease the y-intercept of this equation by $0.59 \times \log(4/3) \simeq 0.07$ dex.

While R_{23} is commonly employed as a metallicity indicator in the local universe, we do not use it to estimate for reasons described below. R_{23} is double valued in terms of the metallicity (Kewley & Dopita 2002), with the turnaround region at $0.8 \leq \log(\text{R}_{23}) \leq 1.0$. The majority of our HAEs with stellar mass $\log(M_*/M_\odot) \leq 10.0$ lie in this region, where small observational uncertainties will lead to large uncertainties in measuring metallicity. As a result, we only show the metallicity from O32 calibration in the main text.

Comparison between the galaxy properties of the normal HAEs and starburst HAEs are listed in Table 7. It is found that oxygen abundance of the starburst HAEs are ~ 0.15 dex lower than that of normal HAEs. This means larger amount of pristine (metal-poor) gas in starburst systems, results in a higher sSFR.

As mentioned in section 1.2.3, there exists a correlation between the stellar mass of galaxies and the ISM metallicity such that more massive galaxies have higher metallicity, known as the Mass-Metallicity Relation (MZR) at least to $z \sim 3.5$. It is also known that oxygen abundance decrease with the increase of redshift at fixed M_* (e.g., Erb et al. 2006; Mannucci et al. 2009; Onodera et al. 2016; Suzuki et al. 2017; Sanders et al. 2018). In Figure 25, we present the MZR at $z \sim 2.3$ from our

HAEs, which is consistent with that at $z \sim 2.3$ from MOSDEF (Sanders et al. 2021) in the intermediate/high-mass regime of $\log(M_*/M_\odot) > 9.0$.

Furthermore, most of the starburst HAEs (blue triangles) with stellar mass $\log(M_*/M_\odot) > 9.0$ have smaller metallicity than normal HAEs with similar stellar mass. This further proves the relation between metallicity and sSFR that galaxies with higher SFR has lower metallicity (e.g., Peeples et al. 2009) and leads to the "M_{*}-SFR-Z" relation, i.e, the Fundamental Metallicity Relation. In Figure 26, we investigate the three-dimensional relation among M_{*}, metallicity, and SFR. We parameterize the FMR in our HAEs with the same method as Mannucci et al. (2010), that apply a combination of M_{*} and SFR to correlate with metallicity as follows,

$$\mu_\alpha = \log(M_*/M_\odot) - \alpha \times \log(\text{SFR}), \quad (25)$$

where α is a free parameter. For $\alpha = 0$, μ_0 corresponds to $\log(M_*/M_\odot)$, i.e, the MZR relation. A well-accepted inferred value of α is $0.55 - 0.7$ (Andrews & Martini 2013; Sanders et al. 2017; Curti et al. 2020). We here adopt $\alpha = 0.6$ ($\mu_{0.6}$) and compare with the best-fit cubic function of FMR from Sanders et al. (2021) based on the $z \sim 0$ spectra stacks of Andrews & Martini (2013),

$$12 + \log(\text{O}/\text{H}) = 8.80 + 0.188y - 0.220y^2 + 0.0531y^3, \quad y = \mu_{0.6} - 10. \quad (26)$$

It is found that the three M_{*}-stacked result ($\mu_{0.6}$) of HAEs with stellar mass $\log(M_*/M_\odot) > 9.0$ located very close to the best-fit $z \sim 0$ FMR, with the maximum offset to the curve of $\Delta\log(\text{O}/\text{H}) = 0.05$ dex. This result further proves that the FMR shows no sign of evolution at least to $z \sim 2.3$ with good precision in the intermediate/high-mass regime.

However, neither the MZR nor the FMR is applicable to those HAEs with stellar mass $\log(M_*/M_\odot) < 8.5$ in Figure 25 and 26, because these HAEs exhibit no evolution in O32 ratio when compared with their higher mass counterparts and result in a same level of metallicity after empirical calibration. When referring to Figure 24, we find that our low-mass HAEs have a similar O32 to local galaxies with same stellar mass ($\log(M_*/M_\odot) < 8.5$) from Andrews & Martini (2013). If applying the same calibration, it means that these low-mass HAEs at $z \sim 2.3$ have a similar metallicity as local galaxies but a higher metallicity than the MZR at $z \sim 2.3$. One explanation for the high metallicity is the environment, which has a secondary effect on the metallicity. It is found that local galaxies in denser environments tend to be more metal rich than galaxies in low density environments (e.g, Peng et al. 2015). Our low-mass HAEs at high-redshift may belong to satellite galaxies around massive galaxies, resulting higher metallicity than MZR. Another explanation is the validity of the O32 calibration in low-mass regime, we will further discuss it in section 5.2.1.

4.5 Photoionization Modeling and ISM ionization states

As O32 emission-line ratio works as a direct diagnostic for ionization parameter, it only has a secondary dependence on metallicity, which is mostly due to the correlation between ionization parameter and metallicity ("U-Z" relation). Moreover, this diagnostic may suffer from large uncertainties at high-redshift because the U-Z

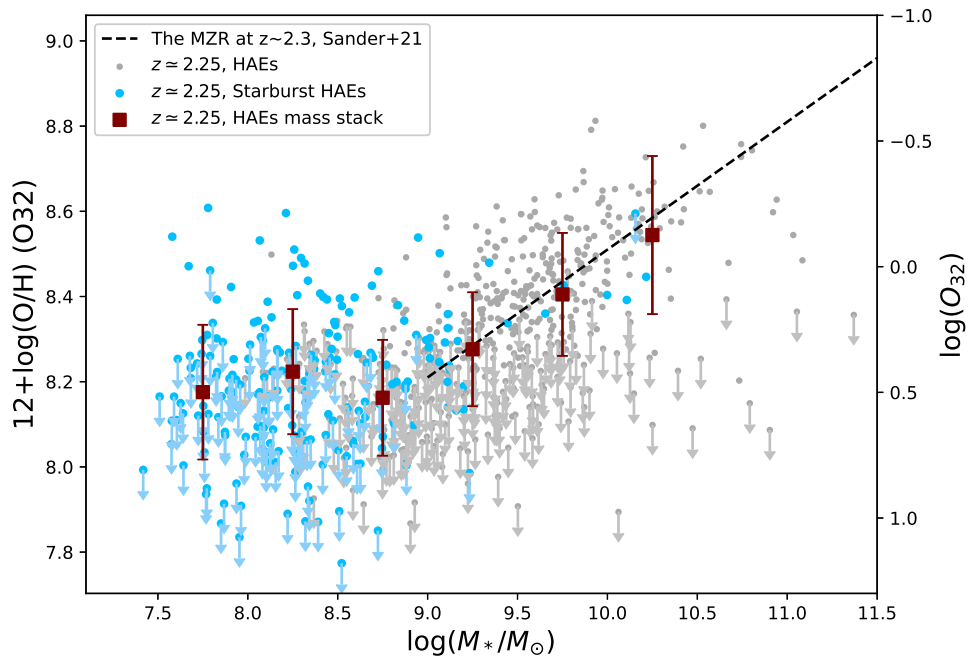


Figure 25. The Mass-Metallicity Relation at $z \sim 2.3$ for the individual galaxies and the M_* -stacked result. Individual points and error bars are the same as in Figure 24. The best-fit MZR at $z \sim 2.3$ from Sanders et al. (2021) are shown as black dashed line for comparison.

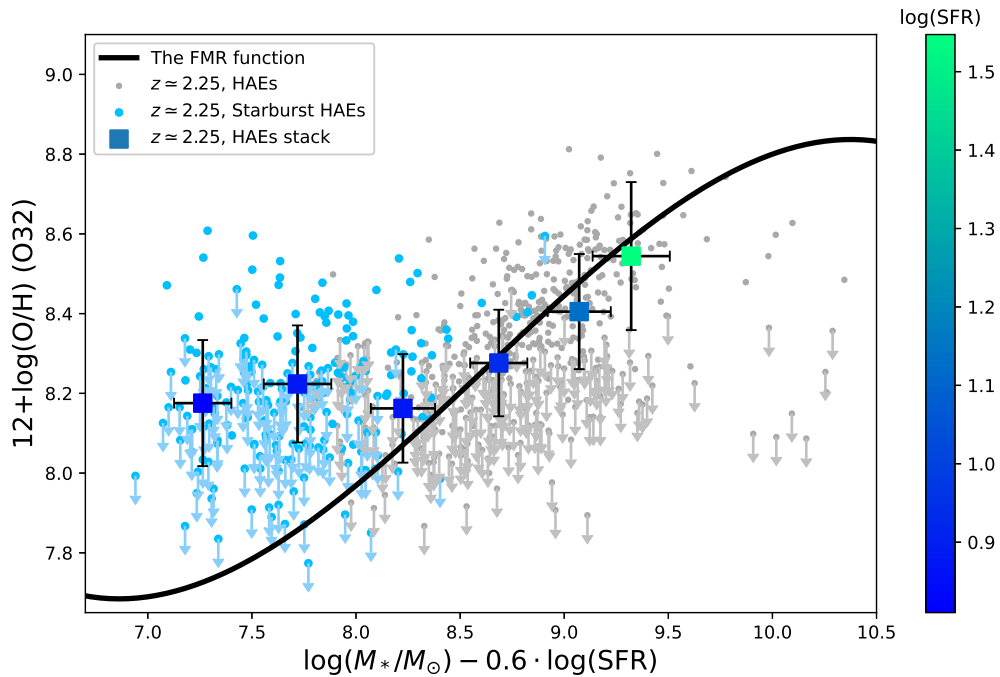


Figure 26. The Fundamental Metallicity Relation at $z \sim 2.3$ for the individual galaxies and the M_* -stacked result. We adopt the coefficient of the linear combination of SFR and M_* as $\alpha = 0.60$. Individual points and y-axis error bars are the same as in Figure 24. Additional x-axis error bars are added based on the standard deviation of SFR. Black solid line is the best-fit cubic function to the $z \sim 0$ stacks from Sanders et al. (2021) as Equation (26).

relation may evolve with redshift (Kewley et al. 2013b). On the other hand, R_{23} is one of the parameters most widely adopted because it directly measure the amount of the main ionization stages of oxygen, O^+ and O^{++} . Still the oxygen abundance calibration curve of R_{23} is dependent on the ionization parameter (Kewley & Dopita 2002; Kobulnicky & Kewley 2004). Usually, an iterative approach is required to resolve these dependencies.

We apply the calibration method, which is introduced by Kobulnicky & Kewley (2004:KK04) based on the photoionization models of Kewley & Dopita (2002). KK04 used strong emission-line ratio R_{23} and O32 to determine the relations between oxygen abundance, and ionization parameters, given by,

$$\begin{aligned} \log(q_{\text{ion}}) = & \{32.81 - 1.153y^2 + [12 + \log(\text{O}/\text{H})] \\ & (-3.396 - 0.025y + 0.1444y^2)\} \\ & \times \{4.603 - 0.3119y - 0.163y^2 + \\ & [12 + \log(\text{O}/\text{H})] (-0.48 + 0.0271y + 0.02037y^2)\}^{-1}, \end{aligned} \quad (27)$$

where $y = \log([\text{OIII}]\lambda\lambda 4959, 5007/[\text{OII}]\lambda\lambda 3726, 29)$. Then, the oxygen abundance $12 + \log(\text{O}/\text{H})$ is separated into the two equations at $12 + \log(\text{O}/\text{H}) = 8.4$,

$$\begin{aligned} 12 + \log(\text{O}/\text{H})_{\text{low}} = & 9.40 + 4.65x - 3.17x^2 \\ & - \log(q_{\text{ion}}) \times (0.272 + 0.547x - 0.513x^2), \end{aligned} \quad (28)$$

$$\begin{aligned} 12 + \log(\text{O}/\text{H})_{\text{high}} = & 9.72 - 0.777x - 0.951x^2 - 0.072x^3 - 0.811x^4 \\ & - \log(q_{\text{ion}}) \times (0.0737 - 0.0713x - 0.141x^2 + 0.0373x^3 - 0.058x^4), \end{aligned} \quad (29)$$

where $x = \log(R_{23})$ and the subscript low (high) corresponds to a metallicity value in the low-Z (high-Z) branch of metallicity.

We compare the metallicity and ionization parameters obtained by the KK04 method with the emission-line ratio of our HAEs in Figure 27. Besides individual galaxies, we also include the median emission-line ratio of normal HAEs and starburst HAEs here as shown in the top two rows of Table 7. Black dotted lines in this Figure are the relations from a photoionization model derived by the iterative method in Kewley & Dopita (2002). Each line represents the relation at a certain ionization parameter q_{ion} , defined by

$$q_{\text{ion}} (\text{cm s}^{-1}) = \frac{Q_{\text{H}^0}}{4\pi R_s^2 n_{\text{H}}}, \quad (30)$$

where Q_{H^0} is the flux of ionizing photons produced by the exciting stars above the Lyman limit, R_s is the Stromgren radius, and n_{H} is the total hydrogen density. Note that in section 3.2.2, we also introduce another ionizing parameter U , which is in a dimensionless form of $U = q_{\text{ion}}/c$.

We further use equations (27) – (29) to estimate the metallicity and ionization parameter of the median emission-line ratio of two populations of HAEs, that are the main sequence HAEs and starburst HAEs, iteratively until the calculation converges. We apply an user-modified open-source Python code, pyMCZ (Bianco et al. 2016), through the Monte Carlo simulation, to characterize the statistical metallicity

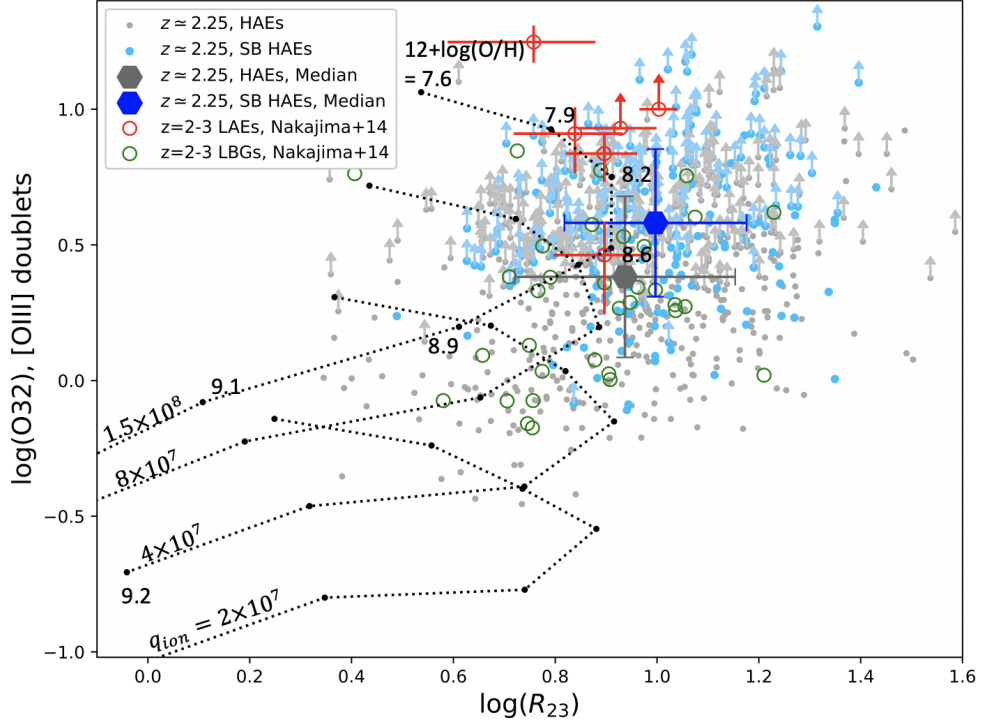


Figure 27. Relation between $[\text{OIII}]\lambda\lambda 4959, 5007/[\text{OII}]\lambda\lambda 3726, 29$ and R_{23} -index for HAEs at $z \sim 2.3$. Individual points are the same as in Figure 22 and Figure 24. Big grey hexagon is the median emission-line ratio of the normal HAEs with $\Delta\text{MS} < 0.6$ dex, while big blue hexagon is the median emission-line ratio of the starburst HAEs. Red and green circles represent the $z = 2-3$ LAEs and LBGs from Nakajima & Ouchi (2014), respectively.

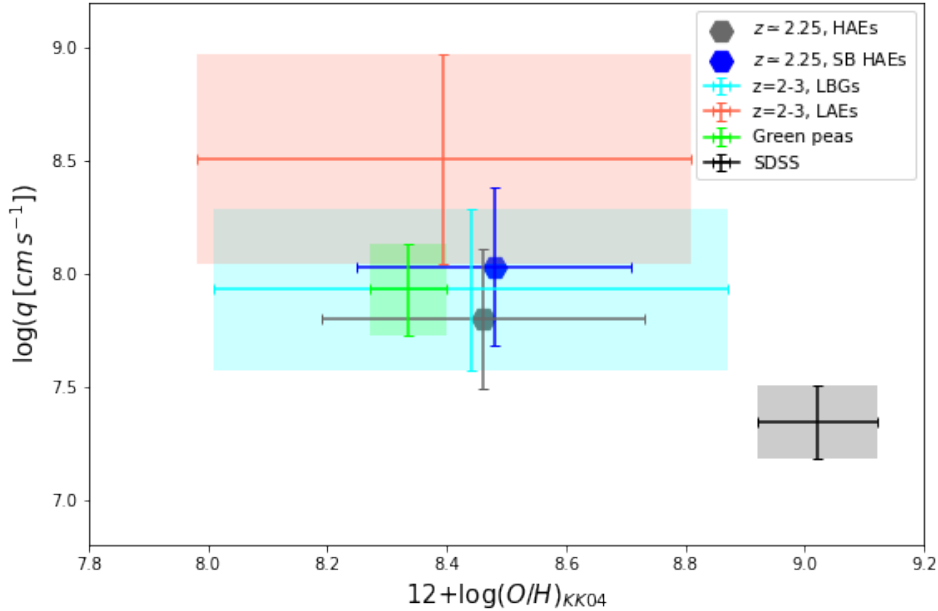


Figure 28. The statistical result of ionization parameter (q_{ion}) and metallicity (oxygen abundance) for our HAEs and galaxy sample from Nakajima & Ouchi (2014) as shown in Table 8. Grey hexagon is the median emission-line ratio of the normal HAEs, while blue hexagon is the median emission-line ratio of the starburst HAEs.

and ionization parameter confidence region due to the propagation of observational uncertainties. For the two median galaxy samples in Figure 27, we obtain their uncertainties by drawing a Gaussian distribution with standard deviation equal to the measurement error, and randomly select a set of R_{23} and $[\text{OIII}]/[\text{OII}]$ ratio following the distributions. The KK04 R_{23} calibration uses the ionization parameter q_{ion} in an iterative fashion to determine the metallicity. We separately iterate the Monte Carlo process 5000 times on the high- Z and low- Z branches, during this step the combined emission-line ratio do not converge to any solution (lie outside of the regions of the photoionization models) are rejected. Then, we combine the two branch solutions together, and define one sigma errors of metallicity and ionization parameter by the standard deviation of the distribution.

In Figure 27, we plot the R_{23} -O32 relation of individual LAEs and LBGs of Nakajima & Ouchi (2014), compiled from previous studies (e.g., Fosbury et al. 2003; Erb et al. 2010; Christensen et al. 2012; Nakajima et al. 2013). Then, Figure 28 and Table 8 present the estimated values of the Monte Carlo simulation of our HAEs and those from Nakajima & Ouchi (2014), which applied a similar Monte Carlo simulation to us. Nakajima & Ouchi (2014) give the distribution of LBGs and LAEs at $2 < z < 3$, and local SDSS galaxies including green Pea galaxies Cardamone et al. (2009). Their results are also presented here for reference.

Table 8. The ionization parameter, $\log(q_{\text{ion}})$, and metallicity, $12 + \log(\text{O}/\text{H})$, distribution

Galaxy Type	$\log(q_{\text{ion}})$	$12 + \log(\text{O}/\text{H})$
$z_{\text{med}} = 2.25$, Normal HAEs	7.55–8.15	8.19–8.73
$z_{\text{med}} = 2.25$, Starburst HAEs	7.68–8.38	8.25–8.71
$z = 2 - 3$, LAEs	8.04–8.97	7.98–8.81
$z = 2 - 3$, LBGs	7.57–8.29	8.01–8.87
Green pea galaxies	7.73–8.13	8.27–8.40
normal SDSS galaxies	7.18–7.51	8.92–9.12

Notes. The distribution of LBGs, LAEs, Green pea galaxies and SDSS galaxies are from Nakajima & Ouchi (2014). For the SDSS sample, only the values in the high- Z branch of R_{23} ($12 + \log(\text{O}/\text{H}) > 8.4$) are given.

We find a slight difference on the metallicity by photoionization models of R_{23} -index and empirical calibration of O32 (section 4.4). O32 calibration gives a result that starburst HAEs have ~ 0.15 dex lower metallicity than normal HAEs, while photoionization models show very similar metallicities of these two types of HAEs. As suggested by Steidel et al. (2014), using the local photoionization models of R_{23} -index do not work well in the metallicity range of $12 + \log(\text{O}/\text{H}) = 8.0$ – 8.7 . Also, Kewley & Ellison (2008) indicated that the metallicities from different calibration methods show systematic offsets up to 0.7 dex, depending on the calibration used. We conclude that this offset are resulted from different calibration methods used and the metallicity from photoionization models of R_{23} -index is not dependable due to the degeneracy of the two-branch solutions.

On the other hand, the difference of ionization parameters between galaxy samples is clearly found in Figure 28. The two types of HAEs shows a slight difference on the ionization parameters that the starburst HAEs have higher ionization parameters than normal HAEs in our sample. When comparing with other types of galaxies, we find starburst HAEs have an ionization parameter higher than the normal SDSS galaxies by a factor of ~ 5 , but lower ionization parameter than that of high- z LAEs. From the large sample of our HAEs catalog, we find that several individual starburst HAEs have a similar emission-line ratio as the 6 LAEs in Nakajima & Ouchi (2014), and these special HAEs which have an extremely strong O32 index may have similar galaxy properties as LAEs. Meanwhile, other starburst HAEs have an ionization parameter as high as high- z LBGs and local green pea galaxies, which indicates similar ionization states of these types of galaxies.

5 DISCUSSION AND IMPLICATIONS

5.1 Main Sequence HAEs

The main sequence HAEs (normal HAEs) take up a large part of HAEs in our sample (1433/1780, and 497/762 with all detection of $H\alpha$, [OIII], [OII]) with a mass completeness at $\log(M_*/M_\odot) \approx 9.2$. Although similar star-forming galaxies have been studied before, it is still interesting to further explore their physical properties.

Modern cosmological hydrodynamic simulations have been impressively successful in reproducing key galaxy properties broadly over cosmic time (e.g., [Kewley et al. 2013a](#); [Somerville & Davé 2015](#); [Davé et al. 2016, 2017](#)). Commonly, various physical processes are included or changed in these simulations of galaxy formation to fit the observation results. On the other hand, recent observation results provide a direct glimpse into the chemical evolution for star formation, leads to a more directly probe of the baryon cycle of gaseous inflows and outflows, which is regarded as the main driver of cosmological galaxy evolution. Cosmological hydrodynamic simulations have utilized these observational results to provide additional constraints on the physical processes of galaxy formation. As a result, observation and simulation are reinforcing each other. [Davé et al. \(2017\)](#) presented an analysis on a suite of cosmological hydrodynamic simulations, called the MUFASA simulations, and provided the star formation, gas mass, chemical evolution of galaxies out to $z \sim 2$. Here, we try to compare our main sequence HAEs to the main results from this simulation.

5.1.1 Star formation rate function

In section 4.1, we derive the luminosity function of our HAEs and obtain an excess at the bright end when comparing with the luminosity function from [Sobral et al. \(2013\)](#). In order to conform to the cosmological hydrodynamic simulations, we transfer the luminosity function to star formation rate function (SFRF) by converting $H\alpha$ luminosity to SFR (Kennicutt calibration, adjusted for a Chabrier IMF).

In the MUFASA simulations, a molecular gas-based star formation prescription (see details in [Krumholz et al. 2009](#); [Thompson et al. 2014](#)) was employed to form stars out of gas, in addition to various quenching feedback models and chemical evolution of 11 elements.

When comparing with the SFRF of $z = 2$ from the MUFASA (see Figure 1 of [Davé et al. 2017](#)) simulations, we find the high-SFR end of our HAEs are in very good agreement with the simulation, and both the high-SFR ends are more populated than other observations. While, as the total volume of the ZFOURGE survey is not large enough and may lead to large uncertainties, it is still difficult to reconcile current SFR measurements among various data sets and the result from simulations.

In the future, we are planning to apply our HAEs selection method to other multi-wavelength photometry catalogs which not only have deep K_s data but also cover wide areas, such as COSMOS2020 catalog ([Weaver et al. 2021](#)) covering across the 2deg^2 of the COSMOS field. It may help us to obtain a much larger HAEs

sample (though multiple emission-line analysis will be difficult) and more credible H α luminosity function and SFRF.

5.1.2 Metallicity, MZR and FMR

Chemical evolution provides a key tracer for star formation and feedback activity in and around galaxies, verifying the accuracy of the baryon cycle in cosmological hydrodynamic simulations. The MUFASA simulations also present the predictions for the gas-phase metallicity and the Mass-Metallicity Relation at $z = 0$ and $z = 2$. A fairly good agreement is obtained between the MZR from MUFASA and observations, such as SDSS and MOSDEF (see Figure 3 of [Davé et al. 2017](#)). An evolution of MZR is also found in the simulation that, at low/intermediate masses, there is ~ 0.25 dex decrease in the metallicity at a fixed M_* from $z = 0$ to $z = 2$, given a evolving rate of $d\log(\text{O}/\text{H})/dz \sim 0.13$ dex.

Similarly, the evolution of MZR is also found in our HAEs sample in Figure 29. We here choose the normal HAEs (grey points in previous figures) and separate them into four mass bins. We take the median values of mass and metallicity in every bin and the best-fit result is given with a single power law in the form,

$$12 + \log(\text{O}/\text{H}) = 0.26 \times \log\left(\frac{M_*}{10^{10} M_\odot}\right) + 8.48. \quad (31)$$

[Sanders et al. \(2021\)](#) also fit the $z \sim 0$ MZR of the SDSS composite spectra of [Andrews & Martini \(2013\)](#) with the parameterization as follows,

$$12 + \log(\text{O}/\text{H}) = 8.87 - \frac{0.25}{3.66} \times \log\left[1 + \left(\frac{M_*}{10^{10.2} M_\odot}\right)^{-3.66}\right]. \quad (32)$$

We find that the MZR in low/intermediate-mass regime ($\log(M_*/M_\odot) < 10.0$) is consistent with a power law at both redshift and the slopes are remarkably consistent to each other. From these two best-fit MZR, we find an evolution of ~ -0.32 dex in O/H from $z \sim 0$ to $z \sim 2.3$, given a evolving rate of $d\log(\text{O}/\text{H})/dz \sim -0.14$ dex. Our result is in close agreement with the MUFASA simulations, proving the validity of the feedback mechanisms that deposit heavy elements into the surrounding gas described in [Davé et al. \(2016\)](#).

The " M_* -SFR- Z " relation, i.e, FMR, is also apparent at both $z = 0$ and $z = 2$ in the MUFASA simulations, with the prediction that the strength of the SFR dependence does not change with redshift. In Figure 26, we also investigate this three-dimensional relation for HAEs and prove that the FMR shows no sign of evolution at least to $z \sim 2.3$, same as the simulation. The physical explanation for the second-parameter correlations with SFR is that an increase in gas accretion will bring in metal-poor gas that triggers new star formation, and conversely, a shutoff in accretion will result in an evolution more similar to a closed box that will raise the metallicity quickly by consuming its gas.

5.2 Low-mass Starburst HAEs

Through our selection method, we find 306 low-mass starburst HAEs, among which 140 have all detection of H α , [OIII], [OII]. Unlike the main sequence HAEs,

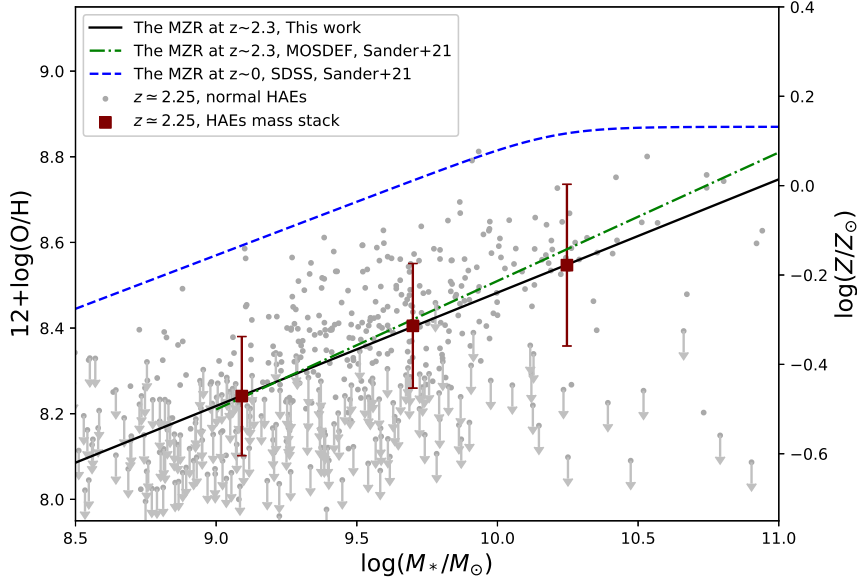


Figure 29. The comparison and evolution of Mass-Metallicity Relation at $z \sim 2.3$ and $z \sim 0$. We select normal HAEs (grey points) in Figure 22 and Figure 24 and stack them into mass bins. Blue dashed line is the best-fit MZR at $z \sim 0$ from Sanders et al. (2021) without correcting for diffuse ionized gas (Sanders et al. 2017). The best-fit MZR at $z \sim 2.3$ from MOSDEF are shown as green dashed-dotted line for reference.

we find that these galaxies scatter above the star formation main sequence with $\Delta MS_{\text{med}} \sim 0.9$ dex. Moreover, they also do not follow the MZR or FMR, when metallicities are calibrating from the O32 index. The median stack of these low-mass starburst HAEs have a close O32 ratio at ~ 0.32 dex independent of the stellar mass. We here discussed some possible reasons for these results.

5.2.1 Limitation of the O32 calibration

As mentioned above, O32 only have a secondary dependence on metallicity and this metallicity-sensitive emission-line ratios may not be applicable to all conditions since the physical conditions of the ISM in low-mass starburst galaxies may differ from their counterparts at low redshift.

For a direct measurement of the gas-phase oxygen abundance, observation of the well-detected emission line $[\text{OIII}]\lambda 4363$ is necessary. The ratio of the flux of the auroral $[\text{OIII}]\lambda 4363$ to that of $[\text{OIII}]\lambda 5007$ is very sensitive to the electron temperature (T_e). The metallicity is then estimated based on T_e . As a result, this measurement is also called the “Direct” or T_e method. (e.g., Pagel et al. 1992; Izotov et al. 2006). However, $[\text{OIII}]\lambda 4363$ cannot be measured from majority of local galaxies, let alone high-redshift galaxies, because it is much weaker than other strong emission lines.

Berg et al. (2012) successfully measured $[\text{OIII}]\lambda 4363$ of 31 local dwarf galaxies with other strong emission lines including $[\text{OIII}]\lambda 5007$ and $[\text{OII}]$. These dwarf galaxies have stellar mass of $6.0 < \log(M_*/M_\odot) < 9.0$ and directly measured metallicity down to $12 + \log(\text{O}/\text{H}) \approx 7.5$. Sanders et al. (2021) supplemented the line ratio of SDSS stacks with these dwarf galaxies and plot the calibrations between emission-

line ratios and direct measured metallicity (see Figure 2 of Sanders et al. 2021). It is interesting that the O32 index of the local dwarf galaxies also have a close value ~ 0.3 dex, and the “O32 vs. $12 + \log(\text{O}/\text{H})$ ” calibration follow a non-linear relation which is different from other linear (or almost linear) empirical calibrations (e.g., Maiolino et al. 2008; Jones et al. 2015; Curti et al. 2017; Bian et al. 2018). It is worth noting that the sample and calibration of Sanders et al. (2021) is mass-dependent while samples from other previous studies are mass-independent, i.e, dwarf galaxies are barely included in the sample. This indicates that, for local dwarf galaxies and main sequence galaxies with similar metallicities, they may have a different O32 index statistically, that the O32 index of dwarf galaxies are ~ 0.7 dex lower than those of main sequence galaxies.

The low-mass starburst HAEs in our sample, have a similar stellar mass with those local dwarf galaxies. Therefore, it is not surprising that the mass-independent O32 ratio is found in our low-mass starburst HAEs because local dwarf galaxies have a similar trend. On the other hand, direct measurement of gas-phase metallicity of local dwarf galaxies (Berg et al. 2012) indicated that the MZR still holds for the low mass regime down to $12 + \log(\text{O}/\text{H}) \approx 7.5$. As a result, it is not likely that the similar O32 ratio corresponds to similar metallicity for our low-mass starburst HAEs. A much more mass-dependent empirical calibration for local dwarf galaxies, such as N2 ($[\text{NII}]\lambda 6584/\text{H}\alpha$, see also in Figure 2 of Sanders et al. 2021), or a direct measurement of metallicity ($[\text{OIII}]\lambda 4363$) is needed to further explore the metallicity of our low-mass starburst HAEs.

One possible physical explanation for the lower O32 index in dwarf galaxies than those of main sequence galaxies with the similar metallicities is that dwarf galaxies may have lower ionization parameters. As mentioned above, O32 emission-line ratio works as a direct diagnostic for ionization parameter, and Equation (30) gives the definition of the ionization parameters in the photoionization code CLOUDY (Ferland et al. 1998, 2013) that gases are described as spherical concentric layers centred on the ionizing sources. Following this rule and the emission-line model from Charlot & Longhetti (2001) with the latest stellar population synthesis, Gutkin et al. (2016) compute a large number grids of emission-line ratios from star-forming galaxies in a wide range of chemical abundances, from $Z_{\text{ISM}} = 0.0001$ to 0.04 ($12 + \log(\text{O}/\text{H}) \approx 6.5$ to 9.1). One of the panels in Figure 2 of Gutkin et al. (2016) plot the evolution of the O32 index with the metallicity predicted by the photoionization models. It is found that, from $12 + \log(\text{O}/\text{H}) \approx 6.5$ to 8.4 (sub-solar metallicity), the O32 index do not evolve much for the photoionization models with ionization parameter $\log U < -2.5$. In figure 30, we compile the “O32 vs. $12 + \log(\text{O}/\text{H})$ ” calibration from previous studies including observations and photoionization models. It is interesting that the calibration of Sanders et al. (2021) at $7.5 < 12 + \log(\text{O}/\text{H}) < 8.2$ has a similar trend to those of photoionization models, while the O32 index decreases sharply from $12 + \log(\text{O}/\text{H}) \sim 8.4$ which is similar to empirical calibrations from other studies. Since Sanders et al. (2021) supplemented dwarf galaxies in the calibration, a reasonable speculation is that these dwarf galaxies hold almost unchangeable ionization parameters during the evolution, along with the increase of metallicities. Then, when they evolve into main sequence galaxies, the ionization parameters start to drop and lead to sudden decrease of O32. On

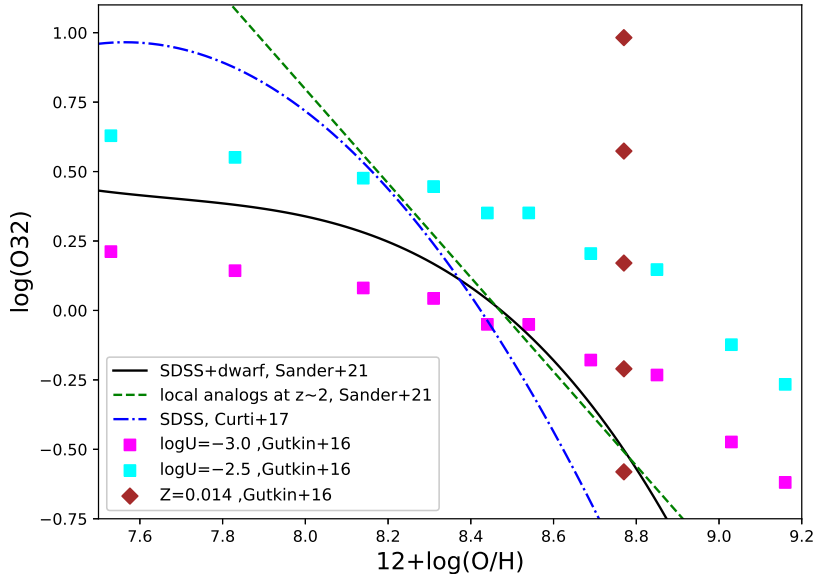


Figure 30. The compilation of the ‘O32 vs. $12 + \log(\text{O}/\text{H})$ ’ calibration from previous studies. Black solid line shows the best-fit $z \sim 0$ calibrations of Sanders et al. (2021), fitted by the combination spectra data from Andrews & Martini (2013) and Berg et al. (2012). Green dashed line and blue dashed-dotted lines display the calibrations of Bian et al. (2018) and Curti et al. (2017), respectively. Squares and diamonds represent the O32 index predicted by the photoionization models from Gutkin et al. (2016). The models assume a fixed hydrogen density, $n_{\text{H}} = 100 \text{ cm}^{-3}$, solar carbon-to-oxygen ratio, and IMF upper mass cut-off at $100 M_{\odot}$ with changeable metallicities and ionization parameters. Squares represent the change of O32 index with metallicities at fixed ionization parameters, while diamonds is the change of O32 index with ionization parameters at fixed metallicity.

the other hand, for those main sequence galaxies with extremely strong starburst, they may hold higher ionization parameters than dwarf galaxies and corresponding higher O32 index.

5.2.2 Inflow of metal-polluted gas ?

The previous section discusses about the issue of the O32 index that it may not be a good metallicity indicator of our low mass starburst HAEs. On the other hand, we cannot exclude the possibility that these low mass HAEs may have a higher metallicity than the MZR as the O32 index has shown. This means that these low mass HAEs may suffer from the inflow of metal-polluted gas, i.e, the pristine gas forming stars already contains a certain amount of metal. From a theoretical point of view, the collective explosive output of from supernovae at earlier epochs could pollute vast regions of intergalactic space to an additional chemical enrichment and some theoretical studies show that massive elliptical galaxies may play an important role in establishing the chemical abundance of the intracluster medium (De Lucia et al. 2004). Since the chemical enrichment is more likely to happen in the clustered environments, we here further explore whether the O32 index has environment dependence. Considering the uncertainty of z_{phot} in our catalog and the number of low mass starburst HAEs in each redshift bin (see Figure

11), we divided galaxies into two redshift intervals, $2.05 < z < 2.3$ and $2.3 < z < 2.5$. To quantify the environmental factors of galaxies, we measure the angular distance from each object to the seventh nearest neighbor, d_7 , and then computed the corresponding surface density, $\Sigma_7 \propto (d_7)^{-2}$ (Papovich et al. 2010). Figure 31 gives the relation between the O32 index and corresponding surface density, $(d_7)^{-2}$, of all 140 low-mass starburst HAEs. We find that there is no relation between the O32 index and $\Sigma_7 \propto (d_7)^{-2}$, indicates no dependence of environment for our sample. As a result, we cannot draw a conclusion that whether the inflows of metal-polluted gases have contribution on the measurement of the O32 index or not.

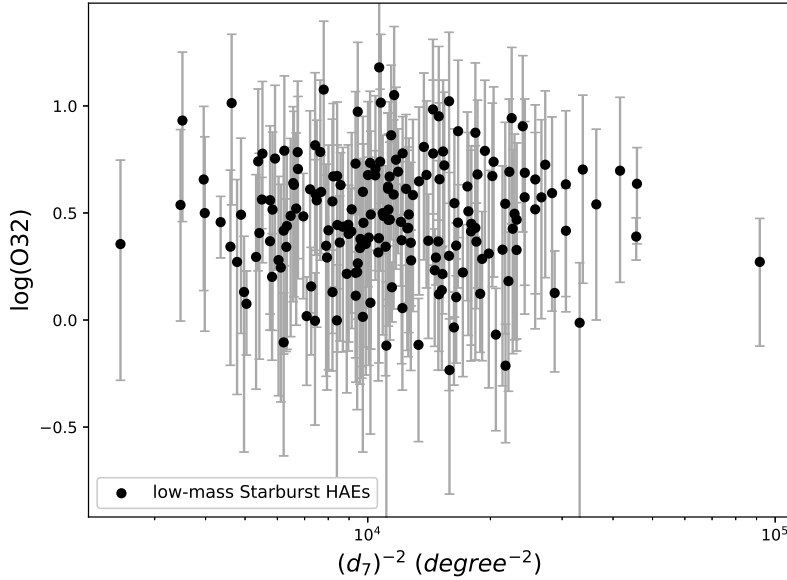


Figure 31. The relation between the O32 index and surface density of low-mass starburst HAEs in two redshift intervals, $2.05 < z < 2.3$ and $2.3 < z < 2.5$. The error bars of each measurement of the O32 index are added.

5.2.3 Similarity and Difference with LAEs

As shown in Figure 22, the low-mass starburst HAEs in our sample scatter above the $H\alpha$ -based star formation main sequence. Similar trends are also found in Ly α emitting galaxies (LAEs) at $z \sim 2 - 3$, which also lie above the main-sequence line based on their $H\alpha$ -based SFR (Nakajima & Ouchi 2014) or UV-based SFR (Hagen et al. 2016). On the other hand, at $z \sim 2.5$, some other LAEs with UV-based SFR follow the extrapolated line of the SFMS to the lower mass end (Shimakawa et al. 2017). In Figure 32, we plot the UV-based SFMS of our low-mass and main sequence HAEs, and the LAEs from previous studies. Quantitatively, the 306 low-mass starburst HAEs in our sample scatter above the SFMS of Speagle et al. (2014) with $\Delta MS_{\text{med,UV}} = 0.73$ dex, while the low-mass LAEs of Hagen et al. (2016) have $\Delta MS_{\text{med,UV}} = 0.31$ dex and the low-mass LAEs of Shimakawa et al. (2017) have $\Delta MS_{\text{med,UV}} = -0.15$ dex. Moreover, we also include the $H\alpha$ -based SFR of LAEs of Nakajima & Ouchi (2014) in this figure, scatter above the SFMS with $\Delta MS_{\text{med,H}\alpha} = 0.45$ dex. While, SFR($H\alpha$) of our low-mass HAEs scattering

above the SFMS of Speagle et al. (2014) with $\Delta MS_{\text{med}, \text{H}\alpha} = 0.89$ dex. This finding demonstrates that our low-mass starburst galaxies tend to have even stronger star formation activities than the LAEs at similar redshift.

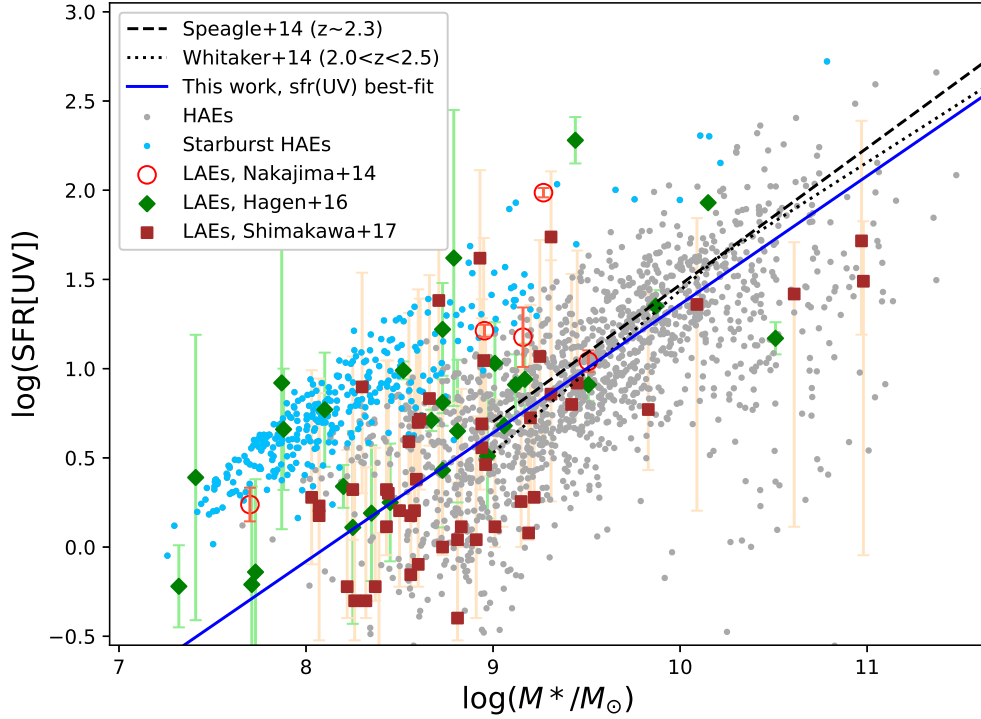


Figure 32. The UV-based star formation main sequence of HAEs at $z_{\text{med}} = 2.25$ in the ZFOURGE field. Individual blue points are starburst objects with $\Delta MS > 0.6$ dex in the $\text{H}\alpha$ -based SFMS. Blue solid line is the best-fit UV-SFMS of the individual HAEs with $9.2 < \log(M_*/M_\odot) < 10.2$. The best-fit SFMS from Whitaker et al. (2014) and Speagle et al. (2014) are also included for reference. Furthermore, LAEs from Nakajima & Ouchi (2014), Hagen et al. (2016) and Shimakawa et al. (2017) are represented as red circles, green diamonds and brown squares, respectively.

Besides, Figure 28 shows that the estimated ionization parameters ($q_{\text{ion}} \sim 7.9$) of our starburst HAEs are ~ 0.5 dex lower than those of LAEs, mainly because O32 is smaller for our starburst HAEs. Also, Nakajima & Ouchi (2014) suggested that there is a positive correlation between the O32 index and Ly α photon escape fractions (f_{esc}) based on the photoionization models with different q_{ion} from 7.5 to 8.5 (see Figure 11 of Nakajima & Ouchi 2014). From the prediction of that photoionization models, our starburst HAEs tend to have $f_{\text{esc}} \simeq 0$, in comparison to LAEs with $f_{\text{esc}} \simeq 0.2$. Combining these factors, it is reasonable to speculate that our low-mass starburst HAEs have much a lower f_{esc} than those of LAEs, and the unescaped ionizing photons may trigger a higher $\text{H}\alpha$ luminosity than the LAEs.

5.3 Further observations

As explained above, chemical abundances in HII region are still subject to systematic uncertainties. In the vast majority of cases, due to the difficulty of detect-

ing the faint T_e sensitive [OIII] λ 4363, chemical abundances are derived from strong emission-line ratio calibration. The current work is limited to the O32 and R₂₃ indices, both of which have defects in calibrating gas-phase metallicity. As a result, measurements of [NII] on these low-mass starburst galaxies would be a great replenishment for our study.

Luckily, SWIMS will carry on a spectroscopic observation of these low-mass starburst galaxies in the ZFOURGE-COSMOS field during the S22A on Subaru telescope. Two masks covering ~ 10 of them would be observed with an exposure time ~ 4 hours per mask to detect all the major optical emission lines, from [OII] to [SII] λ 6717, 31.

Besides, current medium K-band image data of SWIMS is not deep enough, among which the longest exposure time is 2 hours, while ZFOURGE MBF images have exposure time longer than 10 hrs. Perfecting the medium K-band detection needs much longer exposed images from SWIMS. It has been calculated that if the depth of imaging is depth(5σ) ~ 25.0 AB magnitude in three medium K-band filters, which is close to ZFOURGE MBF image, it will enable us to reach a 2σ detection limit of SFR(H α) $\sim 2 M_\odot \text{yr}^{-1}$. This will help us to extract fainter HAEs and extend the SFMS and MZR to a lower mass regime. Beyond that, the SFMS and MZR extend unabated to even much lower masses can further be observed by the James Webb Space Telescope (JWST), opening the door to stellar mass and chemical evolution in the earliest stage of galaxy formation.

6 SUMMARY AND CONCLUSIONS

In this study, we have carried out a systematic search for HAEs at $z \sim 2.3$ in three ZFOURGE fields. The selection of HAEs is based on the flux excess in ZFOURGE- K_s filters due to the intense $H\alpha$ emission lines relative to the best-fit stellar continuum from SED fitting with emission line templates. Following the same strategy of extracting $H\alpha$ emission lines, we also extract the [OII] and [OIII] emission lines of these HAEs from the ZFOURGE medium J/H-band filters. This enables us to carry out multiple emission-line studies on the HAEs and investigate further physical properties. Our analysis separates the HAEs into two populations, the main sequence HAEs and the low-mass starburst galaxies. The main results can be summarized as follows:

1. We have identified 1780 $H\alpha$ emitters at $2.05 < z < 2.5$ with $> 2\sigma$ flux excesses relative to the stellar continuum. Among them, 762 HAEs have detection of [OII] and [OIII] with $> 1\sigma$ flux excesses. In consideration of the limiting volume of the ZFOURGE survey ($\Delta V = 6.8 \times 10^5 \text{ Mpc}^3$), this selection method is very efficient in identifying emitters.
2. The $H\alpha$ emission line fluxes derived by our method have a very good consistency with the spectroscopic line fluxes from the MOSDEF survey, that more than 90% of the detected fluxes have consistent values within a factor of 3. Moreover, an SED-fitting simulation of mocked galaxies with input emission line fluxes has been carried out. Most output line fluxes have a difference within 10%, indicating a good stability of the SED fitting method.
3. The $H\alpha$ luminosity function shows a discrepancy in the bright end when compared to the result of Sobral et al. (2013) and Terao (2020). The discrepancy can be partly explained by the different dust correction applied in these studies. Further, the CSFRD is consistent with literature based on $H\alpha$ measurements, but show an excess in comparison with UV or IR measurements. We think that the limiting volume of the ZFOURGE survey may have some biases and applying our method to a catalog with larger volume is possible to solve this issue.
4. The best-fit $H\alpha$ -derived and UV-derived SFMS of our sample have a good consistency with previous studies above the stellar mass completeness with a slope of 0.70 ± 0.03 for SFMS($H\alpha$) and 0.72 ± 0.04 for SFMS(UV). Meanwhile, we extract a large number of low-mass HAEs scattering above the SFMS, also found by Terao (2020). This suggests that these low-mass HAEs are in bursty star formation phases. As a result, we separate all of our HAEs into the main sequence HAEs and the low-mass starburst HAEs.
5. We obtain the oxygen abundance (metallicity) by the empirical calibration of the O32 index. It is found that the main sequence galaxies follow the Mass-Metallicity Relation (MZR) and the Fundamental Metallicity Relation (FMR). The power law slope of the MZR does not evolve out to $z \sim 2.3$ with a value of ≈ 0.25 . At fixed M_* , metallicity decreases with increasing redshift

as $d\log(\text{O}/\text{H})/dz \sim -0.11$ dex. This evolving rate is consistent with modern cosmological hydrodynamic simulations. We also find that the FMR shows no sign of evolution at least to $z \sim 2.3$, same as the simulation.

6. On the other hand, the low-mass starburst HAEs have the O32 index ~ 0.32 dex independent of stellar mass. It seems that neither the MZR nor the FMR is applicable to these HAEs. While, we think this results from the calibration limitation of the O32 index since similar trend also happens on local dwarf galaxies. A further observation of more mass-dependent emission-line ratio is needed to confirm whether these low-mass starburst galaxies follow the MZR or not.

7. We apply the photoionization models of [Kewley & Dopita \(2002\)](#), which use the combination of R_{23} and O32 indices, to determine the ionization parameters of galaxies. We find a lower ionization parameters in our low-mass starburst HAEs than typical LAEs, but a similar ionization parameters to LBGs. When compared with the UV-based SFR, it is found that the low-mass starburst HAEs have a more intense star formation activity than LAEs. We speculate that our low-mass starburst HAEs are not an analogous population of LAEs that these low-mass starburst galaxies may have very low $\text{Ly}\alpha$ photon escape fractions.

Acknowledgement

I would first like to express the deepest gratitude to my supervisor, Dr. Kentaro Motohara for the insightful and instructive comments, remarks and engagement through the learning process of this master thesis. The door to his office was always open whenever I ran into a trouble spot or had a question about my research or writing. He consistently allowed this thesis to be my own work, but steered me in the right direction. Besides, he has given me patient and constant support and taught me how to become a qualified researcher during my Master course.

I would also like to thank Dr. Lee Spitler from Macquarie University who was involved in the ZFOURGE survey. Through the collaboration with him, he provided me a lot of advises on scientific research. He was also the second reader of this thesis, and I am gratefully indebted to his for very valuable comments on this thesis. Without his participation and input, this study could not have been successfully conducted.

I would also like to acknowledge Dr. Masahiro Konishi from the SWIMS team, who supported me a lot on the computer programming during the imaging processing. In virtue of his great reduction pipeline, I am able to reduce SWIMS images smoothly and perfectly.

I would like to express my special thanks to several experts in extragalactic astronomy, Dr. Tadayuki Kodama, Dr. Kenichi Tadaki, Dr. Rhythm Shimakawa and Dr. Kimihiko Nakajima. They gave me many advises on this study and provided me with the related catalogs.

During my Master course, I have experienced pleasure time with all of the stuffs and student members of the SWIMS team, namely, Dr. Hidenori Takahashi, Dr. Shuhei Koyama, Natsuko Kato, Dr. Yasunori Terao, Kosuke Kushibiki, Hiroki Nakamura, Shogo Homan. They have made these two years an invaluable period in my life.

Finally, I must express my very profound gratitude to my parents for providing me with unfailing support and continuous encouragement throughout my years of study and through the process of researching and writing this thesis. This accomplishment would not have been possible without them.

Appendices

A SWIMS imaging pipeline: SWSRED

As introduced in section 2.2.1, the SWIMS data are reduced using a custom Python pipeline, named “SWSRED”, written by M. Konishi. The latest flow chart of the reduction pipeline is shown in Figure A.1 from [SWIMS webpage](http://www.ioa.s.u-tokyo.ac.jp/TAO/swims/?Data_Reduction/Imaging_Data_Reduction). Notably, the sketch for SWSRED mentioned in section 2.2.1 ended before the second to last step, where the final images had already been reduced. SWSRED has no documentations yet, but almost all the options and parameters setting could be done in the “swsred/reduce_all.py” file. We here follow this flow chart to introduce important steps in one iteration of the image reduction.

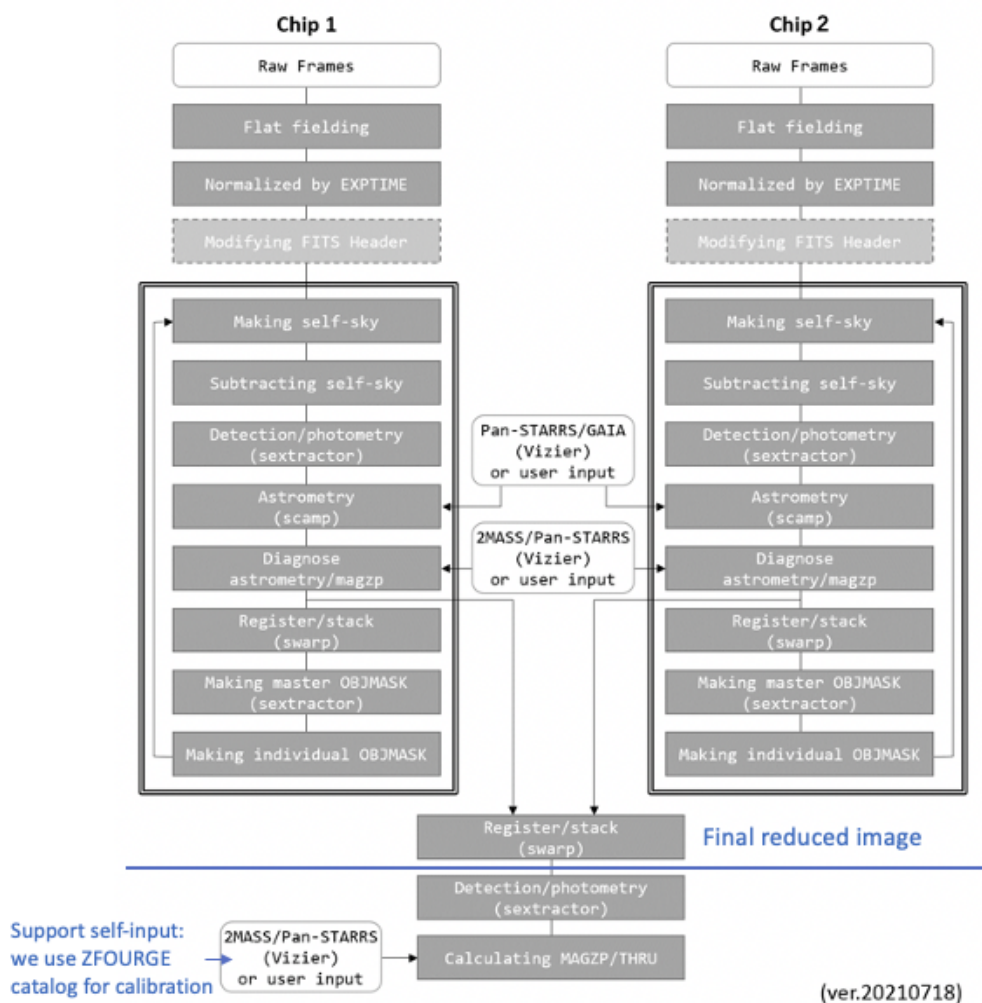


Figure A.1. The flow chart of SWSRED from http://www.ioa.s.u-tokyo.ac.jp/TAO/swims/?Data_Reduction/Imaging_Data_Reduction.

Flat fielding: Dome flat frames are used for flat field. In each semester of SWIMS observations, dome flat frames of both chips in each filter would be created by IRAF, available from the same website as the flow chart. The pipeline would

automatically read the semester from the raw images and choose the appropriate dome flat frame.

Making self-sky: The sky background is computed by averaging a user-defined number of images taken before and after a certain exposure except the frame on the same dithering position. The number of frames used to create a self sky frame is defined by `n_sky` in `reduce_all.py`. Also the combine type and other detailed setting can be adjusted in `make_sky.py`.

Detection/Photometry: The detection threshold for sources used for astrometry is defined by `detect_thresh_wcs` in `reduce_all.py`. The default setting is 3.0. While in some cases, for example, the number of bright stars is very rare in the field, or the seeing is not good enough, this value have to be set to a lower value. Otherwise, if the number of detected objects is very small, errors would happen during the astrometry.

Astrometry: The brightest (faintest) source selected for astrometry is defined by `mag_min_wcs` (`mag_max_wcs`) in `reduce_all.py`. The default setting of `mag_max_wcs` is 18.5. While, same as above, for the sky-field with very little bright stars, we may relax this setting to larger value (recommended value: 20). The reference catalog for astrometry can be selected from Pan-STARRS1 (Chambers et al. 2016), GAIA-DR2 (Gaia Collaboration et al. 2018) and 2MASS (Skrutskie et al. 2006). Notably. the pipeline encounters most of the errors during this process and the reduction pipeline would stop here.

Register/stack: After the correction of astrometry, all the frames in the set are registered and SWARP is ran to stack these frames together into one stacked frame. The default `COMBINE_TYPE` is `CLIPPED`. This option is not introduced in the User’s guide of SWARP (Bertin 2010b). In short, this `COMBINE_TYPE` exclude pixel values that off from the mean by a value greater then a factor times of the standard deviation (Gruen et al. 2014). While, we can still choose other options which are listed in the User’s guide of SWARP.

Making master/individual OBJMASK: In the last part of the iteration, object masks are created for each frame in order to obtain a better self-sky in the next iteration.

B PSF matching on SWIMS reduced image

In order to merge our SWIMS sources into ZFOURGE catalog, we follow the PSF matching method of ZFOURGE. After reprojecting K_1/K_2 image to match the ZFOURGE pixel sizes, we firstly select unsaturated stars with high S/N in the reprojected image and cut them out into postage stamps of $10''.65 \times 10''.65$. We closely follow the step in Straatman et al. (2016) and select a tightly homogeneous sample of stars to obtain the final-median PSF. Figure B.1 exhibits the final-median PSF we obtained from SWIMS K_1/K_2 image.

All the individual PSFs from the ZFOURGE survey have been convolved into a target PSF same as the Moffat profile (Moffat 1969) with $\text{FWHM} = 0''.9$ and $\beta = 2.5$ with the advantage of the noiseless feature of theoretical models. Then, a convolution kernel was generated for each PSF during this process. Finally, the original images were then convolved with respective kernels and to match the target Moffat PSF. As

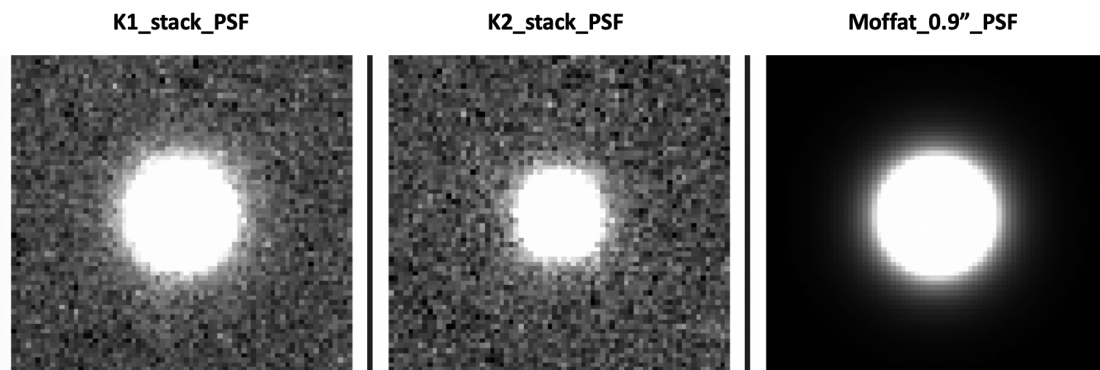


Figure B.1. The final-median PSF of SWIMS K_1/K_2 image obtained from tightly homogeneous stars. The target Moffat profile with FWHM = $0''.9$ and $\beta = -2.5$ is also presented here.

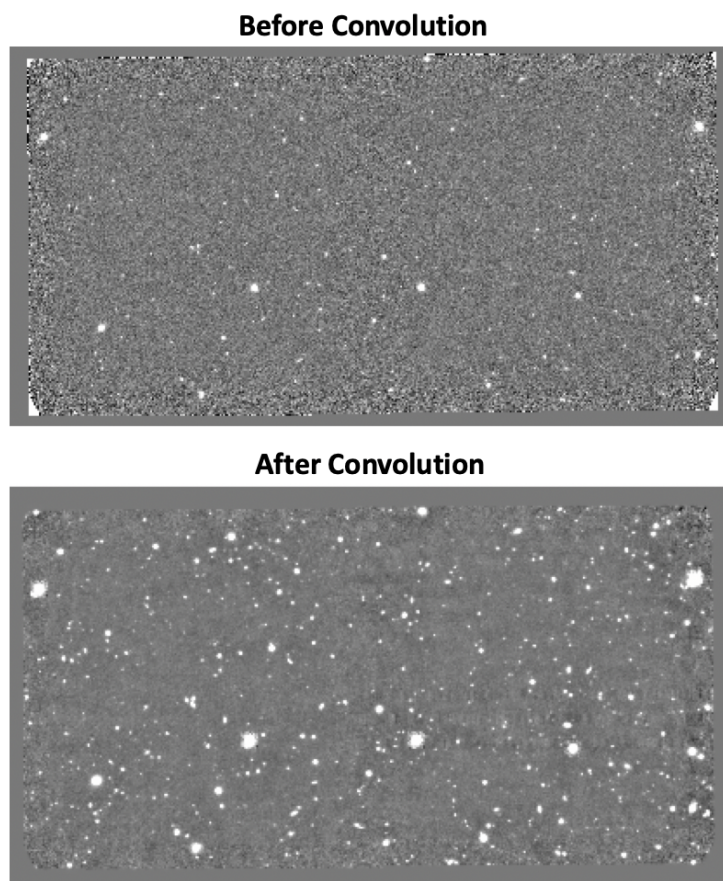


Figure B.2. The SWIMS K_2 image before and after convolution following the process introduced in Appendix B.

a result, we also need to the same process for our SWIMS K_1/K_2 image. In order to attain this goal, we obtain the convolution kernel of each K_1/K_2 image by an open-source Python code, PyPHER (Boucaud et al. 2016). Finally, the reprojected K_1/K_2 image are convolved with the kernel from PyPHER. Although the convolved PSF shows some residual compared to the model, we calculated that the convolved PSF capture the same amount of light within 1% at $r = 0''.6$, indicating a good convolved result. Figure B.2 gives the the convolved K_2 images.

C Comparison of different SED fitting code

Besides CIGALE, We have also tried SED fitting with another two code, FAST++ (Kriek et al. 2009) and PROSPECTOR (Johnson et al. 2021) in our work.

FAST++ is a C++ version of the popular SED fitting code FAST, with a number of small differences between FAST++ and the original FAST. Two simple stellar population models (SSP), BC03 and M2005, with grids of parametric SFH (exponential, delayed or truncated) are compiled in the FAST libraries directory. Then FAST++ reads the parameter file, and makes a cube of model fluxes for the full stellar population grid. It is worth mentioning that the original stellar population synthesis from FAST libraries do not contain emission lines, so we personally run the IDL to add the nebular emission lines following Inoue (2011) into each model. The strength of emission lines is fixed, which is defined by the number of ionizing photons (`n_lyc`) in the IDL script. In short, though the SED fitting process of FAST++ is similar to CIGALE, FAST++ is a bit old-fashioned and the treatment of emission lines, dust attenuation is cruder than that of CIGALE.

PROSPECTOR is a python-based SED fitting code with several modern features. For stellar population synthesis, the Flexible Stellar Population Synthesis (FSPS; Conroy et al. 2009; Conroy & Gunn 2010) package is used. The FSPS includes detailed stellar populations with a variety of choices for stellar isochrones, stellar spectral and dust emission libraries. PROSPECTOR code can also model and fit more flexible or complicated SFHs, so-called “non-parametric” SFHs. Galaxies evolve through piece-wise constant star formation histories, in each of N bins with a user-defined lookback time. Non-parametric SFHs are capable of modeling star formation histories with sharp features or unusual shapes which are forbidden by the parametric forms (e.g., Cohn et al. 2018; Kubo et al. 2021). Lastly, traditional codes often worked by comparing pre-computed parameter grids or libraries of SED models and find the closest models to the observations (χ^2 fitting). On the other hand, FSPS and non-parametric SFHs are very flexible and have too many degenerate parameters, leading to poor and noisy best-fit solutions through the traditional routine. So, PROSPECTOR carries out Bayesian statistics, coupled with a Monte Carlo Markov chain (MCMC) sample to fully explore the posterior probability for poorly constrained parameters. However, this fitting process leads to a problem that each PROSPECTOR run only work on one single galaxy. Meanwhile, each PROSPECTOR run cost around half an hour during our test. As a result, it would be too time-consuming for PROSPECTOR to finish fitting almost 5000 galaxies from the parent sample.

In consideration of these factors, we decide to present the SED fitting results

from CIGALE in the main text eclectically. In section 4.1, we found that the bright end of the $H\alpha$ luminosity function from CIGALE is deficient compared with Terao (2020), which use a similar method as us but a different SED code, FAST. Except the difference on dust correction, we speculate that the observed luminosity may also have some bias. So, we run the FAST++ code on the parent sample and applying the same procedure to extract the $H\alpha$ line fluxes. The comparison between the observed $H\alpha$ luminosity from CIGALE and FAST++ are shown in Figure C.1. Based on the linear regression result, we find that at the bright-luminosity end, FAST++ tends to produce brighter $H\alpha$ luminosity.

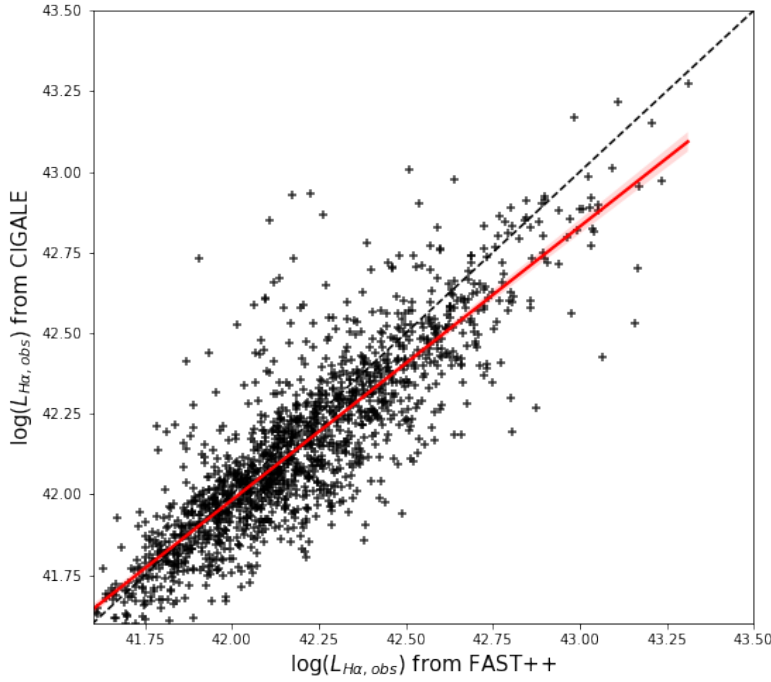


Figure C.1. Relation between the observed $H\alpha$ luminosity from CIGALE and FAST++. Red solid line is the linear relationship as determined through regression, with a shaded region represents the 95% confidence interval for that regression.

Since the observed $H\alpha$ luminosities are determined from the flux excess in the observed K_s fluxes which are independent of the SED code, the result from Figure C.1 means that the stellar continuums derived by FAST++ are lower than those from CIGALE. In order to investigate whose stellar continuums are more reliable, we also run the PROSPECTOR code on several objects for reference. Besides, we also include the best-fit SED from Terao (2020) produced by FAST. The comparison between the best fit models from these codes for the same galaxy are presented in Figure C.2. We find that, the best-fitting stellar continuums from CIGALE and PROSPECTOR are very close to each other, while quite different that from FAST++ (FAST). We can find that the FAST++ (FAST) fitting results do not show the obvious Balmer and D4000Å Jump, leads to a lower stellar continuum flux at redder wavelength. This phenomenon may result from an overestimate of emission line strengths added to the stellar continuum templates. Since CIGALE

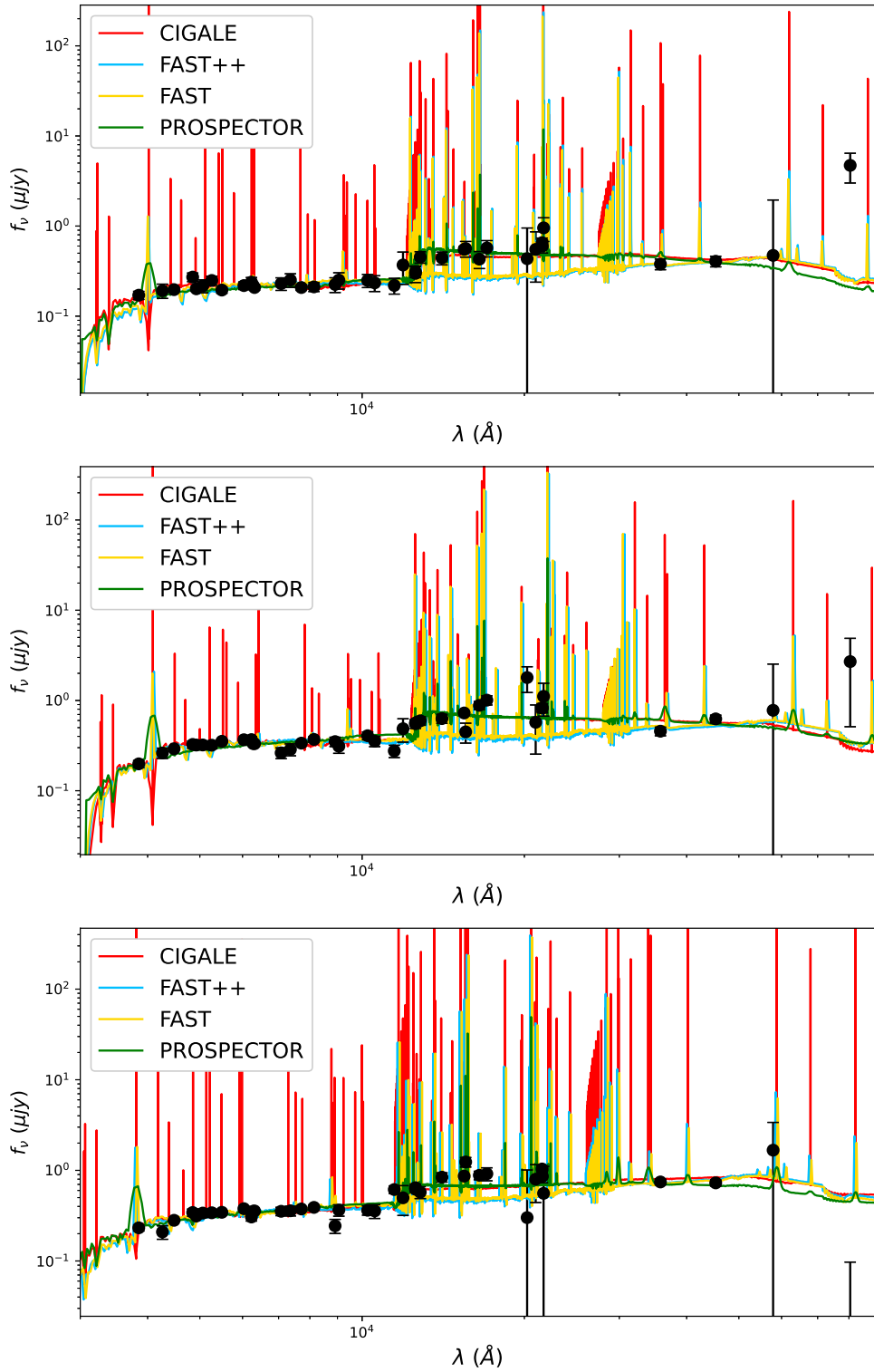


Figure C.2. The best-fit SED fitting model from CIGALE, FAST++, FAST, PROSPECTOR for three individual galaxies, shown as red, blue, yellow and green line, respectively. Notably, the treatment of emission line templates is different in CIGALE, FAST++(FAST) and PROSPECTOR, so the apparent feature is diverse from each other.

and PROSPECTOR are more modern and have more delicate treatments of emission lines, we prefer the SED-fitting result from these two codes.

In conclusion, we find that FAST are likely to produce a lower stellar continuum than CIGALE and may lead to an overestimate of $H\alpha$ fluxes. This is an important factor that causes an excess at the bright end of $H\alpha$ luminosity function.

D SED fitting simulation of individual model

In section 3.5.1, we present an individual galaxy SED simulation, which shows a bimodal distribution of output $H\alpha$ fluxes, because of the degeneracy to different galaxy types during the fitting. Such case in the main text is infrequent among all the simulated galaxy SEDs. Here we presented some general examples of individual galaxy SED simulation in Figure D.1 and D.2.

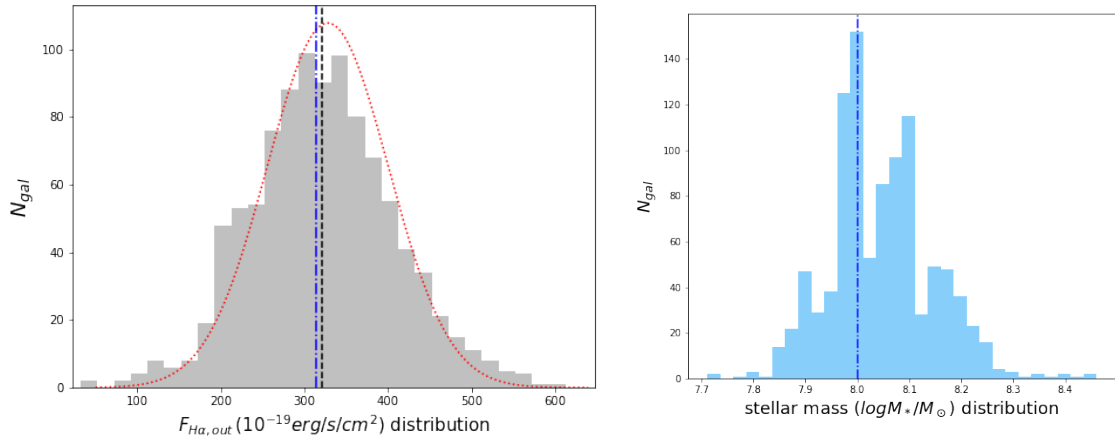


Figure D.1. The simulation and output result from a galaxy SED with $\log(M_*/M_\odot) = 8.0$ (ID: 5961). Outlines as the top two panels in Figure 13.

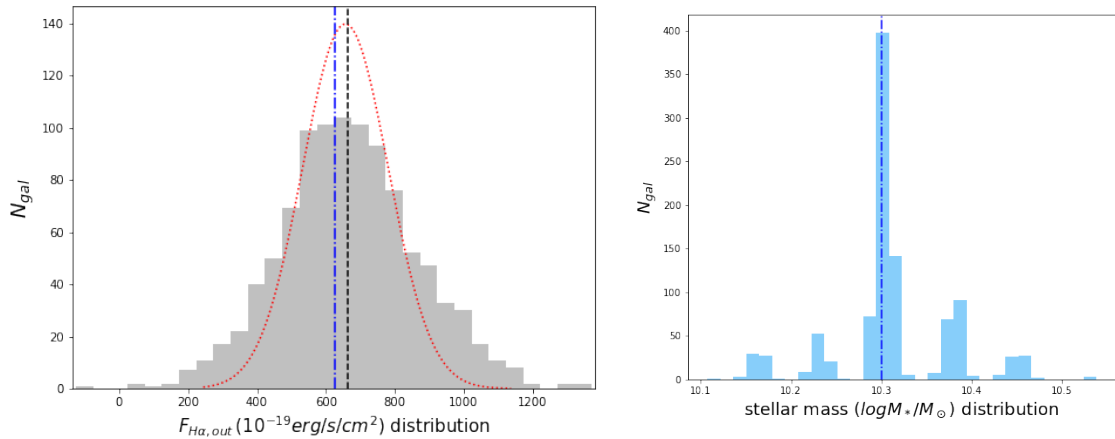


Figure D.2. The simulation and output result from a galaxy SED with $\log(M_*/M_\odot) = 10.3$ (ID: 3731). Outlines as the top two panels in Figure 13.

One example is a low-mass galaxy SED with $\log(M_*/M_\odot) = 8.0$, while another is a high-mass galaxy SED with $\log(M_*/M_\odot) = 10.3$. As was shown in Figure 16,

we find that high-mass galaxies often have much broader distribution of output $H\alpha$ fluxes than low-mass galaxies, i.e, higher possibility of degeneracy to other templates instead of the template for the best-fit model. These two examples also reflect this feature when comparing the distribution of output $H\alpha$ fluxes to the randomized $H\alpha$ fluxes recovered from the Gaussian noise on K_s fluxes. It is easily found that the high-mass one has a broader distribution of output $H\alpha$ fluxes. When examining the stellar mass distribution, we find a multi-modal distribution of stellar mass on the high-mass galaxy SED, indicating the degeneracy to other galaxy types.

E Reddening comparison of various dust attenuation recipes

In our study, we apply a special dust correction recipe for the color excess of nebular emission, $E(B - V)_{neb}$, that amplifying the color excess of stellar continuum, $E(B - V)_{star}$, by a f -factor of $1/(0.44 + 0.2z)$ (Saito et al. 2020) instead of traditional treatment that use a fixed $1/0.44$. Besides, we introduced the diversity of dust attenuation models in CIGALE in section 3.2.3. Therefore, we also run the CIGALE fitting with another two dust attenuation recipes based on the `dustatt_modified_starburst` model introduced in section 3.2.3. This model enable us to fit stellar continuum and nebular emission with respective extinction curves, connected by a fixed f -factor.

For the first recipe, the Calzetti curve ($R_V = 4.05$; Calzetti et al. 2000) is used to fit the stellar continuum, meanwhile the Milky Way curve ($R_V = 3.1$; Cardelli et al. 1989) is used to fit for nebular emission lines with a user-defined f -factor of 0.44. Actually, this recipe is popular used for nearby galaxies.

On the other hand, for the second recipe, we adopt the conclusions from Reddy et al. (2015, 2020) based on the MOSDEF observation, using the SMC curve ($R_V = 2.76$; Gordon et al. 2003) to fit the stellar continuum, and the Milky Way curve ($R_V = 3.1$; Cardelli et al. 1989) with a user-defined f -factor of 0.48 to fit the stellar continuum. This $f = 0.48$ is the best-fit relation between $E(B - V)_{star}$ in Reddy et al. (2015) and $E(B - V)_{neb}$ obtained from the Balmer decrement and assuming an intrinsic ratio of $H\alpha/H\beta = 2.86$ in Reddy et al. (2020).

In this section, we try to compare these reddening correction method and see whether a change of dust attenuation recipe will lead to some systematic offsets. Moreover, we further compare the SED-derived $E(B - V)_{neb}$ and Balmer decrement derived $E(B - V)_{neb}$ to check whether there would be any influence on derived galaxy properties.

Firstly, we make a comparison between the observed emission line fluxes derived from SED fitting and those from the MOSDEF Emission-Line Catalog for the cross-matching HAEs as we have done in section 3.5.2, and check whether different dust attenuation recipes would lead to large offsets on the observed emission line fluxes. Figure E.1, E.2 and E.3 give the comparison of observed $H\alpha$, [OIII], [OII] flux, respectively. In each figure, the left panel represents the result from the first dust attenuation recipe mentioned above, while the right panel represents that from the second dust attenuation recipe. At least, we find no significant systematic errors in each panel and still the SED-derived observed fluxes have very good agreement with those from spectroscopic survey that $\sim 90\%$ detected fluxes have consistent

values within a factor of 3. Comparing with the dust attenuation recipe we used in the main text, the nebular emission lines in both new recipes would have stronger dust attenuation than the stellar continuum during the fitting since the f -factor is smaller. However, because the nebular emission would not contribute a lot to the total model fluxes during the SED fitting process for brighter galaxies, we state that the change of dust attenuation recipes would not lead to a large variation on the stellar continuum level and the observed flux of emission lines for the cross-matching HAEs.

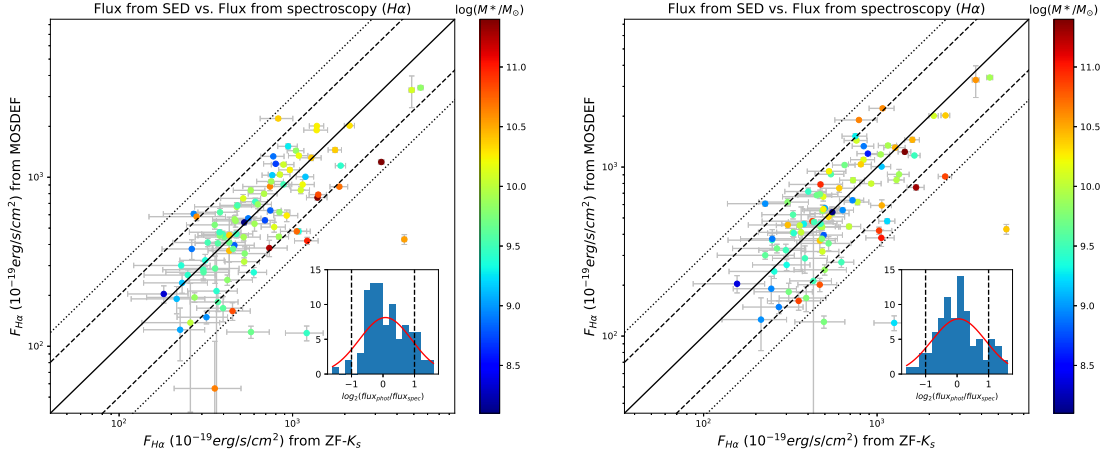


Figure E.1. Left: Comparison between the observed $H\alpha$ fluxes derived from SED fitting with the Calzetti curve and those from the MOSDEF Emission-Line Catalog (Kriek et al. 2015). Right: Same but for the SMC curve. Outlines as in Figure 18.

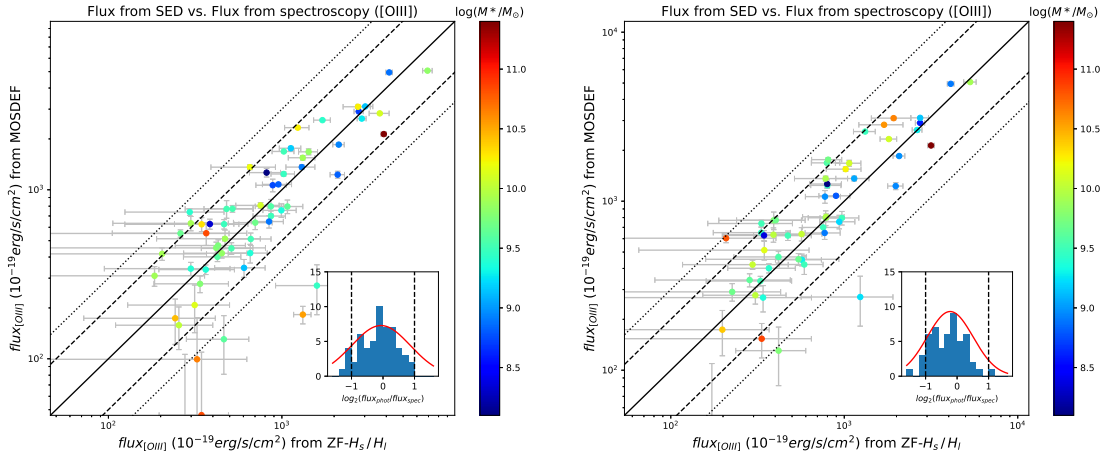


Figure E.2. Left: Comparison between the observed $[OIII]$ fluxes derived from SED fitting with the Calzetti curve and those from the MOSDEF Emission-Line Catalog. Right: Same but for the SMC curve. Outlines as in Figure 18.

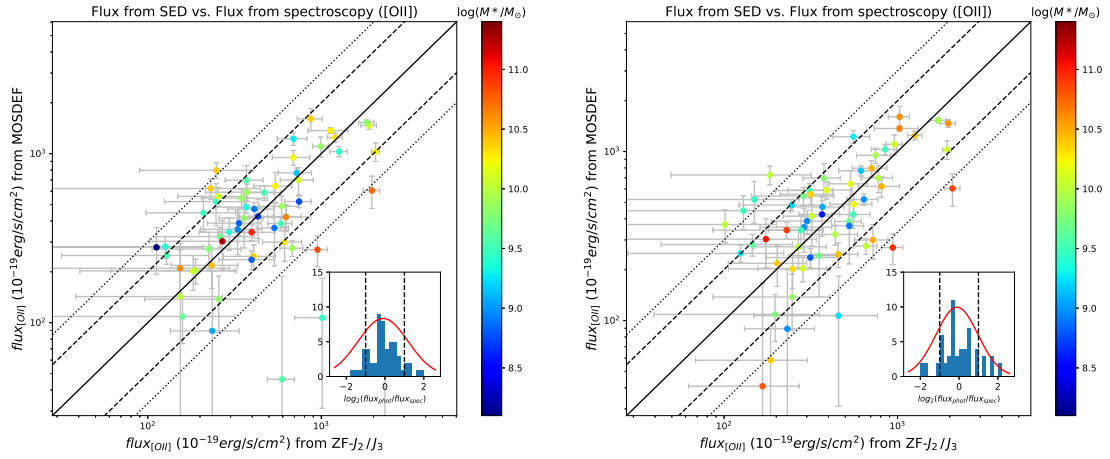


Figure E.3. Left: Comparison between the observed [OII] fluxes derived from SED fitting with the Calzetti curve and those from the MOSDEF Emission-Line Catalog. Right: Same but for the SMC curve. Outlines as in Figure 18.

Next, from each set of the two new SED fitting results, we obtain a new set of observed $H\alpha$ fluxes, dust extinction coefficient $A_{H\alpha}$ and stellar mass M_* . We again plot the star formation rate (SFR) versus stellar mass (M_*) relation and derive the $H\alpha$ -based SFMS as in Figure 22. Figure E.4 represents the SFMS derived from SED fitting with the first dust attenuation recipe, and Figure E.5 is that of the second recipe. Notably, We here still classify starburst galaxies as scattered 0.6 dex above the extrapolated best-fit SFMS of the HAEs with stellar mass $9.2 < \log(M_*/M_\odot) < 10.2$ (the solid blue line in each figure). Also, the best-fit SFMS from Speagle et al. (2014), Whitaker et al. (2014) and Shivaiei et al. (2015) are added for references.

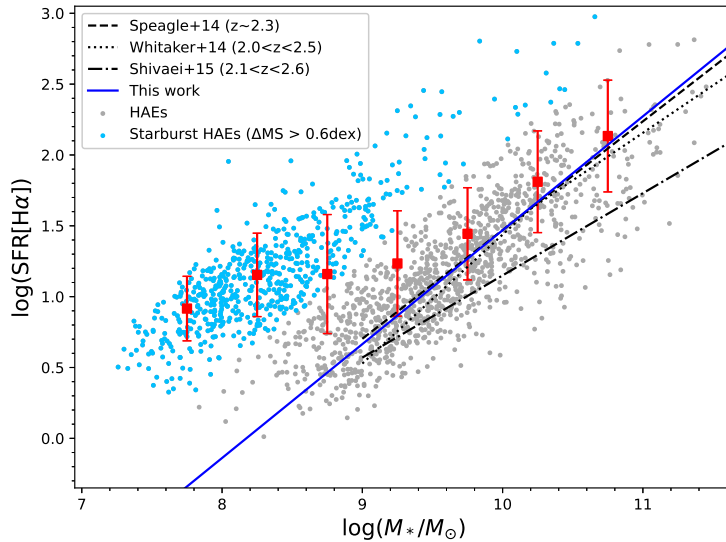


Figure E.4. The star formation main sequence of HAEs in the ZFOURGE field from the SED fitting with the Calzetti curve. Outlines as in Figure 22.

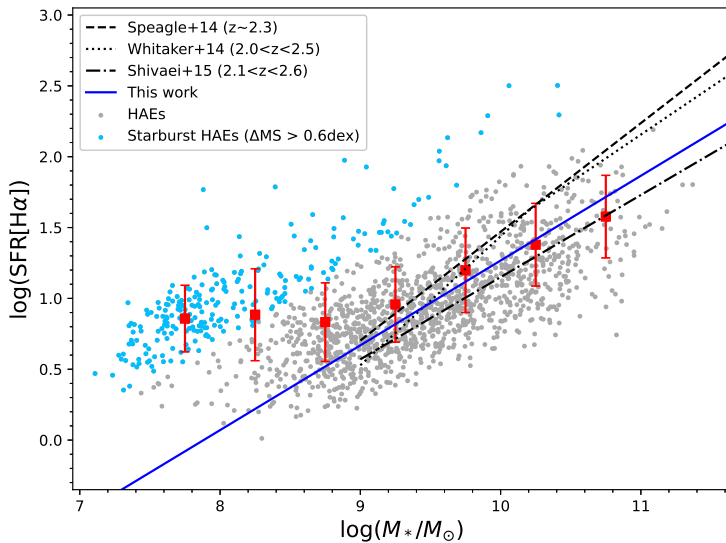


Figure E.5. The star formation main sequence of HAEs in the ZFOURGE field from the SED fitting with the SMC curve. Outlines as in Figure 22.

Here, HAEs of the new fitting results are still selected with flux excesses $> 2\sigma$, and it is found that using different dust attenuation recipe would result in an obvious systematic offsets.

Based on the Calzetti+MW dust attenuation recipe, a total number of 1810 HAEs are selected. The best-fit SFMS have a slope of 0.81 ± 0.03 and intercept of -6.57 ± 0.30 , which is steeper than previous literature. Among all these HAEs, 610 objects are classified as starburst HAEs, which have $\Delta MS > 0.6$ dex and a further cut gives a number of 543 HAEs have stellar mass $\log(M_*/M_\odot) < 9.0$. The number of starburst HAEs is much larger than that in the main text.

In contrast, only 1619 HAEs are selected based on the SMC+MW dust attenuation recipe. The best-fit SFMS have a slope of 0.60 ± 0.03 and intercept of -4.71 ± 0.31 , which is more closer to Shivaie et al. (2015). In this fitting result, a large number of starburst HAEs are lost when comparing with the first recipe. Among all these HAEs, only 240 objects are classified as starburst HAEs, which have $\Delta MS > 0.6$ dex and a further cut gives a number of 213 HAEs have stellar mass $\log(M_*/M_\odot) < 9.0$. The number of starburst HAEs is less than that in the main text.

Since the observed $H\alpha$ fluxes do not have a large variation, the systematic offsets on the SFMS are mainly caused by the large disparity on the dust extinction coefficient $A_{H\alpha}$ derived from the SED fitting. For the first recipe, which assuming the Calzetti curve and dividing the $E(B - V)_{star}$ by a f -factor 0.44, it has been shown in previous studies that this recipe overestimated the corrected $H\alpha$ SFRs for galaxies at $z \sim 2 - 3$ (e.g., Reddy et al. 2010; Steidel et al. 2014), which also happens on our SED fitting test. Therefore, we state that the assumption of $f = 0.44$ seems too small for high-redshift galaxies, leads to an overestimate of dust attenuation for the nebular emission. That's the reason why we adopt a larger redshift-dependent f -factor from Saito et al. (2020) in the main text.

On the other hand, [Shivaei et al. \(2020\)](#) derived the dust attenuation curve of low-metallicity galaxies and high-metallicity galaxies and indicated that low-metallicity galaxies appear to show a steeper curve similar to that of the SMC curve, while the slope of the high-metallicity curve is identical to that of the Calzetti curve. This result can be explained by different dust grain properties or different dust-star geometries in different types of galaxy. It is possible that the SMC curve is not very suitable for HAEs with $9.2 < \log(M_*/M_\odot) < 10.2$, results in an underestimate of dust attenuation for the stellar continuum. This further influences the dust attenuation for emission lines and leads to a shallower slope in [Figure E.5](#).

Although the most suitable dust attenuation curve for the stellar continuum and nebular emission of the high-redshift galaxies is still remaining as an open question, we think that the dust attenuation recipe we presented in the main text is acceptable and would not lead to large systematic errors on the physical properties of our HAEs.

Deriving reddening from the observed flux ratio of hydrogen recombination lines (e.g., $H\alpha/H\beta$) is considered the gold standard for the dust correction for nebular emission. Here, we further compare the SED-derived $E(B - V)_{neb}$ and Balmer decrement derived $E(B - V)_{neb}$. [Reddy et al. \(2015\)](#) indicated that the difference between $E(B - V)_{neb}$ and $E(B - V)_{star}$ is correlated to $SFR(H\alpha)$, where the difference between the two components increases with increasing SFR. Since the SED-derived $E(B - V)_{neb}$ for our HAEs are directly related to $E(B - V)_{star}$, we investigate whether this correlation exists here.

We make use of the cross-matching HAEs to the MOSDEF Emission-Line Catalog in [section 3.5.2](#). Among them, 83 galaxies have detection of $H\beta$ and a further cut leads to 60 galaxies with $S/N > 3$. Then, we calculated $E(B - V)_{neb,balmer}$ by [Equation \(8\)](#), meanwhile $E(B - V)_{neb,SED}$ are already existing in our catalog. In addition, we calculate $SFR(H\alpha)$ from the MOSDEF data since spectroscopic measurements are more accurate. [Figure E.6](#) presents the relation of difference in color excesses and $SFR(H\alpha)$. It is clear that this relation is existing, and $E(B - V)_{neb,balmer}$ are substantially redder than $E(B - V)_{neb,SED}$ at larger $SFR(H\alpha)$. The best-fit linear relation to the individual galaxies is,

$$E(B - V)_{neb,balmer} - E(B - V)_{neb,SED} = (0.254 \pm 0.028) \times \log(SFR(H\alpha)) - (0.388 \pm 0.271). \quad (33)$$

In other words, this finding indicates that nebular color excesses are substantially redder than the continuum color excesses for galaxies with larger $SFR(H\alpha)$. Physically, this trend can be understood as the product of increased metal and dust enrichment of the ISM with increasing SFR, reflecting the simple model of [Reddy et al. \(2015\)](#) (see [Figure 20](#) in [Reddy et al. 2015](#)). This model indicated two distinct stellar populations in each galaxy: one is stars located in diffuse dust component, and another is stars resided in very dusty regions. As the SFR increases, these more obscured and dusty regions begin to dominate the nebular line and bolometric luminosities, while the diffuse component dominates the UV through optical SED at both low and high SFRs. Consequently, the color excesses of nebular and continuum diverge with rising SFR. This physical picture implies that galaxies with larger SFRs may exhibit a higher dispersion in their spatially resolved colors. Anyway, a further detailed analysis of the color dispersion and SFR surface density aided by

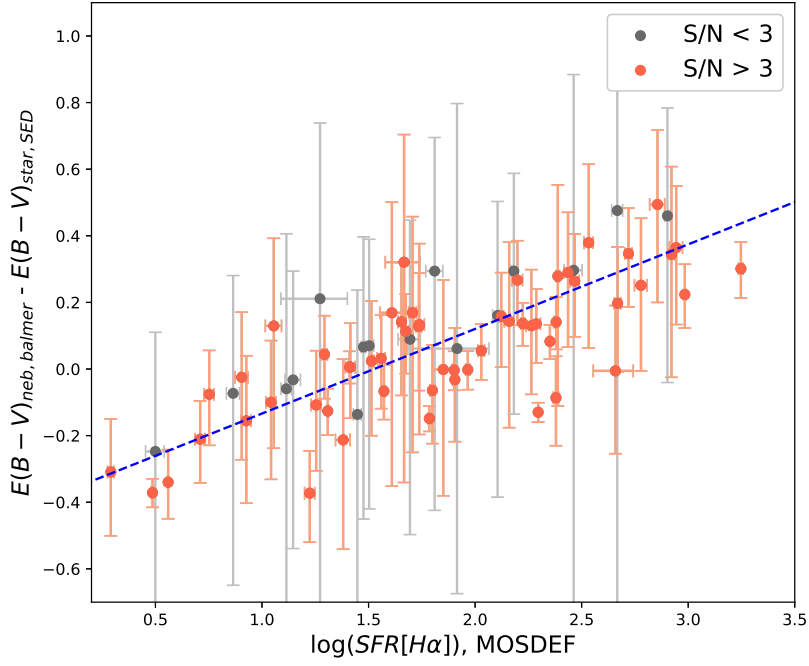


Figure E.6. The difference between the SED-derived color excess for nebular emission, $E(B - V)_{\text{neb, SED}}$, and the Balmer decrement derived color excess for nebular emission, $E(B - V)_{\text{neb, balmer}}$ as a function of $\text{SFR}(\text{H}\alpha)$. All these galaxies are cross-matched to the MOSDEF Emission-Line Catalog, and $\text{SFR}(\text{H}\alpha)$ are calculated from the spectroscopic measurements. The detection of $\text{H}\beta$ with $\text{S/N} > 3$ are presented as individual red circles, while others are grey circles. The blue dashed line shows the best-fit relation.

the deep and high resolution data, such as those from JWST, are needed to further explore the star formation activities in high-redshift SFGs.

References

- Abazajian, K. N., Adelman-McCarthy, J. K., Agüeros, M. A., et al. 2009, *ApJS*, 182, 543, doi: [10.1088/0067-0049/182/2/543](https://doi.org/10.1088/0067-0049/182/2/543)
- Andrews, B. H., & Martini, P. 2013, *ApJ*, 765, 140, doi: [10.1088/0004-637X/765/2/140](https://doi.org/10.1088/0004-637X/765/2/140)
- Berg, D. A., Skillman, E. D., Marble, A. R., et al. 2012, *ApJ*, 754, 98, doi: [10.1088/0004-637X/754/2/98](https://doi.org/10.1088/0004-637X/754/2/98)
- Bertin, E. 2010a, SCAMP: Automatic Astrometric and Photometric Calibration. <http://ascl.net/1010.063>
- . 2010b, SWarp: Resampling and Co-adding FITS Images Together. <http://ascl.net/1010.068>
- Bertin, E., & Arnouts, S. 1996, *A&AS*, 117, 393, doi: [10.1051/aas:1996164](https://doi.org/10.1051/aas:1996164)
- Bian, F., Kewley, L. J., & Dopita, M. A. 2018, *ApJ*, 859, 175, doi: [10.3847/1538-4357/aab74](https://doi.org/10.3847/1538-4357/aab74)
- Bianco, F. B., Modjaz, M., Oh, S. M., et al. 2016, *A&C*, 16, 54, doi: [10.1016/j.ascom.2016.03.002](https://doi.org/10.1016/j.ascom.2016.03.002)
- Boquien, M., Burgarella, D., Roehlly, Y., et al. 2019, *A&A*, 622, A103, doi: [10.1051/0004-6361/201834156](https://doi.org/10.1051/0004-6361/201834156)
- Boucaud, A., Bocchio, M., Abergel, A., et al. 2016, *A&A*, 596, A63, doi: [10.1051/0004-6361/201629080](https://doi.org/10.1051/0004-6361/201629080)
- Brammer, G. B., van Dokkum, P. G., & Coppi, P. 2008, *ApJ*, 686, 1503, doi: [10.1086/591786](https://doi.org/10.1086/591786)
- Brinchmann, J., Charlot, S., White, S. D. M., et al. 2004, *MNRAS*, 351, 1151, doi: [10.1111/j.1365-2966.2004.07881.x](https://doi.org/10.1111/j.1365-2966.2004.07881.x)
- Bruzual, G., & Charlot, S. 2003, *MNRAS*, 344, 1000, doi: [10.1046/j.1365-8711.2003.06897.x](https://doi.org/10.1046/j.1365-8711.2003.06897.x)
- Burgarella, D., Buat, V., & Iglesias-Páramo, J. 2005, *MNRAS*, 360, 1413, doi: [10.1111/j.1365-2966.2005.09131.x](https://doi.org/10.1111/j.1365-2966.2005.09131.x)
- Calzetti, D. 2013, *Star Formation Rate Indicators*, ed. J. Falcón-Barroso & J. H. Knapen, 419
- Calzetti, D., Armus, L., Bohlin, R. C., et al. 2000, *ApJ*, 533, 682, doi: [10.1086/308692](https://doi.org/10.1086/308692)
- Calzetti, D., Harris, J., Gallagher, John S., I., et al. 2004, *AJ*, 127, 1405, doi: [10.1086/382095](https://doi.org/10.1086/382095)
- Calzetti, D., Kinney, A. L., & Storchi-Bergmann, T. 1994, *ApJ*, 429, 582, doi: [10.1086/174346](https://doi.org/10.1086/174346)
- Cardamone, C., Schawinski, K., Sarzi, M., et al. 2009, *MNRAS*, 399, 1191, doi: [10.1111/j.1365-2966.2009.15383.x](https://doi.org/10.1111/j.1365-2966.2009.15383.x)
- Cardelli, J. A., Clayton, G. C., & Mathis, J. S. 1989, *ApJ*, 345, 245, doi: [10.1086/167900](https://doi.org/10.1086/167900)
- Chabrier, G. 2003, *PASP*, 115, 763, doi: [10.1086/376392](https://doi.org/10.1086/376392)
- Chambers, K. C., Magnier, E. A., Metcalfe, N., et al. 2016, arXiv e-prints, arXiv:1612.05560. <https://arxiv.org/abs/1612.05560>
- Charlot, S., & Fall, S. M. 2000, *ApJ*, 539, 718, doi: [10.1086/309250](https://doi.org/10.1086/309250)
- Charlot, S., & Longhetti, M. 2001, *MNRAS*, 323, 887, doi: [10.1046/j.1365-8711.2001.04260.x](https://doi.org/10.1046/j.1365-8711.2001.04260.x)

- Christensen, L., Laursen, P., Richard, J., et al. 2012, MNRAS, 427, 1973, doi: [10.1111/j.1365-2966.2012.22007.x](https://doi.org/10.1111/j.1365-2966.2012.22007.x)
- Cibinel, A., Daddi, E., Sargent, M. T., et al. 2019, MNRAS, 485, 5631, doi: [10.1093/mnras/stz690](https://doi.org/10.1093/mnras/stz690)
- Cohn, J. H., Leja, J., Tran, K.-V. H., et al. 2018, ApJ, 869, 141, doi: [10.3847/1538-4357/aaed3d](https://doi.org/10.3847/1538-4357/aaed3d)
- Conroy, C., & Gunn, J. E. 2010, ApJ, 712, 833, doi: [10.1088/0004-637X/712/2/833](https://doi.org/10.1088/0004-637X/712/2/833)
- Conroy, C., Gunn, J. E., & White, M. 2009, ApJ, 699, 486, doi: [10.1088/0004-637X/699/1/486](https://doi.org/10.1088/0004-637X/699/1/486)
- Cowley, M. J., Spitler, L. R., Tran, K.-V. H., et al. 2016, MNRAS, 457, 629, doi: [10.1093/mnras/stv2992](https://doi.org/10.1093/mnras/stv2992)
- Cucciati, O., Tresse, L., Ilbert, O., et al. 2012, A&A, 539, A31, doi: [10.1051/0004-6361/201118010](https://doi.org/10.1051/0004-6361/201118010)
- Curti, M., Cresci, G., Mannucci, F., et al. 2017, MNRAS, 465, 1384, doi: [10.1093/mnras/stw2766](https://doi.org/10.1093/mnras/stw2766)
- Curti, M., Mannucci, F., Cresci, G., & Maiolino, R. 2020, MNRAS, 491, 944, doi: [10.1093/mnras/stz2910](https://doi.org/10.1093/mnras/stz2910)
- Dale, D. A., Helou, G., Magdis, G. E., et al. 2014, ApJ, 784, 83, doi: [10.1088/0004-637X/784/1/83](https://doi.org/10.1088/0004-637X/784/1/83)
- Davé, R., Raffaeferantsoa, M. H., Thompson, R. J., & Hopkins, P. F. 2017, MNRAS, 467, 115, doi: [10.1093/mnras/stx108](https://doi.org/10.1093/mnras/stx108)
- Davé, R., Thompson, R., & Hopkins, P. F. 2016, MNRAS, 462, 3265, doi: [10.1093/mnras/stw1862](https://doi.org/10.1093/mnras/stw1862)
- De Lucia, G., Kauffmann, G., & White, S. D. M. 2004, MNRAS, 349, 1101, doi: [10.1111/j.1365-2966.2004.07584.x](https://doi.org/10.1111/j.1365-2966.2004.07584.x)
- Dopita, M. A., & Evans, I. N. 1986, ApJ, 307, 431, doi: [10.1086/164432](https://doi.org/10.1086/164432)
- Eikenberry, S., Bandyopadhyay, R., Bennett, J. G., et al. 2012, in SPIE, Vol. 8446, , 84460I, doi: [10.1117/12.925679](https://doi.org/10.1117/12.925679)
- Elbaz, D., Daddi, E., Le Borgne, D., et al. 2007, A&A, 468, 33, doi: [10.1051/0004-6361:20077525](https://doi.org/10.1051/0004-6361:20077525)
- Erb, D. K., Pettini, M., Shapley, A. E., et al. 2010, ApJ, 719, 1168, doi: [10.1088/0004-637X/719/2/1168](https://doi.org/10.1088/0004-637X/719/2/1168)
- Erb, D. K., Shapley, A. E., Pettini, M., et al. 2006, ApJ, 644, 813, doi: [10.1086/503623](https://doi.org/10.1086/503623)
- Fabian, A. C. 2012, ARA&A, 50, 455, doi: [10.1146/annurev-astro-081811-125521](https://doi.org/10.1146/annurev-astro-081811-125521)
- Faisst, A. L., Masters, D., Wang, Y., et al. 2018, ApJ, 855, 132, doi: [10.3847/1538-4357/aab1fc](https://doi.org/10.3847/1538-4357/aab1fc)
- Ferland, G. J., Korista, K. T., Verner, D. A., et al. 1998, PASP, 110, 761, doi: [10.1086/316190](https://doi.org/10.1086/316190)
- Ferland, G. J., Porter, R. L., van Hoof, P. A. M., et al. 2013, RMxAA, 49, 137. <https://arxiv.org/abs/1302.4485>
- Ferrière, K. M. 2001, Reviews of Modern Physics, 73, 1031, doi: [10.1103/RevModPhys.73.1031](https://doi.org/10.1103/RevModPhys.73.1031)
- Flores Velázquez, J. A., Gurvich, A. B., Faucher-Giguère, C.-A., et al. 2021, MNRAS, 501, 4812, doi: [10.1093/mnras/staa3893](https://doi.org/10.1093/mnras/staa3893)
- Förster Schreiber, N. M., Genzel, R., Lutz, D., Kunze, D., & Sternberg, A. 2001, ApJ, 552, 544, doi: [10.1086/320546](https://doi.org/10.1086/320546)

- Fosbury, R. A. E., Villar-Martín, M., Humphrey, A., et al. 2003, *ApJ*, 596, 797, doi: [10.1086/378228](https://doi.org/10.1086/378228)
- Gaia Collaboration, Brown, A. G. A., Vallenari, A., et al. 2018, *A&A*, 616, A1, doi: [10.1051/0004-6361/201833051](https://doi.org/10.1051/0004-6361/201833051)
- Geach, J. E., Smail, I., Best, P. N., et al. 2008, *MNRAS*, 388, 1473, doi: [10.1111/j.1365-2966.2008.13481.x](https://doi.org/10.1111/j.1365-2966.2008.13481.x)
- Giacconi, R., Zirm, A., Wang, J., et al. 2002, *ApJS*, 139, 369, doi: [10.1086/338927](https://doi.org/10.1086/338927)
- Gordon, K. D., Clayton, G. C., Misselt, K. A., Landolt, A. U., & Wolff, M. J. 2003, *ApJ*, 594, 279, doi: [10.1086/376774](https://doi.org/10.1086/376774)
- Grazian, A., Giallongo, E., Gerbasi, R., et al. 2016, *A&A*, 585, A48, doi: [10.1051/0004-6361/201526396](https://doi.org/10.1051/0004-6361/201526396)
- Gruen, D., Seitz, S., & Bernstein, G. M. 2014, *PASP*, 126, 158, doi: [10.1086/675080](https://doi.org/10.1086/675080)
- Gruppioni, C., Pozzi, F., Rodighiero, G., et al. 2013, *MNRAS*, 432, 23, doi: [10.1093/mnras/stt308](https://doi.org/10.1093/mnras/stt308)
- Gutkin, J., Charlot, S., & Bruzual, G. 2016, *MNRAS*, 462, 1757, doi: [10.1093/mnras/stw1716](https://doi.org/10.1093/mnras/stw1716)
- Hagen, A., Zeimann, G. R., Behrens, C., et al. 2016, *ApJ*, 817, 79, doi: [10.3847/0004-637X/817/1/79](https://doi.org/10.3847/0004-637X/817/1/79)
- Hayashi, M., Kodama, T., Tanaka, I., et al. 2016, *ApJL*, 826, L28, doi: [10.3847/2041-8205/826/2/L28](https://doi.org/10.3847/2041-8205/826/2/L28)
- Hayes, M., Schaerer, D., & Östlin, G. 2010, *A&A*, 509, L5, doi: [10.1051/0004-6361/200913217](https://doi.org/10.1051/0004-6361/200913217)
- Inoue, A. K. 2011, *MNRAS*, 415, 2920, doi: [10.1111/j.1365-2966.2011.18906.x](https://doi.org/10.1111/j.1365-2966.2011.18906.x)
- Izotov, Y. I., Stasińska, G., Meynet, G., Guseva, N. G., & Thuan, T. X. 2006, *A&A*, 448, 955, doi: [10.1051/0004-6361:20053763](https://doi.org/10.1051/0004-6361:20053763)
- Janowiecki, S., Salzer, J. J., van Zee, L., Rosenberg, J. L., & Skillman, E. 2017, *ApJ*, 836, 128, doi: [10.3847/1538-4357/836/1/128](https://doi.org/10.3847/1538-4357/836/1/128)
- Johnson, B. D., Leja, J., Conroy, C., & Speagle, J. S. 2021, *ApJS*, 254, 22, doi: [10.3847/1538-4365/abef67](https://doi.org/10.3847/1538-4365/abef67)
- Jones, T., Martin, C., & Cooper, M. C. 2015, *ApJ*, 813, 126, doi: [10.1088/0004-637X/813/2/126](https://doi.org/10.1088/0004-637X/813/2/126)
- Kaasinen, M., Bian, F., Groves, B., Kewley, L. J., & Gupta, A. 2017, *MNRAS*, 465, 3220, doi: [10.1093/mnras/stw2827](https://doi.org/10.1093/mnras/stw2827)
- Kaasinen, M., Kewley, L., Bian, F., et al. 2018, *MNRAS*, 477, 5568, doi: [10.1093/mnras/sty1012](https://doi.org/10.1093/mnras/sty1012)
- Kashino, D., Silverman, J. D., Rodighiero, G., et al. 2013, *ApJL*, 777, L8, doi: [10.1088/2041-8205/777/1/L8](https://doi.org/10.1088/2041-8205/777/1/L8)
- Kauffmann, G., Heckman, T. M., Tremonti, C., et al. 2003, *MNRAS*, 346, 1055, doi: [10.1111/j.1365-2966.2003.07154.x](https://doi.org/10.1111/j.1365-2966.2003.07154.x)
- Kennicutt, Robert C., J. 1998, *ARA&A*, 36, 189, doi: [10.1146/annurev.astro.36.1.189](https://doi.org/10.1146/annurev.astro.36.1.189)
- Kennicutt, R. C., & Evans, N. J. 2012, *ARA&A*, 50, 531, doi: [10.1146/annurev-astro-081811-125610](https://doi.org/10.1146/annurev-astro-081811-125610)

- Kewley, L. J., & Dopita, M. A. 2002, *ApJS*, 142, 35, doi: [10.1086/341326](https://doi.org/10.1086/341326)
- Kewley, L. J., Dopita, M. A., Leitherer, C., et al. 2013a, *ApJ*, 774, 100, doi: [10.1088/0004-637X/774/2/100](https://doi.org/10.1088/0004-637X/774/2/100)
- Kewley, L. J., & Ellison, S. L. 2008, *ApJ*, 681, 1183, doi: [10.1086/587500](https://doi.org/10.1086/587500)
- Kewley, L. J., Maier, C., Yabe, K., et al. 2013b, *ApJL*, 774, L10, doi: [10.1088/2041-8205/774/1/L10](https://doi.org/10.1088/2041-8205/774/1/L10)
- Kewley, L. J., Nicholls, D. C., & Sutherland, R. S. 2019, *ARA&A*, 57, 511, doi: [10.1146/annurev-astro-081817-051832](https://doi.org/10.1146/annurev-astro-081817-051832)
- Kewley, L. J., Zahid, H. J., Geller, M. J., et al. 2015, *ApJL*, 812, L20, doi: [10.1088/2041-8205/812/2/L20](https://doi.org/10.1088/2041-8205/812/2/L20)
- Kobulnicky, H. A., & Kewley, L. J. 2004, *ApJ*, 617, 240, doi: [10.1086/425299](https://doi.org/10.1086/425299)
- Konishi, M., Motohara, K., Takahashi, H., et al. 2012, in *SPIE*, Vol. 8446, , 84467P, doi: [10.1117/12.924259](https://doi.org/10.1117/12.924259)
- Kormendy, J., & Ho, L. C. 2013, *ARA&A*, 51, 511, doi: [10.1146/annurev-astro-082708-101811](https://doi.org/10.1146/annurev-astro-082708-101811)
- Koyama, Y., Smail, I., Kurk, J., et al. 2013, *MNRAS*, 434, 423, doi: [10.1093/mnras/stt1035](https://doi.org/10.1093/mnras/stt1035)
- Kriek, M., van Dokkum, P. G., Labbé, I., et al. 2009, *ApJ*, 700, 221, doi: [10.1088/0004-637X/700/1/221](https://doi.org/10.1088/0004-637X/700/1/221)
- Kriek, M., Shapley, A. E., Reddy, N. A., et al. 2015, *ApJS*, 218, 15, doi: [10.1088/0067-0049/218/2/15](https://doi.org/10.1088/0067-0049/218/2/15)
- Krumholz, M. R., McKee, C. F., & Tumlinson, J. 2009, *ApJ*, 693, 216, doi: [10.1088/0004-637X/693/1/216](https://doi.org/10.1088/0004-637X/693/1/216)
- Kubo, M., Umehata, H., Matsuda, Y., et al. 2021, *ApJ*, 919, 6, doi: [10.3847/1538-4357/ac0cf8](https://doi.org/10.3847/1538-4357/ac0cf8)
- Laigle, C., McCracken, H. J., Ilbert, O., et al. 2016, *ApJS*, 224, 24, doi: [10.3847/0067-0049/224/2/24](https://doi.org/10.3847/0067-0049/224/2/24)
- Lawrence, A., Warren, S. J., Almaini, O., et al. 2007, *MNRAS*, 379, 1599, doi: [10.1111/j.1365-2966.2007.12040.x](https://doi.org/10.1111/j.1365-2966.2007.12040.x)
- Lequeux, J., Peimbert, M., Rayo, J. F., Serrano, A., & Torres-Peimbert, S. 1979, *A&A*, 500, 145
- Madau, P., & Dickinson, M. 2014, *ARA&A*, 52, 415, doi: [10.1146/annurev-astro-081811-125615](https://doi.org/10.1146/annurev-astro-081811-125615)
- Maiolino, R., Nagao, T., Grazian, A., et al. 2008, *A&A*, 488, 463, doi: [10.1051/0004-6361:200809678](https://doi.org/10.1051/0004-6361:200809678)
- Mannucci, F., Cresci, G., Maiolino, R., Marconi, A., & Gnerucci, A. 2010, *MNRAS*, 408, 2115, doi: [10.1111/j.1365-2966.2010.17291.x](https://doi.org/10.1111/j.1365-2966.2010.17291.x)
- Mannucci, F., Cresci, G., Maiolino, R., et al. 2009, *MNRAS*, 398, 1915, doi: [10.1111/j.1365-2966.2009.15185.x](https://doi.org/10.1111/j.1365-2966.2009.15185.x)
- Maraston, C. 2005, *MNRAS*, 362, 799, doi: [10.1111/j.1365-2966.2005.09270.x](https://doi.org/10.1111/j.1365-2966.2005.09270.x)
- Matthee, J., Sobral, D., Best, P., et al. 2017, *MNRAS*, 465, 3637, doi: [10.1093/mnras/stw2973](https://doi.org/10.1093/mnras/stw2973)

- McCracken, H. J., Milvang-Jensen, B., Dunlop, J., et al. 2012, *A&A*, 544, A156, doi: [10.1051/0004-6361/201219507](https://doi.org/10.1051/0004-6361/201219507)
- McLean, I. S., Steidel, C. C., Epps, H. W., et al. 2012, in *SPIE*, Vol. 8446, , 84460J, doi: [10.1117/12.924794](https://doi.org/10.1117/12.924794)
- Moffat, A. F. J. 1969, *A&A*, 3, 455
- Momcheva, I. G., Brammer, G. B., van Dokkum, P. G., et al. 2016, *ApJS*, 225, 27, doi: [10.3847/0067-0049/225/2/27](https://doi.org/10.3847/0067-0049/225/2/27)
- Motohara, K., Konishi, M., Takahashi, H., et al. 2014, in *SPIE*, Vol. 9147, , 91476K, doi: [10.1117/12.2054861](https://doi.org/10.1117/12.2054861)
- Nakajima, K., & Ouchi, M. 2014, *MNRAS*, 442, 900, doi: [10.1093/mnras/stu902](https://doi.org/10.1093/mnras/stu902)
- Nakajima, K., Ouchi, M., Shimasaku, K., et al. 2013, *ApJ*, 769, 3, doi: [10.1088/0004-637X/769/1/3](https://doi.org/10.1088/0004-637X/769/1/3)
- Nanayakkara, T., Glazebrook, K., Kacprzak, G. G., et al. 2016, *ApJ*, 828, 21, doi: [10.3847/0004-637X/828/1/21](https://doi.org/10.3847/0004-637X/828/1/21)
- Noll, S., Burgarella, D., Giovannoli, E., et al. 2009, *A&A*, 507, 1793, doi: [10.1051/0004-6361/200912497](https://doi.org/10.1051/0004-6361/200912497)
- Oke, J. B., & Gunn, J. E. 1983, *ApJ*, 266, 713, doi: [10.1086/160817](https://doi.org/10.1086/160817)
- Onodera, M., Carollo, C. M., Lilly, S., et al. 2016, *ApJ*, 822, 42, doi: [10.3847/0004-637X/822/1/42](https://doi.org/10.3847/0004-637X/822/1/42)
- Onodera, M., Shimakawa, R., Suzuki, T. L., et al. 2020, *ApJ*, 904, 180, doi: [10.3847/1538-4357/abc174](https://doi.org/10.3847/1538-4357/abc174)
- Osterbrock, D. E. 1989, *Astrophysics of gaseous nebulae and active galactic nuclei*
- Ouchi, M., Mobasher, B., Shimasaku, K., et al. 2009, *ApJ*, 706, 1136, doi: [10.1088/0004-637X/706/2/1136](https://doi.org/10.1088/0004-637X/706/2/1136)
- Pagel, B. E. J., Simonson, E. A., Terlevich, R. J., & Edmunds, M. G. 1992, *MNRAS*, 255, 325, doi: [10.1093/mnras/255.2.325](https://doi.org/10.1093/mnras/255.2.325)
- Papovich, C., Momcheva, I., Willmer, C. N. A., et al. 2010, *ApJ*, 716, 1503, doi: [10.1088/0004-637X/716/2/1503](https://doi.org/10.1088/0004-637X/716/2/1503)
- Peeples, M. S., Pogge, R. W., & Stanek, K. Z. 2009, *ApJ*, 695, 259, doi: [10.1088/0004-637X/695/1/259](https://doi.org/10.1088/0004-637X/695/1/259)
- Peng, Y., Maiolino, R., & Cochrane, R. 2015, *Nature*, 521, 192, doi: [10.1038/nature14439](https://doi.org/10.1038/nature14439)
- Persson, S. E., Murphy, D. C., Smee, S., et al. 2013, *PASP*, 125, 654, doi: [10.1086/671164](https://doi.org/10.1086/671164)
- Pozzetti, L., Bolzonella, M., Lamareille, F., et al. 2007, *A&A*, 474, 443, doi: [10.1051/0004-6361:20077609](https://doi.org/10.1051/0004-6361:20077609)
- Price, S. H., Kriek, M., Brammer, G. B., et al. 2014, *ApJ*, 788, 86, doi: [10.1088/0004-637X/788/1/86](https://doi.org/10.1088/0004-637X/788/1/86)
- Reddy, N. A., Erb, D. K., Pettini, M., Steidel, C. C., & Shapley, A. E. 2010, *ApJ*, 712, 1070, doi: [10.1088/0004-637X/712/2/1070](https://doi.org/10.1088/0004-637X/712/2/1070)

- Reddy, N. A., Kriek, M., Shapley, A. E., et al. 2015, ApJ, 806, 259, doi: [10.1088/0004-637X/806/2/259](https://doi.org/10.1088/0004-637X/806/2/259)
- Reddy, N. A., Shapley, A. E., Sanders, R. L., et al. 2018, ApJ, 869, 92, doi: [10.3847/1538-4357/aaed1e](https://doi.org/10.3847/1538-4357/aaed1e)
- Reddy, N. A., Shapley, A. E., Kriek, M., et al. 2020, ApJ, 902, 123, doi: [10.3847/1538-4357/abb674](https://doi.org/10.3847/1538-4357/abb674)
- Saito, S., de la Torre, S., Ilbert, O., et al. 2020, MNRAS, 494, 199, doi: [10.1093/mnras/staa727](https://doi.org/10.1093/mnras/staa727)
- Salpeter, E. E. 1955, ApJ, 121, 161, doi: [10.1086/145971](https://doi.org/10.1086/145971)
- Sanders, R. L., Shapley, A. E., Zhang, K., & Yan, R. 2017, ApJ, 850, 136, doi: [10.3847/1538-4357/aa93e4](https://doi.org/10.3847/1538-4357/aa93e4)
- Sanders, R. L., Shapley, A. E., Kriek, M., et al. 2018, ApJ, 858, 99, doi: [10.3847/1538-4357/aabcd](https://doi.org/10.3847/1538-4357/aabcd)
- Sanders, R. L., Shapley, A. E., Jones, T., et al. 2021, ApJ, 914, 19, doi: [10.3847/1538-4357/abf4c1](https://doi.org/10.3847/1538-4357/abf4c1)
- Schechter, P. 1976, ApJ, 203, 297, doi: [10.1086/154079](https://doi.org/10.1086/154079)
- Scoville, N., Abraham, R. G., Aussel, H., et al. 2007, ApJS, 172, 38, doi: [10.1086/516580](https://doi.org/10.1086/516580)
- Shimakawa, R., Kodama, T., Shibuya, T., et al. 2017, MNRAS, 468, 1123, doi: [10.1093/mnras/stx091](https://doi.org/10.1093/mnras/stx091)
- Shimakawa, R., Kodama, T., Hayashi, M., et al. 2018a, MNRAS, 473, 1977, doi: [10.1093/mnras/stx2494](https://doi.org/10.1093/mnras/stx2494)
- Shimakawa, R., Koyama, Y., Röttgering, H. J. A., et al. 2018b, MNRAS, 481, 5630, doi: [10.1093/mnras/sty2618](https://doi.org/10.1093/mnras/sty2618)
- Shivaei, I., Reddy, N. A., Shapley, A. E., et al. 2015, ApJ, 815, 98, doi: [10.1088/0004-637X/815/2/98](https://doi.org/10.1088/0004-637X/815/2/98)
- Shivaei, I., Reddy, N., Rieke, G., et al. 2020, ApJ, 899, 117, doi: [10.3847/1538-4357/aba35e](https://doi.org/10.3847/1538-4357/aba35e)
- Skelton, R. E., Whitaker, K. E., Momcheva, I. G., et al. 2014, ApJS, 214, 24, doi: [10.1088/0067-0049/214/2/24](https://doi.org/10.1088/0067-0049/214/2/24)
- Skrutskie, M. F., Cutri, R. M., Stiening, R., et al. 2006, AJ, 131, 1163, doi: [10.1086/498708](https://doi.org/10.1086/498708)
- Smith, L. J., Westmoquette, M. S., Gallagher, J. S., et al. 2006, MNRAS, 370, 513, doi: [10.1111/j.1365-2966.2006.10507.x](https://doi.org/10.1111/j.1365-2966.2006.10507.x)
- Sobral, D., Smail, I., Best, P. N., et al. 2013, MNRAS, 428, 1128, doi: [10.1093/mnras/sts096](https://doi.org/10.1093/mnras/sts096)
- Sobral, D., Best, P. N., Geach, J. E., et al. 2009, MNRAS, 398, 75, doi: [10.1111/j.1365-2966.2009.15129.x](https://doi.org/10.1111/j.1365-2966.2009.15129.x)
- Somerville, R. S., & Davé, R. 2015, ARA&A, 53, 51, doi: [10.1146/annurev-astro-082812-140951](https://doi.org/10.1146/annurev-astro-082812-140951)
- Sparke, L. S., & Gallagher, John S., I. 2007, Galaxies in the Universe: An Introduction
- Sparre, M., Hayward, C. C., Feldmann, R., et al. 2017, MNRAS, 466, 88, doi: [10.1093/mnras/stw3011](https://doi.org/10.1093/mnras/stw3011)

- Speagle, J. S., Steinhardt, C. L., Capak, P. L., & Silverman, J. D. 2014, *ApJS*, 214, 15, doi: [10.1088/0067-0049/214/2/15](https://doi.org/10.1088/0067-0049/214/2/15)
- Spitler, L. R., Labbé, I., Glazebrook, K., et al. 2012, *ApJL*, 748, L21, doi: [10.1088/2041-8205/748/2/L21](https://doi.org/10.1088/2041-8205/748/2/L21)
- Stecher, T. P. 1965, *ApJ*, 142, 1683, doi: [10.1086/148462](https://doi.org/10.1086/148462)
- Steidel, C. C., Rudie, G. C., Strom, A. L., et al. 2014, *ApJ*, 795, 165, doi: [10.1088/0004-637X/795/2/165](https://doi.org/10.1088/0004-637X/795/2/165)
- Straatman, C. M. S., Spitler, L. R., Quadri, R. F., et al. 2016, *ApJ*, 830, 51, doi: [10.3847/0004-637X/830/1/51](https://doi.org/10.3847/0004-637X/830/1/51)
- Suzuki, R., Tokoku, C., Ichikawa, T., et al. 2008, *PASJ*, 60, 1347, doi: [10.1093/pasj/60.6.1347](https://doi.org/10.1093/pasj/60.6.1347)
- Suzuki, T. L., Kodama, T., Onodera, M., et al. 2017, *ApJ*, 849, 39, doi: [10.3847/1538-4357/aa8df3](https://doi.org/10.3847/1538-4357/aa8df3)
- Terao, Y. 2020, PhD Thesis, Univ. of Tokyo
- Theios, R. L., Steidel, C. C., Strom, A. L., et al. 2019, *ApJ*, 871, 128, doi: [10.3847/1538-4357/aaf386](https://doi.org/10.3847/1538-4357/aaf386)
- Thompson, R., Nagamine, K., Jaacks, J., & Choi, J.-H. 2014, *ApJ*, 780, 145, doi: [10.1088/0004-637X/780/2/145](https://doi.org/10.1088/0004-637X/780/2/145)
- Topping, M. W., Shapley, A. E., Sanders, R. L., et al. 2021, *MNRAS*, 506, 1237, doi: [10.1093/mnras/stab1793](https://doi.org/10.1093/mnras/stab1793)
- Tran, K.-V. H., Alcorn, L. Y., Kacprzak, G. G., et al. 2017, *ApJ*, 834, 101, doi: [10.3847/1538-4357/834/2/101](https://doi.org/10.3847/1538-4357/834/2/101)
- Tremonti, C. A., Heckman, T. M., Kauffmann, G., et al. 2004, *ApJ*, 613, 898, doi: [10.1086/423264](https://doi.org/10.1086/423264)
- Vanzella, E., Giavalisco, M., Inoue, A. K., et al. 2010, *ApJ*, 725, 1011, doi: [10.1088/0004-637X/725/1/1011](https://doi.org/10.1088/0004-637X/725/1/1011)
- Weaver, J. R., Kauffmann, O. B., Ilbert, O., et al. 2021, arXiv e-prints, arXiv:2110.13923. <https://arxiv.org/abs/2110.13923>
- Whitaker, K. E., Franx, M., Leja, J., et al. 2014, *ApJ*, 795, 104, doi: [10.1088/0004-637X/795/2/104](https://doi.org/10.1088/0004-637X/795/2/104)
- Yeh, S. C. C., & Matzner, C. D. 2012, *ApJ*, 757, 108, doi: [10.1088/0004-637X/757/2/108](https://doi.org/10.1088/0004-637X/757/2/108)
- York, D. G., Adelman, J., Anderson, John E., J., et al. 2000, *AJ*, 120, 1579, doi: [10.1086/301513](https://doi.org/10.1086/301513)
- Yoshii, Y., Aoki, T., Doi, M., et al. 2010, in *SPIE*, Vol. 7733, , 773308, doi: [10.1117/12.856680](https://doi.org/10.1117/12.856680)
- Zeimann, G. R., Stanford, S. A., Brodwin, M., et al. 2013, *ApJ*, 779, 137, doi: [10.1088/0004-637X/779/2/137](https://doi.org/10.1088/0004-637X/779/2/137)